

GROWTH AND CHARACTERISATION OF PICRATE FAMILY CRYSTALS

**MAJOR RESEARCH PROJECT 3rd YEAR REPORT SUBMITTED TO
THE UNIVERSITY GRANTS COMMISSION: 2012-15
UGC F. No [41-270/2012(SR)]**

By

**DR. SP. MEENAKSHISUNDARAM
PRINCIPAL INVESTIGATOR**

DEPARTMENT OF CHEMISTRY



**ANNAMALAINAGAR - 608 002
TAMILNADU, INDIA**

INDEX

S.NO	TITLE	PAGE NO.
1	OBJECTIVE OF THE PROJECT	1
2	METHODOLOGY	1
3	WORK DONE AND RESULTS ACHIEVED	2
3.1	Synthesis, crystal growth, characterization and theoretical studies of 4-benzoylanilinium picrate and 2-benzoyl-4-nitroanilinium picrate crystals	2-22
3.2	Synthesis, growth, structure, hyperpolarizability and supramolecular architecture of some organic picrate crystals 1. (2-aminobenzyl)methylammonium- picrate 2. 1-benzylpiperidyl-4-ammonium picrate 3. (diaminomethyl)sulfonium picrate 4. 4-formyl-N,N-dimethylbenzenammonium picrate	23-38
3.3	Supramolecular architecture of third-order nonlinear optical ammonium picrate crystals: DFT	39-63
3.4	Crystal growth, characterization and theoretical studies of 4-aminopyridinium picrate	64-81
3.5	Synthesis, structure, crystal growth and computational studies of tetrakis(thiourea)copper(I) picrate	82-96
3.6	Hyperpolarizability, Hirshfeld and Density functional theory computations of a nonlinear optical picrate	97-121
	LIST OF PUBLICATIONS	122

Objective of the project, Methodology and Work done

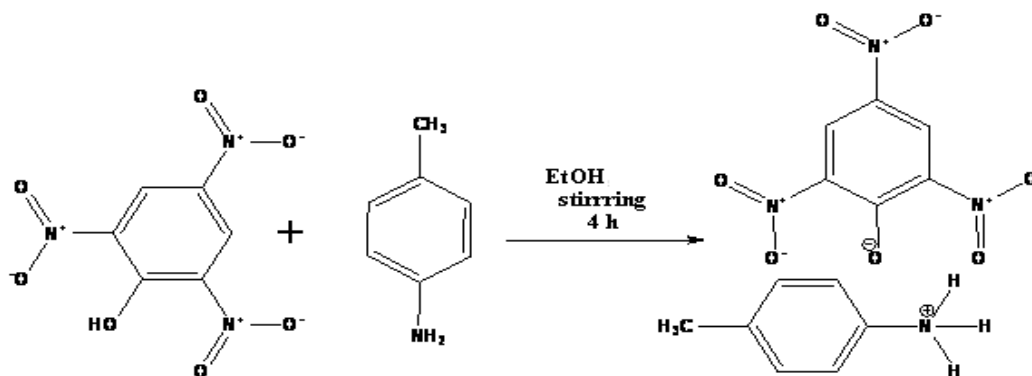
Mr. A. Aditya Prasad was selected as **project fellow** and he joined duty on 01.08.2012. The work as per plan is in progress.

Objective

- To synthesize and grow picrate crystals
- To characterize the picrate crystals
- To understand second-order NLO properties of as-grown crystals
- To calculate β (first order molecular hyperpolarizability)

Methodology

Picrate complexes are synthesized by stoichiometric incorporation of electron donor (amines, amino acids, piperidones etc.) and picric acid (electron acceptor) in the molar ratio of 1:1 in appropriate solvents.



Single crystals of picrates are grown from their alcoholic solution using slow evaporation solution growth technique. High quality transparent crystals are harvested from growth medium after attaining a reasonable size. For selected crystals the structural analysis is done using single crystal XRD analysis. Various characterisation studies are performed such as FT-IR, UV-VIS, TG-DTA, SEM and powder X-ray diffraction to analyse the crystal. Theoretical studies are also carried out and mostly the theoretical data are in agreement with experimental results.

WORK DONE AND RESULTS ACHIEVED

CHAPTER-3.1

Synthesis, crystal growth, characterization and theoretical studies of 4-benzoylanilinium picrate and 2-benzoyl-4-nitroanilinium picrate crystals

Single crystals of 4-benzoylanilinium picrate (BAP) were grown by slow evaporation solution growth technique from a solution of a mixed solvent system methanol-acetone (1:1,v/v) containing equimolar quantities of 4-aminobenzophenone and picric acid. The functional groups present in the molecule are identified by FT-IR analysis. Scanning electron microscopy reveals the surface morphology of the grown crystals. Optimized geometry, first-order molecular hyperpolarizability (β), polarizability (α), bond lengths, bond angles and excited state energy from theoretical UV were derived by theoretical calculations. The complete assignment of the vibrational modes for 4-benzoylanilinium picrate was performed by the Scaled Quantum Mechanics Force Field (SQMFF) methodology using potential energy distribution. Natural Bond Orbital calculations were employed to study the stabilities arising from charge delocalization and intermolecular interactions. The atomic charge distributions of the atoms present in BAP are obtained by Mulliken charge population analysis.

Single crystals of 2-benzoyl-4-nitroanilinium picrate (BNAP) were grown by slow evaporation solution growth technique from a solution of ethanol-chloroform-acetic acid (1:1:1, v/v). The ^1H and ^{13}C signals of the specimen are analysed for identification. Fourier transformed infrared spectroscopy confirms the presence of characteristic functional groups.

Powder X-ray diffraction was carried out to determine the structure and crystallinity. The optical properties of the grown crystals were analyzed by UV-vis spectroscopy. Thermogravimetric (TG) and differential thermal analysis (DTA) studies reveal no decomposition up to the melting point. The surface morphology of the as-grown crystals was studied by scanning electron microscopy (SEM).

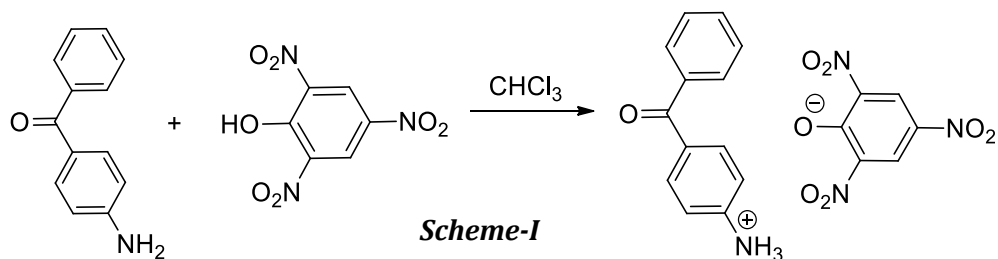
Introduction

Picric acid, as an electron acceptor, form charge transfer molecular complexes with a number of electron donor compounds through electrostatic or hydrogen bonding interactions. Hence, the picrates are convenient for identification and quantitative analysis of organic compounds. The bonding of these picrate complexes depends on the nature of the donor-acceptor system. Picrates are used in the synthesis of amine derivatives in qualitative organic chemistry. Recently, we have investigated the growth, structure and characterization of tetrakis(thiourea)zinc(II) picrate [1], *p*-toluidinium picrate [2] and (chloro)tris(thiourea- κ S)cadmium(II) picrate [3]. As a part of our investigations in the study of charge transfer complexes, the present work was undertaken.

Synthesis and growth

BAP was synthesized by mixing stoichiometric amounts of 4-aminobenzophenone (Sigma-Aldrich) and picric acid (Sigma-Aldrich) in an equimolar ratio using chloroform as solvent (Scheme-I). The mixture was stirred at room temperature ($\sim 30^\circ\text{C}$) for 3 h and the picrate was formed as reddish-yellow colour precipitate. The precipitate was collected from the

filter, dried and purified by recrystallization.



Recrystallized BAP was dissolved in mixed solvent system (methanol:acetone, 1:1, v/v) and the solution warmed with constant stirring for an hour to avoid co-precipitation of multiple phases. Reddish-yellow rod-like crystals were grown by slow evaporation solution growth technique and the crystals were harvested after a period of 8-10 d. Photographs of as-grown BAP are shown in **Fig.3.1.1a**.

BNAP was synthesized using 2-amino-5-nitrobenzophenone (Aldrich) and picric acid (Qualigens) in the molar ratio of 1:1 (Scheme-II). The reactants were dissolved in a mixed solvent system thoroughly mixed using a magnetic stirrer (5 h). Single crystals of BNAP were grown from the mixed solvent ethanol-chloroform-acetic acid (1:1:1, v/v) by slow evaporation solution growth technique. Crystallization took place within a period of 10–12 d and the photographs of as-grown crystals are shown in **Fig.3.1.1b**.

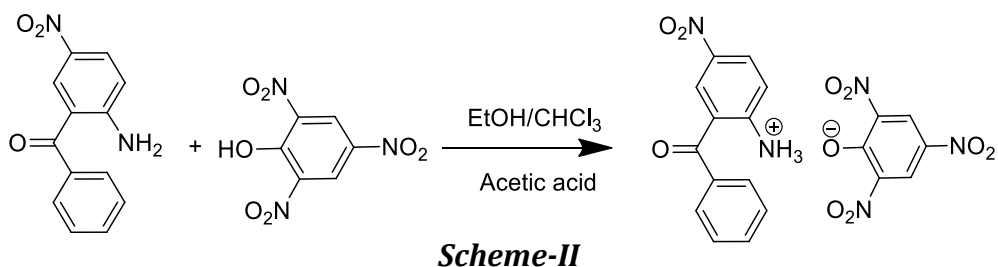




Fig.3.1.1 Photographs of as-grown crystals (a) 4-benzoylanilinium picrate
(b) 2-benzoyl-4-nitroanilinium picrate

FT-IR

To identify the presence of functional groups, Fourier transform infrared spectrum (FT-IR) was recorded using AVATAR 330 FT-IR spectrometer by KBr pellet technique in the spectral range of 400-4000 cm^{-1} . The vibrations are assigned with potential energy distribution by using VEDA program [4]. Most of the observed vibrational patterns coincide with theoretically predicted vibrational modes. The molecular structure of BAP consists of 43 atoms showing total 123 normal modes of vibrations and 31 vibrational modes are assigned by using PED. The molecular conformation yielded by geometry optimization exhibits no special symmetries and the molecule belongs to the C1 point group. Frequencies were scaled by using scaled quantum mechanics [5], with a scaling factor 0.98. The deviation from the experiment is less than 10 cm^{-1} with few exceptions. The N-H stretch lies in the spectral region experimentally around 3066 cm^{-1} but theoretically calculated frequency is $\sim 3099 \text{ cm}^{-1}$, showing high intense peak and $\sim 3751 \text{ cm}^{-1}$, $\sim 3678 \text{ cm}^{-1}$ also show N-H stretching. The H-N-H bending of the ammonium group is observed at $\sim 1866 \text{ cm}^{-1}$ and the

cm^{-1} are due to the symmetric and asymmetric stretching vibrations of NO_2 group. The peak at $\sim 3079 \text{ cm}^{-1}$ indicates the asymmetric stretching of NH_3^+ . The charge transfer complex is evidenced by the presence of main characteristic IR bands of donor and acceptor in the spectrum of the product. The observed vibrational bands of BNAP are listed in **Table 3.1.2**.

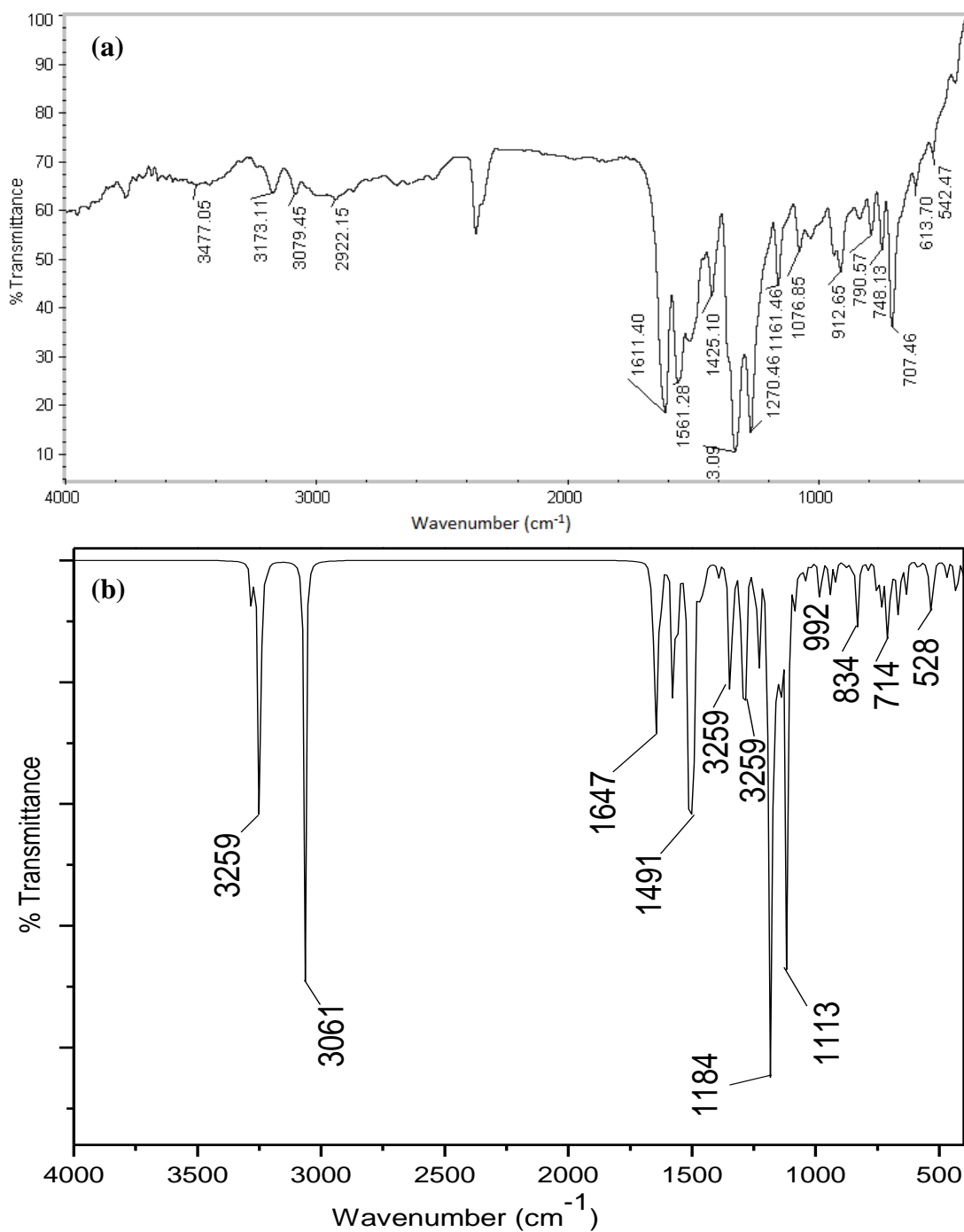


Fig.3.5.3 FT-IR spectra of BNAP (a) Experimental (b) Theoretical

Table 3.1.1 Comparison of the experimental and calculated vibrational spectra and proposed assignments of BAP

Mode no.	Experimental wavenumbers (cm ⁻¹)		Calculated wavenumbers (cm ⁻¹)			Vibration assignments with PED (≥ 10%)	
	FT-IR	<i>I</i> _{IR}	HF/6-31C(d,p)			Scaled	Frc const.
			Unscaled	Scaled	Frc const.		
1			4.39334	3751.51	3676.48	9.0631	V _{NH} (94)
2			6.81927	3678.34	3604.77	8.4223	V _{NH} (38)
3	3543.3		0.826758	3438.17	3369.41	7.6149	V _{CH} (51) + V _{CH} (48)
4			0.626837	3430.12	3361.52	7.5826	V _{CH} (48) + V _{CH} (51)
5	3066		100	3099.46	3037.47	6.1456	V _{NH} (56)
6	1983.96		12.5405	1956.76	1917.62	29.0615	V _{OC} (89)
7			72.7327	1913.06	1874.8	26.2434	V _{OH} (59)
8	1866.17		4.72335	1848.99	1812.01	2.2526	δ _{HNH} (57)
9	1629.05		9.81881	1645.34	1612.43	21.5001	V _{ON} (44)
10			36.4238	1609.8	1577.6	17.6506	V _{ON} (22)
11			4.5686	1606.77	1574.63	3.3323	δ _{HCC} (35) + V _{CC} (17)
12	1597.71		1.61062	1580.22	1548.62	3.7871	δ _{HCC} (35)
13	1571.38		3.36856	1578.05	1546.49	7.4852	δ _{HCC} (34) + V _{CC} (19)
14	1543.17		8.3809	1499.26	1469.27	4.5273	δ _{HCC} (16) + δ _{HCC} (18)
15	1506.59		42.5006	1496.58	1466.65	6.6362	V _{ON} (30)
16	1449.01		0.778937	1469.28	1439.89	1.7163	δ _{HCC} (58) + δ _{HCC} (15)
17	1362.51		0.675592	1348.03	1321.07	1.9411	δ _{HCC} (14) + δ _{HCC} (13) + δ _{HCC} (31) + V _{CC} (15)
18	1324.26		1.1552	1337.82	1311.06	2.7476	δ _{HCC} (24) + V _{CC} (23) + V _{CC} (12)
19	1284.91		0.506905	1284.3	1258.61	2.9031	δ _{HCC} (18) + V _{CC} (23) + V _{CC} (10) + V _{NH} (36)
20	1202.9		4.7895	1202.35	1178.3	1.5381	δ _{HCC} (13) + δ _{HCC} (19) + V _{CC} (11) + V _{CC} (13)
21	1081.48		0.160873	1089.81	1068.01	4.0936	V _{CC} (34) + V _{CC} (23) + V _{CC} (22)
22	975.88		1.34531	974.761	955.266	0.7655	τ _{HCCC} (18) + τ _{HCCC} (19) + τ _{HCCC} (27)
23	959.57		0.934728	967.126	947.783	0.7414	τ _{HCCC} (14) + τ _{HCCC} (43)
24	930.64		0.146519	938.433	919.664	0.8079	τ _{HCCC} (36) + τ _{HCCC} (26) + V _{ON} (10) + δ _{ONO} (59)
25	910.55		2.54593	912.861	894.604	5.2096	γ _{OCOM} (34) + γ _{OCOC} (15)
26	844.13		1.60699	836.895	820.157	3.8408	γ _{OCOM} (18) + γ _{OCOC} (40)
27			3.73457	818.54	802.169	0.777	τ _{HCCC} (10) + τ _{CCCC} (10) + γ _{OCOC} (17)
28	796.38		2.60074	795.8	779.884	4.3813	V _{NC} (12) + δ _{ONO} (40) + δ _{CCC} (22)
29	740.66		0.948404	745.8	730.884	1.3856	τ _{CCCC} (11) + γ _{OCOC} (40)
30			0.594829	730.059	715.458	2.2192	δ _{OCOC} (16) + δ _{ONC} (11) + δ _{NCC} (12)
31	704.73		0.258192	694.909	681.011	1.8936	δ _{CCC} (38) + δ _{CCC} (26)

v - stretching, γ - out of plane bending, δ - in plane bending, τ - torsion.
*I*_{IR} - IR intensity (km mol⁻¹).

Table 3.1.2. Frequencies of the fundamental vibrations of BNAP, picric acid (PA) and 2-amino-5-nitrobenzophenone/cm⁻¹

BNAP	PA *	2-amino-5-nitrobenzophenone	Assignment of vibration
1561	1523	-	$\nu_{as}NO_2$
1353	1337	1375	$\nu_s NO_2$
2922	-	-	$\nu CH (-CH_3)$
3079	-	-	$\nu NH (NH_3^+)$
3477	3425	3466	$\nu_s NH$
-	-	3337	$\nu_{as} NH$
1161	1153	1317 and 1156	$\nu C-O$
1611 and 1425	1632 and 1435	1617 and 1436	$\nu C=C$
-	3100	-	$\nu-OH$
707 and 748	728	743	ωNO_2
790	788	764	ϕNO_2

*Ref (17)

NMR spectral analysis

BAP is dissolved in 0.5 ml of CDCl₃ solvent and TMS (tetramethylsilane) was used as an internal standard. ¹H NMR spectrum of BAP is shown in **Fig.3.1.4a**. The signal at 9.20 ppm corresponds to NH₃ proton of the 4-aminobenzophenonium group. The multiplet appeared in the range 6.86-7.73 ppm corresponds to eleven aromatic protons. The signal at 2.18 ppm is due to acetone peak, ¹³C NMR spectrum of BAP is shown in **Fig.3.1.4b**. The signals at 195.3 ppm are due to the carbonyl carbon. The weak signals at 153.2, 147.8, 138.4 and 137.21 ppm are due to ipso carbons. The aromatic carbon signals appeared in the range of 115.5 - 132.7 ppm. The signals at 207.1 ppm (C=O) and 30.9 ppm (CH₃) are due to solvent acetone peak.

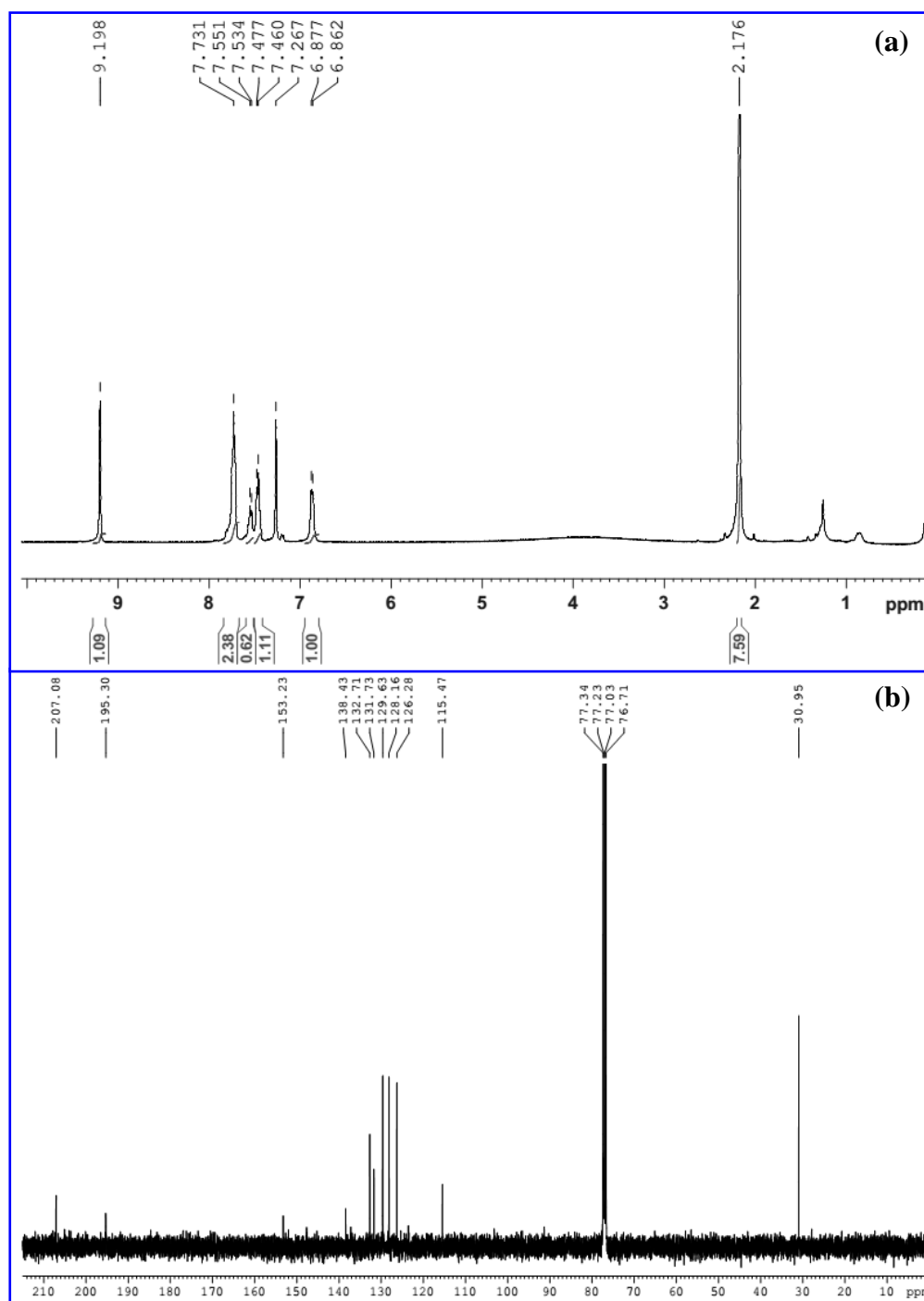


Fig.3.5.4 NMR spectra of BAP (a) ^1H (b) ^{13}C

^1H NMR spectrum of BNAP is shown in **Fig.3.1.5a**. The signal at 9.1 ppm corresponds to *ortho* proton of the picrate anion. The peak appeared in the range 8.30–8.40 ppm corresponds to three protons of ammonium ion. The peaks at the range of 6.7–8.0 are due to aromatic protons. ^{13}C NMR spectrum of BNAP is shown in **Fig.3.1.5b**. The signal at 197.94 ppm is due

to the carbonyl carbon. The weak signals at 155.3, 138.5 and 132.2 ppm are due to ipso carbon of the benzophenone ring. The weak signals at 153.2, 137.1 and 136.6 ppm are due to ipso carbon of the picrate anion. The aromatic carbon signals appeared in the range of 116.0–132.2 ppm. The signals at 77.39, 77.07 and 76.75 ppm are due to solvent (acetone) peak.

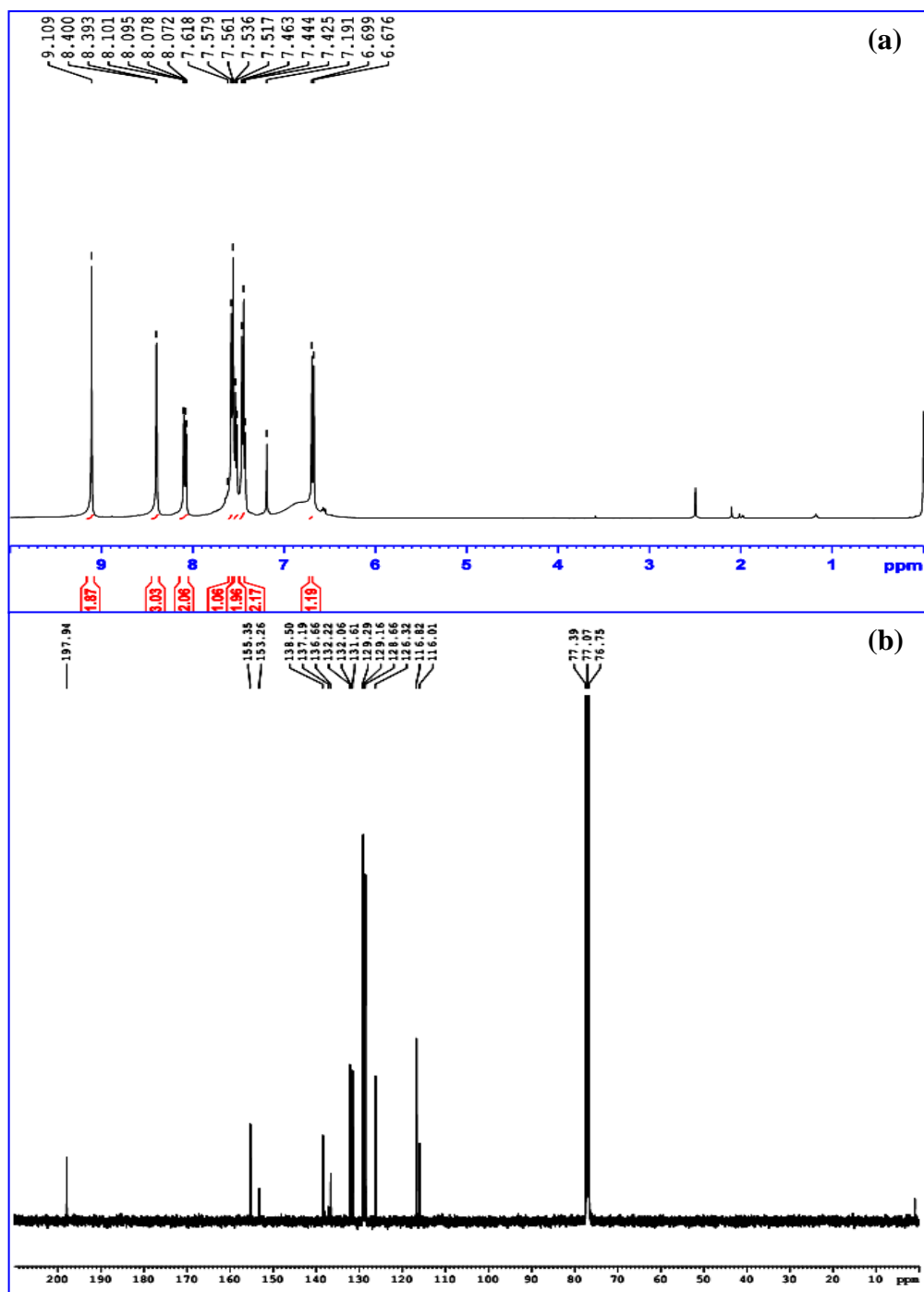


Fig.3.5.5 NMR spectra of BNAP (a) ^1H (b) ^{13}C

Optical absorbance studies

UV-vis spectrum of BAP was recorded using UV-1650PC UV-vis spectrophotometer. It shows minimum absorption in the visible region. Experimentally by using ethanol as a solvent, a peak is observed at the wavelength of ~344 nm (**Fig.3.1.6a**).

The optical absorption spectrum of BNAP shows good transmission in the visible region. The lower cut-off wavelength is ~300 nm and band gap energy of the specimen is deduced as 4.45 eV using the Tauc plot, $[F(R)h\nu]^2$ vs $h\nu$ (eV) (**Fig.3.1.7**) where $F(R)$ is Kubelka-Munk function [6], correlating reflectance and concentration.

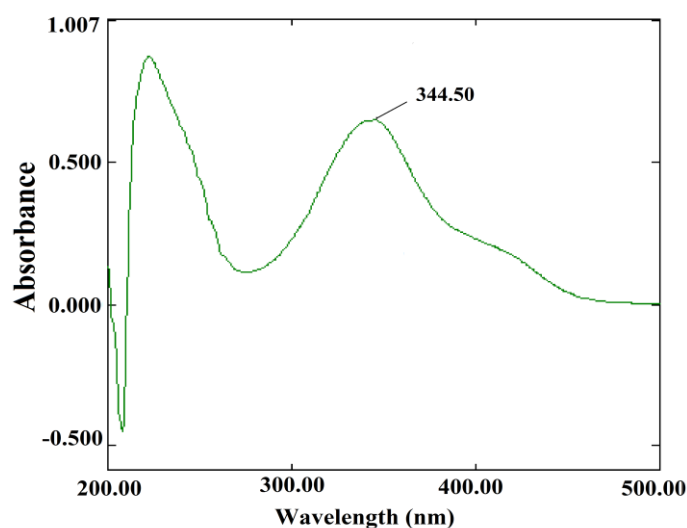


Fig. 3.1.6 UV-vis spectra of BAP

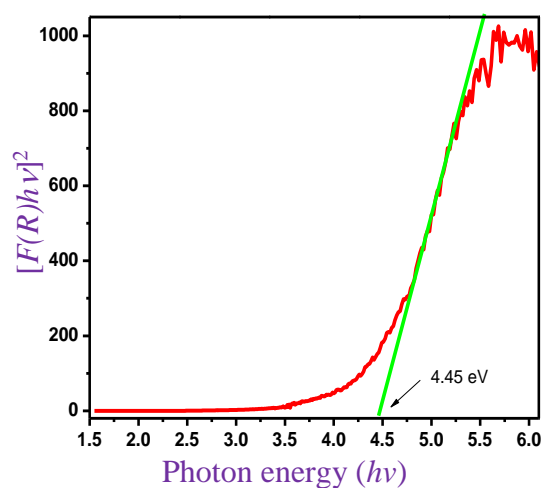


Fig.3.1.7 Tauc plot of BNAP

Thermal analysis

The thermal behavior of BAP was studied by the thermogravimetric and differential thermal analysis using a NETZSCH STA 449 F3 thermal analyzer in nitrogen atmosphere (**Fig.3.1.8a**). It is clear that there is no physically adsorbed water in the molecular structure of the crystal. TG curve shows a single stage weight loss at ~210 °C due to decomposition of BAP into fragments and its subsequent volatilization.

TG curve of BNAP shows a single stage mass loss at ~ 180 °C due to decomposition into fragments and its subsequent volatilization. In DTA, a sharp endothermic peak at ~ 140 °C is due to the melting point of the material. The sharpness of the endothermic peak shows good degree of crystallinity and purity of the material. TG/DTA curve of BNAP are shown in

Fig.3.1.8b.

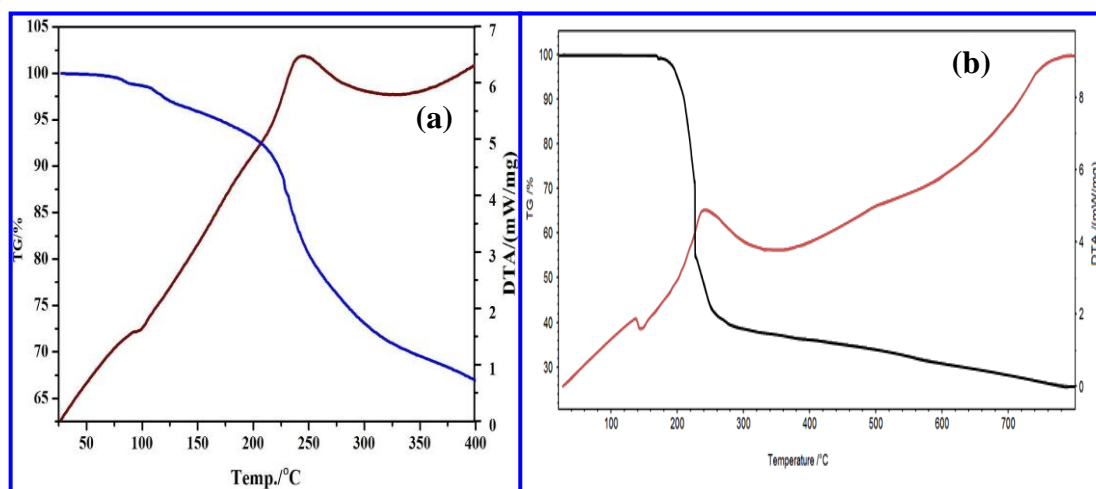


Fig.3.5.8 TG/DTA curve of (a) BAP (b) BNAP

Scanning electron microscopy (SEM)

The particles like images on the surface of both crystals could be due to the surface roughness. A dendritic growth, crack development and etch pits are observed (**Fig.3.1.9**).

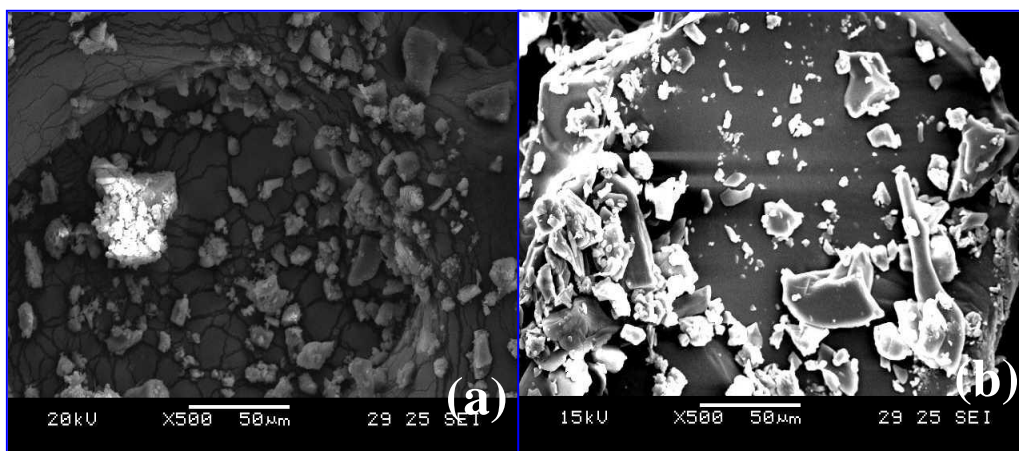


Fig.3.1.9 SEM photographs of (a) BAP (b) BNAP

NBO analysis

NBO calculations are performed using NBO 3.1 program as implemented in the GAUSSIAN09W [7] package using HF/6-31G (*d, p*) method. The second order Fock matrix was carried out to evaluate donor (i)-acceptor (j) that is donor level bands to acceptor level bonds interaction in the NBO analysis [8]. For each donor (i) and acceptor (j), the stabilization energy $E(2)$ associated with the delocalization $i \rightarrow j$ is estimated as,

$$E(2) = E_{ij} = q_i F(i,j)^2 / (\epsilon_j - \epsilon_i) \quad \text{Eqn. (3.1.1)}$$

where q_i is the donor orbital occupancy, $\epsilon_j - \epsilon_i$ are diagonal elements and $F(i,j)$ is the off-diagonal NBO Fock Matrix element. NBO analysis provides a best method for studying interaction among bonds and also provides the convenient basis for investigating charge transfer molecular systems [9, 10]. The larger the $E(2)$ value the more intensive is the donation tendency from electron donors to electron acceptors and the greater the extent of conjugation of the whole system [11]. Delocalization of electron density between occupied Lewis type (bond or lone pair) NBO orbital and formally unoccupied (antibond or Rydberg) non-Lewis NBO orbital corresponds to a stabilizing donor-acceptor interaction. NBO analysis has been performed on the BAP molecule in order to elucidate the intramolecular hybridization and delocalization of electron density within the molecule. The intramolecular hyperconjugative interactions are of $\pi(\text{C21-N24})$ orbital to $\sigma^*(\text{C20-C21})$; $\pi^*(\text{C21-N24})$ lead to strong stabilization energies of 38.06 and 38.86 kJ/mol, respectively. In case of $\sigma(\text{C5-C6})$ orbital to $\sigma^*(\text{C1-N7})$ the stabilization energy is 6.45 kJ/mol. The most important interaction energy in this molecule is electron donating from LP(O31) to the antibonding acceptor $\text{RY}^*(\text{N24})$ resulting in less stabilization energy of 3.56 kJ/mol. The same LP(O31) with $\pi^*(\text{C21-N24})$

leads to moderate stabilization energy of 1.29 kJ/mol. The maximum energy delocalization takes part in the π - π^* transition. The $E(2)$ values and types of the transition are shown in **Table 3.1.3**.

Table 3.1.3. Second order Perturbation theory analysis of Fock matrix in NBO basis for BAP

Donor (i)	ED(i)(e)	Acceptor (j)	ED(j)(e)	$E^{(2)}$ kJ mol	$E(j)-E(i)$ a.u	$F(i,j)$ a.u
σ (C1-C2)	1.9776	$\sigma^*(C1-C6)$	0.0204	5.76	1.79	0.09
σ (C1-N7)	1.9898	$RY^*(C2)$	0.0056	1.08	2.46	0.04
		$\sigma^*(C5-C6)$	0.0118	1.53	1.89	0.04
σ (C2-C3)	1.9762	$RY^*(1)C1$	0.0051	3.1	2.15	0.07
		$\sigma^*(C1-N7)$	0.0232	6.27	1.46	0.08
σ (C4-C5)	1.9758	$RY^*(C3)$	0.0063	0.66	2.39	0.03
		$\sigma^* (C3-C4)$	0.0196	4.61	1.77	0.08
σ (C5-C6)	1.9770	$\sigma^* (C1-N7)$	0.0232	6.45	1.47	0.08
σ (C10-C12)	1.9746	$\sigma^* (C10-C11)$	0.0205	5.14	1.75	0.08
		$\sigma^* (C12-C14)$	0.0130	3.09	1.78	0.06
σ (C17-C18)	1.9739	$RY^*(1)C16$	0.0064	0.99	1.97	0.04
		$\sigma^* (C19-N23)$	0.0700	5.28	1.5	0.08
		$\sigma^* (N25-O28)$	0.0413	2.84	1.66	0.06
σ (C18-C19)	1.9753	$RY^*(1)C17$	0.0080	2.14	2.42	0.06
		$RY^*(2)C17$	0.0075	1.54	2.4	0.05
		$\sigma^*(N23-O26)$	0.0483	2.52	1.71	0.05
σ (C19-N23)	1.9881	$RY^*(C18)$	0.0054	1.11	1.92	0.04
		$RY^*(C20)$	0.0169	1.35	1.74	0.04
σ (C20-C21)	1.9737	$RY^*\sigma C 16$	0.0064	1.86	1.92	0.05
		$\sigma^* (C20-O22)$	0.0062	1.24	1.78	0.04
		$\sigma^* (C21-N24)$	0.0519	0.63	1.52	0.02
π (C20-O22)	1.9838	$\pi^*(C18-C19)$	0.1978	4.46	0.68	0.05
		$\pi^*(C21-N24)$	0.6677	4.01	0.45	0.04
σ (C21-N24)	1.9876	$RY^*(1)C16$	0.0052	1.27	2.55	0.05
		$\sigma^* (C19-C20)$	0.0550	0.91	1.84	0.03
π (C21-N24)	1.6309	$\sigma^* (C20-C21)$	0.0582	38.06	0.6	0.13
		$\pi^* (C21-N24)$	0.6677	38.86	0.36	0.11
σ (N23-O26)	1.9952	$RY^* (C19)$	0.0071	0.85	2.78	0.04
		$RY^* (C19)$	0.0068	1.18	2.71	0.05
LP (N7)	1.6429	$LP^* (H36)$	0.4664	0.68	3.19	0.04
		$RY^*(H37)$	0.0073	0.78	3.12	0.04
LP (O29)	1.9816	$RY^* (N25)$	0.0176	7.11	2.47	0.11
LP (O30)	1.9683	$RY^* (N24)$	0.0148	3.97	2.21	0.08
LP (O31)	1.9328	$RY^* (N24)$	0.0148	3.56	2.27	0.08
		$\pi^* (C21-N24)$	0.6677	11.97	1.13	0.10

^aED is the occupation number

^b $E^{(2)}$ is the energy of hyperconjugative interactions.

^cEnergy difference between donor and acceptor of i and j NBO orbitals.

^d $F(i, j)$ is the Fock matrix element between i and j NBO orbitals

Molecular electrostatic potential (MEP)

The MEP is a plot of electrostatic potential mapped on the constant electron density surface displaying electrostatic potential (electron+nuclei) distribution. The different values of the electrostatic potential at the surface are represented by different colours; red represents regions of most negative electrostatic potential (preferred site for electrophilic attack), blue represents regions of most positive electrostatic potential (preferred site for nucleophilic attack) and green represents regions of zero potential. To predict reactive sites for electrophilic and nucleophilic attack for BAP, the MEP was mapped with the total density of the molecule. As can be seen in **Figs.3.1.10a and b** red indicates the more electron rich and blue the more electron poor area. Furthermore, the polarization effect is clearly visible.

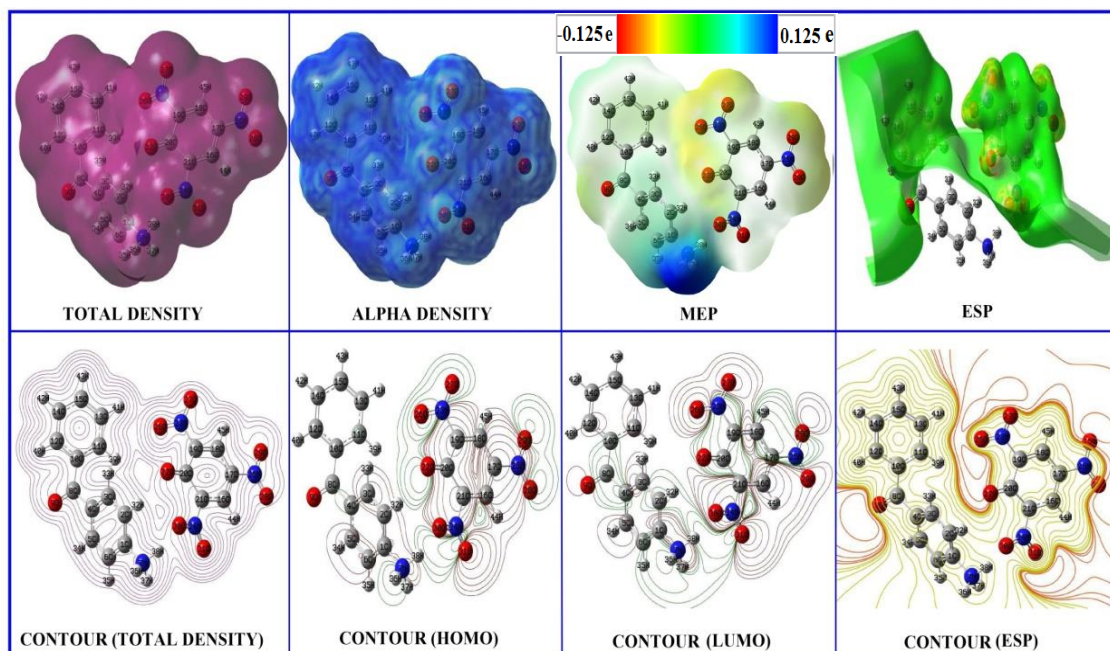


Fig.3.5.10a Molecular surfaces obtained using HF/6-31G(d,p) level

The colour code of this map for BAP is in the range between -0.125 to $+0.125$ e and for BNAP it is -9.105 e^{-2} to $+9.105 \text{ e}^{-2}$. Molecular shape, size and dipole moment of the molecule provide a visual method to understand the relative polarity [12]. As can be seen from the MEP map of the molecule, the negative region is mainly localized from nitro and carbonyl groups whereas the positive region lies in the six membrane aromatic ring system.

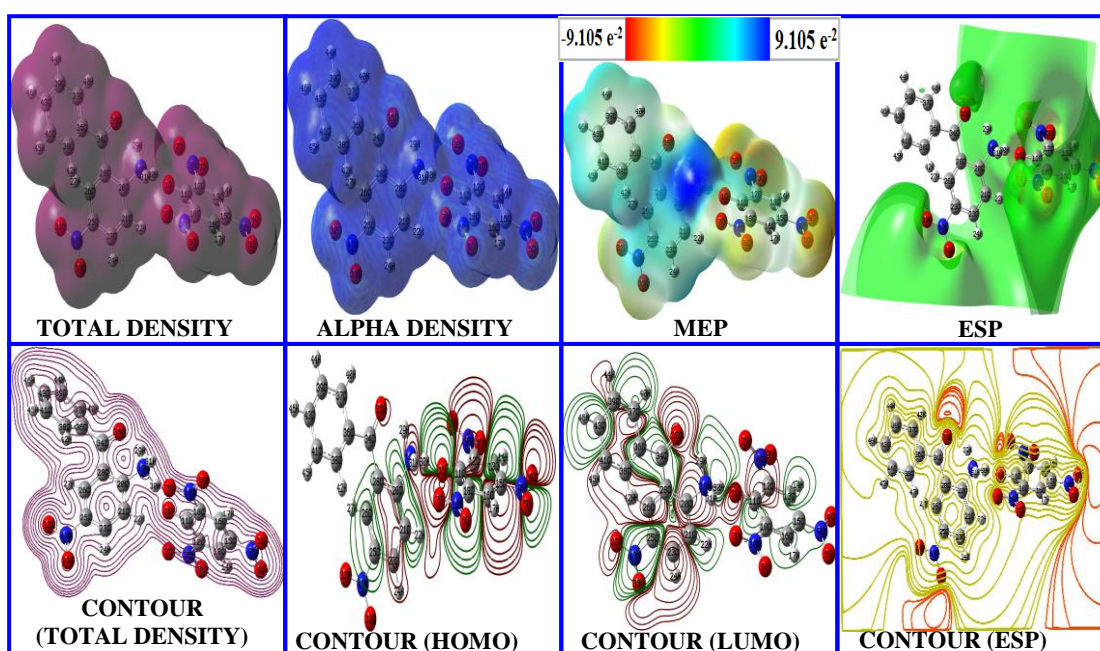


Fig.3.5.10b Molecular surfaces obtained using HF/6-31G(d,p) level

The highest occupied molecular orbital (HOMO) and lowest unoccupied molecular orbital (LUMO) of BAP and BNAP are shown in **Figs.3.1.11a** and **b** respectively. The frontier orbital gap facilitates in characterizing the chemical reactivity and kinetic stability of the molecule. The red and green colors represent the positive and negative values for the wave function. The HOMO is the orbital that primarily acts as an electron donor and the LUMO is the orbital that mainly acts as an electron acceptor [13, 14].

The energy gap between HOMO (-0.1603 a.u.) to LUMO (-0.013 a.u.) of the molecule is about 0.1602 a.u. for BAP and it is -0.3437 a.u. for BNAP. The HOMO and LUMO energy gap explains the eventual charge transfer interactions taking place within the molecule.

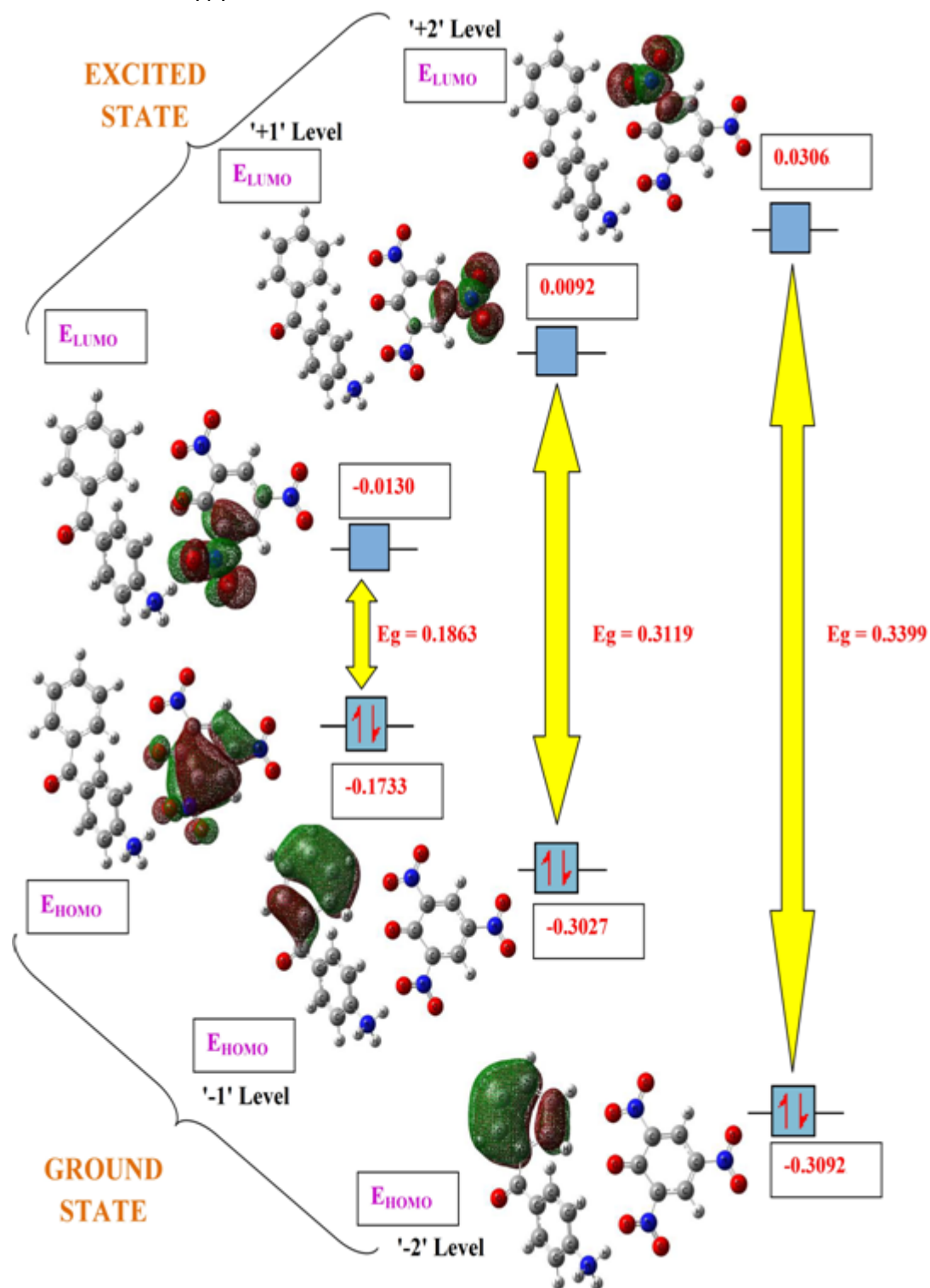


Fig. 3.1.11a HOMO-LUMO energy gap of BAP

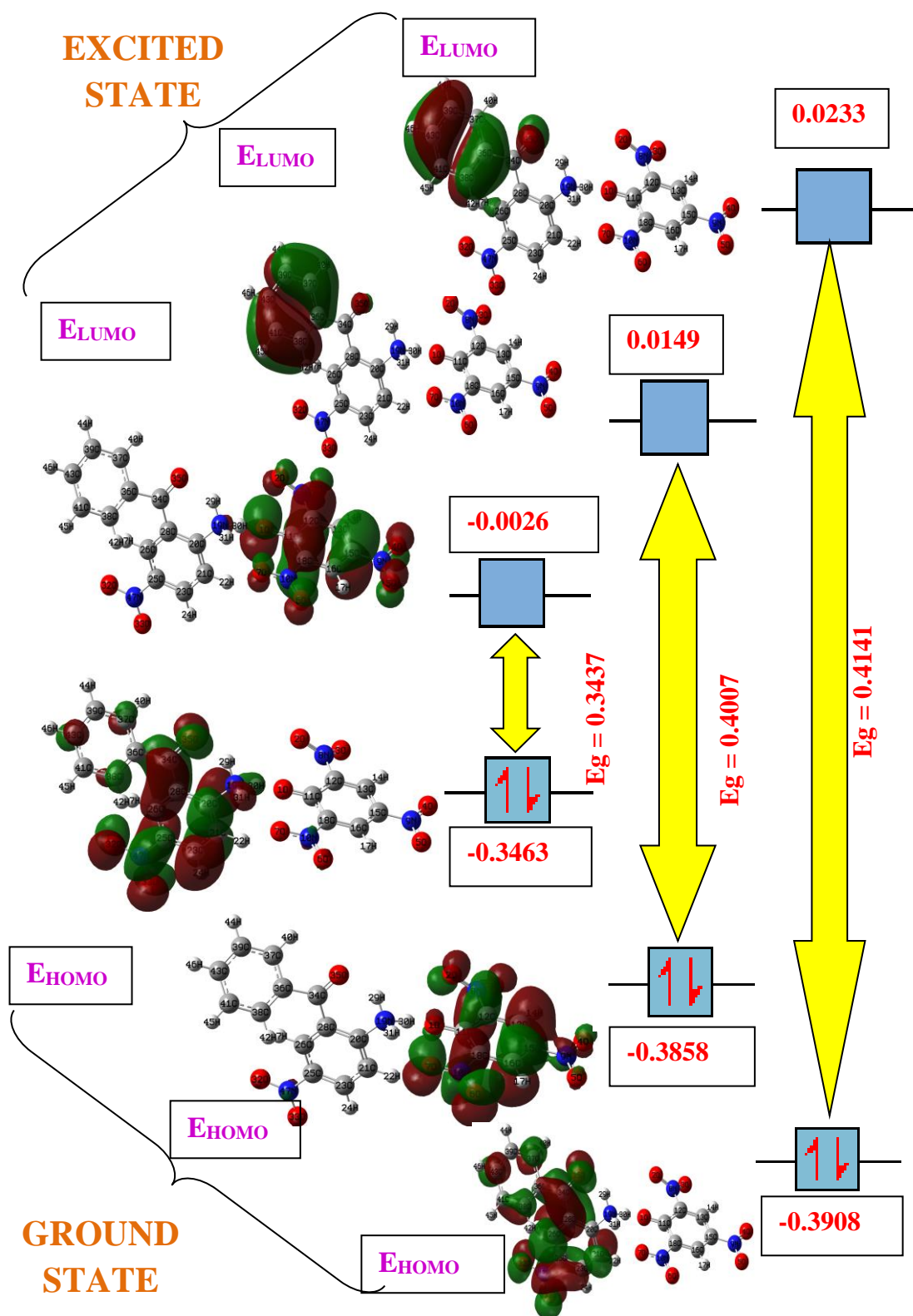


Fig. 3.5.11b HOMO-LUMO energy gap of BNAP

Mulliken [15] has derived the wave functions for the ground state and excited states of the complex and the charge distribution over the atoms thus provides a way of examining the proton transfer process. The proton transfer occurs from picric acid to pyridine. The charge distributions calculated by the Mulliken method [16] for the equilibrium geometry of BAP, BNAP are given in **Tables 3.1.4a and b**. The charge distribution on the molecule has an important influence on the vibrational spectra. Optimized molecular structure and Mulliken charge transfer of BAP and BNAP are shown in **Fig.3.1.12**.

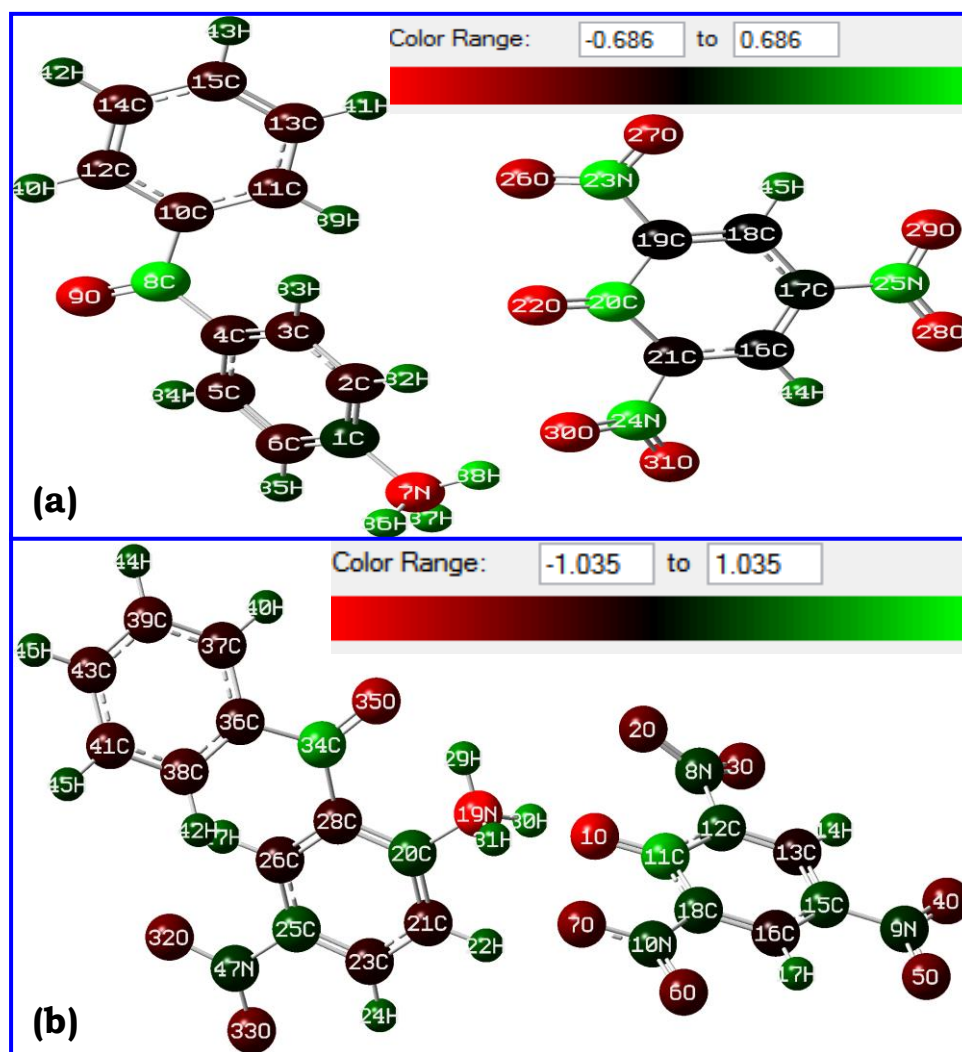


Fig.3.5.12 Mulliken charge transfer indicated by colour (a) BAP (b) BNAP

Conclusions

4-Benzoylanilinium picrate and 2-benzoyl-4-nitroanilinium picrate crystals were grown and characterized. The functional groups present in the molecule are confirmed by FT-IR analysis. The product formation was also confirmed by NMR spectral analysis. Scanning electron microscopic study gives information about the surface morphology of the specimens. TG/DTA reveals thermal stability of the as-grown crystal. MEP at the HF/6-31G(*d,p*) method was mapped with the total density of the molecule. HOMO and LUMO energy gap explains the eventual charge transfer interactions taking place within the molecule. Mulliken charge transfer indicates the charge distribution over the atoms thus providing a way of examining the proton transfer process. The crystal cohesion is achieved by intermolecular hydrogen bonds between picrate anion and amino group.

References

- [1] K. Muthu, SP. Meenakshisundaram, *Mater. Lett.*, **84** (2012), 56–58.
- [2] K. Muthu, SP. Meenakshisundaram, *J Cryst. Growth.*, **352** (2012), 163–166.
- [3] K. Muthu, SP. Meenakshisundaram, SC. Mojumdar, *J Therm Anal Calorim.*, **112** (2013), 1039–1045.
- [4] Michał H. Jamróz, *Spectrochimica Acta Part A: Molecular and Biomolecular Spectroscopy*, **114** (2013), 220.
- [5] P. Pulay, G. Fogarasi, G. Pongor, J. E. Boggs, A. Vargha, *J. Am. Chem. Soc.*, **105** (1983), 7037.

- [6] P. Kubelka, F. Munk, Ein Beitrag zur Optik der Farbanstriche. *Z Tech Phys.*, **12** (1931), 593–601.
- [7] M. J. Frisch *et al*, Gaussian 09 Revision-C.01, Gaussian, Inc., Wallingford, CT, (2009).
- [8] M. Szafran, A. Komasa, E. B. Adamska, *J. Mol. Struct. (Theochem)*., **827** (2007), 101.
- [9] C. James, A. Amal Raj, R. Rehunathan, I. Hubert Joe, V. S. Jayakumar, *J. Raman Spectrosc.*, **379** (2006), 1381.
- [10] L. Junna, C. Zhi-rang, Y. Shen-fang, J. Zhejiag, *Univ. Sci.*, **6B** (2005), 584.
- [11] S. Sebastin, N. Sundaraganesan, *Spectrochimica Acta Part A: Molecular and Biomolecular Spectroscopy*, **75** (2010), 941–952.
- [12] I. Fleming, *Frontier Orbitals and Organic Chemical Reactions*, *John Wiley and Sons*, New York (1976), 5.
- [13] K. S. Thanthiriwatte, K. M. Nalin de Silva. *J. Mol. Struct. (Theochem)*., **617** (2002),169.
- [14] P. S. Liyange, R. M. de Silva, K. M. Nalin de Silva. *J. Mol. Struct. (Theochem)*., **639** (2003),195.
- [15] R. S. Mulliken, *J. Am. Chem. Soc.*, **74** (1952), 811.
- [16] R. S. Mulliken, *J. Chem. Phys.*, **23** (1955),1833.
- [17] S. Anandhi, T.S. Shyju, R. Gopalakrishnan, *J Cryst. Growth.*, **312** (2010), 3292.

CHAPTER-3.2

Synthesis, growth, structure, hyperpolarizability and supramolecular architecture of some organic picrate crystals

Supramolecular single crystals of (2-aminobenzyl)methylammonium-picrate, 1-benzylpiperidyl-4-ammonium picrate, (diaminomethyl)sulfonium picrate and 4-formyl-N,N-dimethylbenzenammonium picrate were synthesized and grown by slow evaporation technique. Inter- and intramolecular hydrogen bonding interactions exhibit supramolecularity in the crystal packing, designed by weak N-H \cdots O, C-H \cdots O, N-H \cdots π and $\pi\cdots\pi$ molecular interactions. Different types of supramolecularity such as, 3D stacking model of packing projection, zipper-like structure and sandwich model of packing are observed. The first-order molecular hyperpolarizability values were estimated for all the four compounds. Hirshfeld surfaces were derived from single crystal X-ray diffraction data. Investigation of the intermolecular interactions *via* Hirshfeld surface analysis reveals the close contacts associated with strong interactions. Fingerprint analysis was used to locate, analyse and quantify all bonding interactions.

Introduction

Picric acid has ability to form the salts and charge transfer molecular complexes with many organic compounds particularly with aromatic amines [1, 2]. These picrates are convenient for identification and quantitative analysis of organic compounds. Similar type of organic picrates has been reported earlier [3-5].

Here, we report some novel picrates possessing high first-order molecular hyperpolarizability and hence, suitable for nonlinear optical applications. The hydrogen bonding interactions and molecular motifs developed in this crystal structure are highlighted and their influence on the packing projections was demonstrated. All four specimens were characterized by UV-DRS, thermal analysis and Density functional theory computations.

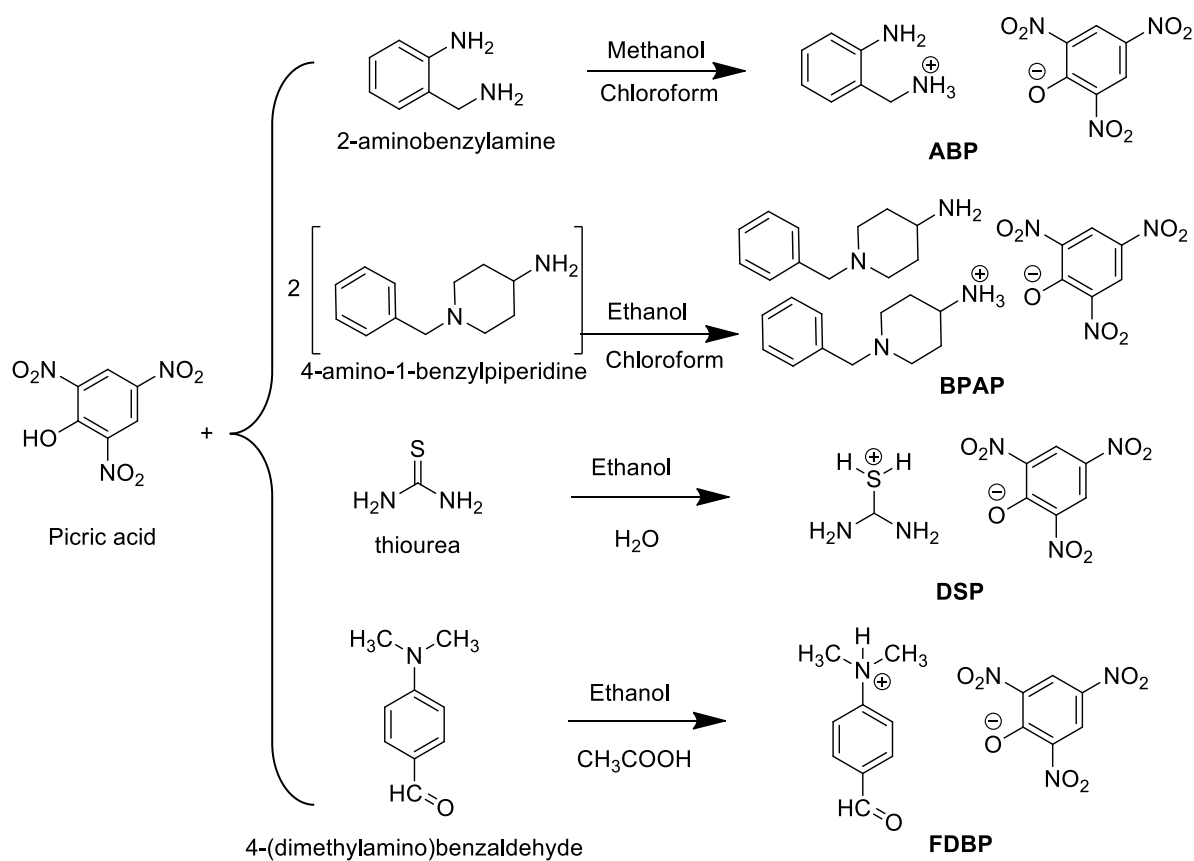
Synthesis and crystal growth

2-Aminobenzylaminium picrate (ABP) was synthesized by mixing stoichiometric quantities of 2-aminobenzylamine (Aldrich) and picric acid (Aldrich) in the molar ratio of 1:1 (Scheme I). The reactants were dissolved in a mixed solvent system of methanol-chloroform (2:1, v/v) and thoroughly mixed using a magnetic stirrer for about 5 h. The solution was filtered and kept in constant temperature water bath for about 10 d. Single crystals of ABP were grown from mixed solvent by slow evaporation solution growth technique at constant temperature (20°C) and quality crystals were harvested after 10-12 d. Tiny crystals also appeared at the bottom of the container due to secondary nucleation (**Fig.3.2.1a**).

1-Benzylpiperidyl-4-ammonium picrate (BPAP) was synthesized by mixing stoichiometric quantities of 4-amino-1-benzylpiperidine and picric acid in the molar ratio of 2:1 (**Scheme 1**). The reactants were dissolved in mixed solvent ethanol-chloroform (2:1, v/v), thoroughly mixed using a magnetic stirrer. Single crystals of BPAP were grown from their ethanol-chloroform (2:1, v/v) solution using slow evaporation solution growth technique. Good

crystals were harvested after a period of 10–12 d. Photographs of as-grown crystals are shown in **Fig.3.2.1b**.

(Diaminomethyl)sulfonium picrate (DSP) was synthesized by mixing stoichiometric quantities of thiourea and picric acid in the molar ratio of 1:1 (Scheme I). The reactants were dissolved in mixed solvent ethanol-water (1:1, v/v), thoroughly mixed using a magnetic stirrer. Single crystals of DSP were grown by slow evaporation solution growth technique. Good crystals were harvested after a period of 10–12 d. Photographs of as-grown DSP crystals are shown in **Fig.3.2.1c**.



Scheme I

4-Formyl-N,N-dimethylbenzenammonium picrate (FDBP) was synthesized by mixing stoichiometric quantities of 4-(dimethylamino)benzaldehyde (Aldrich) and picric acid (Aldrich) in the molar ratio of 1:1 (Scheme I). The reactants were dissolved in mixed solvent ethanol-acetic acid (1:1, v/v), thoroughly mixed using a magnetic stirrer. Single crystals of FDBP were grown by slow evaporation solution growth technique. Good crystals were harvested after a period of 10–12 d. Photographs of as-grown FDBP crystals are shown in

Fig.3.2.1d.



Fig.3.2.1. The as-grown crystals of
 (a) (2-aminobenzyl)methylammonium picrate
 (b) 1-benzylpiperidyl-4-ammonium picrate
 (c) (diaminomethyl)sulfonium picrate
 (d) 4-formyl-N,N-dimethylbenzenammonium picrate

Results and discussion

Single crystal XRD analysis

Structures of all picrates were elucidated by single crystal X-ray diffraction analysis. The *ORTEP* of all the four compounds are displayed in **Fig.3.2.2** and the corresponding crystal data are listed in **Table 3.2.1**.

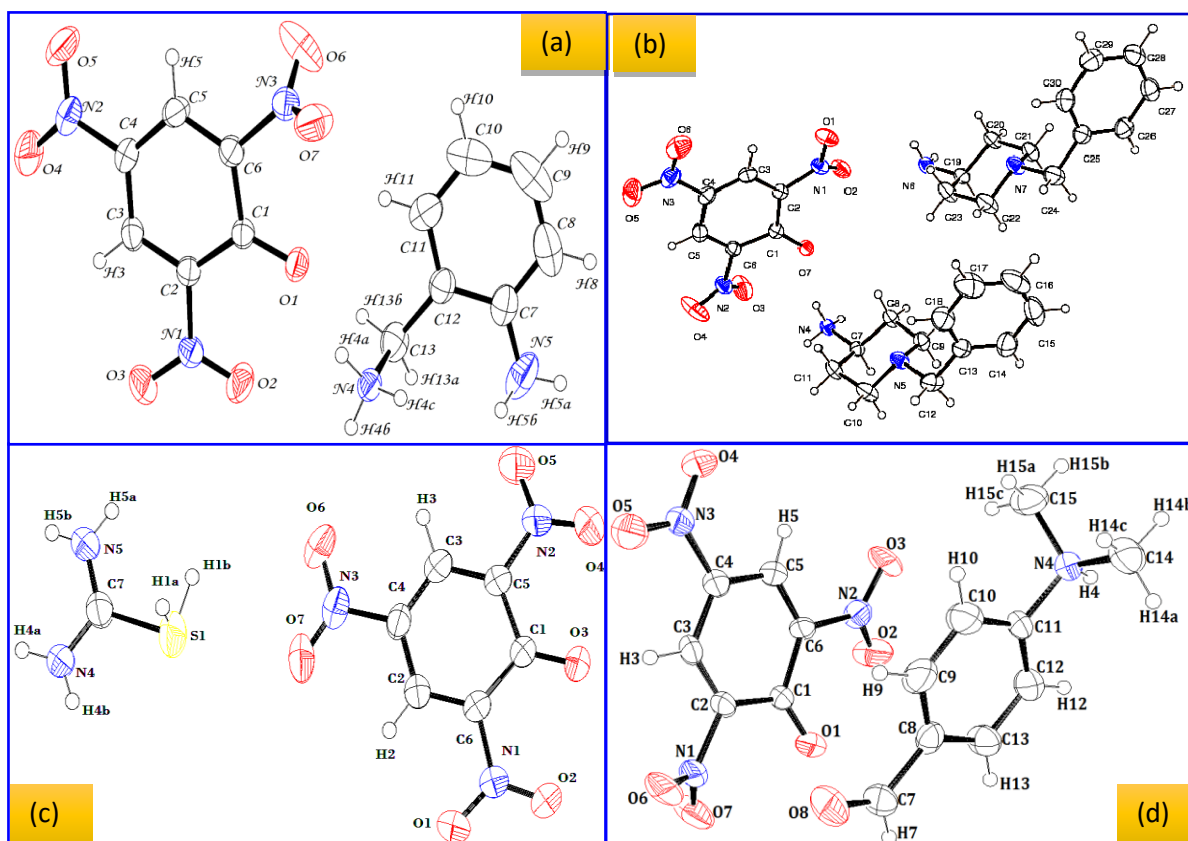


Fig.3.2.2. ORTEP of (a) (2-aminobenzyl)methylammonium picrate
 (b) 1-benzylpiperidyl-4-ammonium picrate
 (c) (diaminomethyl)sulfonium picrate
 (d) 4-formyl-N,N-dimethylbenzenammonium picrate

ABP

X-ray diffraction analysis reveals that the crystal structure is designed with inter- and intramolecular hydrogen bonding interactions. It belongs to the triclinic crystal system with space group $P\bar{1}$ consisting of two molecules in an unit cell. Crystal structure exhibits supramolecular column-like packing projection and ionic-bonded network structure along the a-axis (**Fig.3.2.3**). This column is formed by the picrate anion (yellow) with the protonated 2-aminobenzylammonium (green colour). In **Fig.3.2.3c**, a red circle clearly represents the hydrogen bonding interactions between phenolic ring oxygen to aminium group hydrogen, which are constructed with the bond distances of 1.813 and 1.827 Å. Each column developed through picrate to picrate

bridging interactions of the hydrogen atoms of the phenolate ring (O \cdots H), indicated as 'B' in **Fig.3.2.3c** assembled with bond distances of about 2.478 and 2.573 Å. Picrate–amine edge-to-edge interactions between the hydrogen atoms appear as a bridge like structure indicated by 'A' in **Fig.3.2.3c**, formed with a bond distance of 2.578 Å. Strong N–H \cdots O intermolecular interactions were assembled like a sandwich model of packing with distances of 1.925 and 2.248 Å (**Fig.3.2.4**).

Table 3.2.1. Crystal data and structure refinement

	ABP	BPAP	DSP	FDBP
Empirical formula	C ₁₃ H ₁₃ N ₅ O ₇	C ₃₀ H ₃₉ N ₇ O ₇	C ₇ H ₈ N ₅ O ₇ S	C ₁₅ H ₁₄ N ₄ O ₈
Formula weight	351.28	609.68	306.24	378.30
Temperature/K	273	293(2) K	298.15	293
Crystal system	triclinic	Triclinic,	monoclinic	monoclinic
Space group	<i>P</i> $\bar{1}$	<i>P</i> $\bar{1}$	<i>C</i> 2/ <i>c</i>	<i>P</i> 2 ₁ / <i>c</i>
<i>a</i> /Å	7.6398(8)	<i>a</i> = 11.8580(2)	13.2932(15)	9.749(10)
<i>b</i> /Å	7.8926(8)	<i>b</i> = 12.4560(3)	20.945(2)	10.789(11)
<i>c</i> /Å	12.9154(11)	<i>c</i> = 13.1700(2)	9.6005(11)	15.784(16)
α /°	78.501(8)	95.1220(10)	90	90
β /°	77.653(8)	106.8110(10)	113.844(2)	90
γ /°	86.996(8)	117.5550(10)	90	90
Volume/Å ³	745.45(13)	1592.85(5)	2444.9(5)	1660(3)
<i>Z</i>	2	2	8	4
ρ calc/gcm ³	1.5649	1.271	1.6638	1.5133
μ /mm ⁻¹	0.130	0.092	0.309	0.125
<i>F</i> (000)	364.2	648	1257.8	784.5
Crystal size/mm ³	1.0 × 0.8 × 0.6	0.35 x 0.30 x 0.25	0.3 × 0.3 × 0.25	0.3 × 0.3 × 0.25
Reflections collected	-5 ≤ <i>h</i> ≤ 9, -9 ≤ <i>k</i> ≤ 9, -16 ≤ <i>l</i> ≤ 16	-14 ≤ <i>h</i> ≤ 14, -14 ≤ <i>k</i> ≤ 14, -	-16 ≤ <i>h</i> ≤ 16, -25 ≤ <i>k</i> ≤ 25, -11 ≤ <i>l</i> ≤ 11	-11 ≤ <i>h</i> ≤ 12, -13 ≤ <i>k</i> ≤ 12, -19 ≤ <i>l</i> ≤ 19
Final R indexes [<i>I</i> ≥ 2 σ (<i>I</i>)]	R1 = 0.0189, wR2 = 0.0293	R1 = 0.0494, wR2 = 0.1386	R1 = 0.0342, wR2 = 0.0276	R1 = 0.3113, wR2 = 0.5000
CCDC number	CCDC1009556	CCDC1430063	CCDC1061333	CCDC1430067

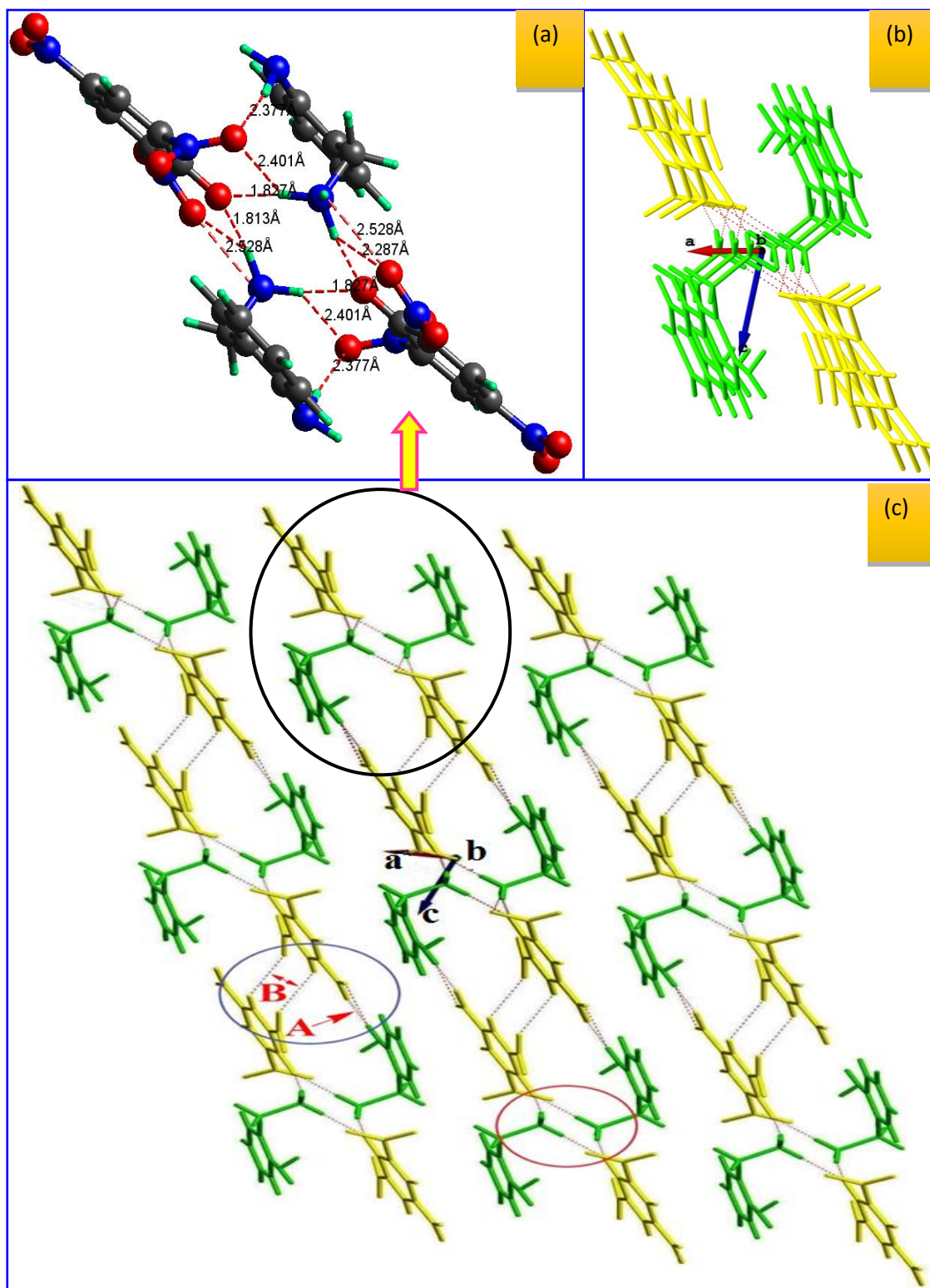


Fig.3.2.3. (a) Molecule representing weak and strong N-H...O interactions along a-axis (b) 3-Dimensional View (c) 2-Dimensional crystal packing projection of columnar hydrogen bonded network structure along a-axis

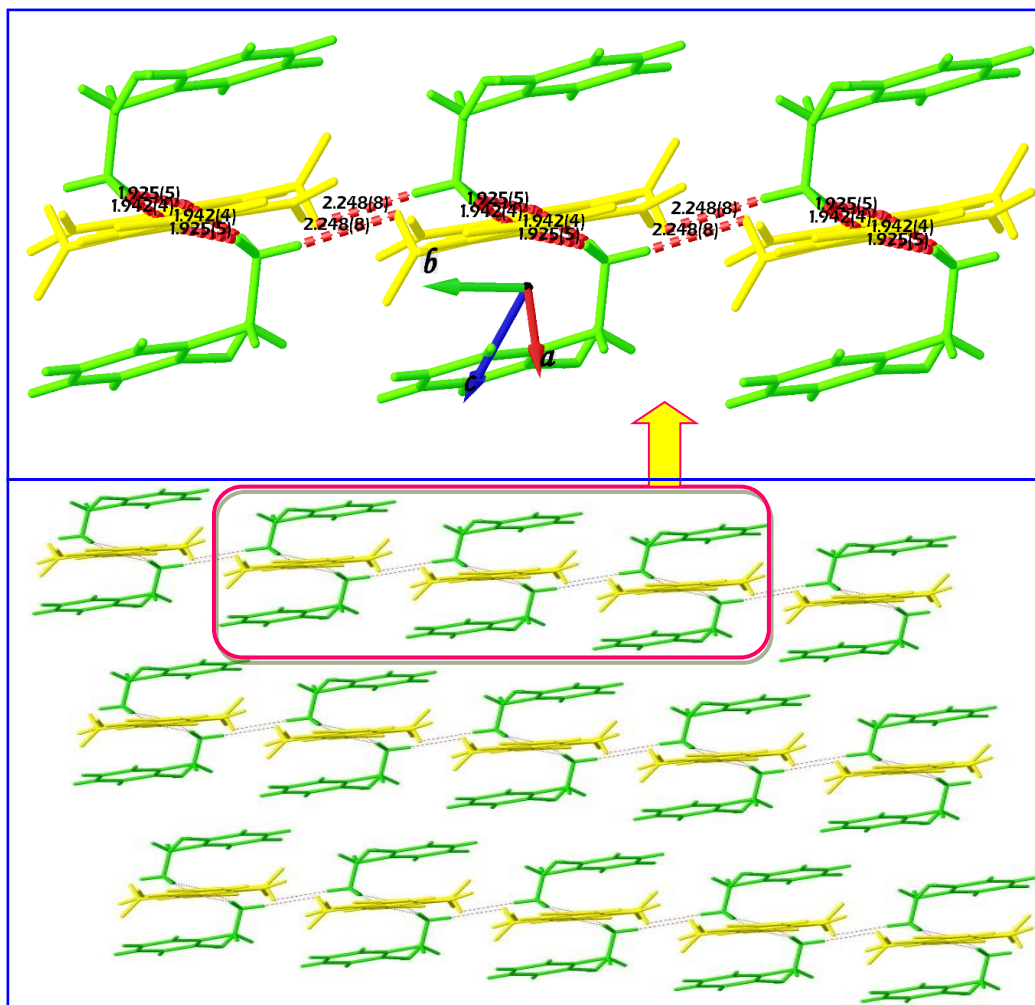


Fig.3.2.4. 2D view of sandwich modeled crystal packing projection

BPAP

BPAP belongs to the triclinic system with space group $P\bar{1}$ consisting of two molecules in an unit cell. Due to weak and strong intramolecular hydrogen bonding interactions, the picrate anion and aminium cation arranged as a box like strategy with stable packing motif. The weak C–H \cdots O intermolecular interactions with well-defined packing projection are displayed in **Fig.3.2.5**. As a consequence this molecule exhibits both inter- and intra molecular hydrogen bonding interactions with a distinct supramolecularity.

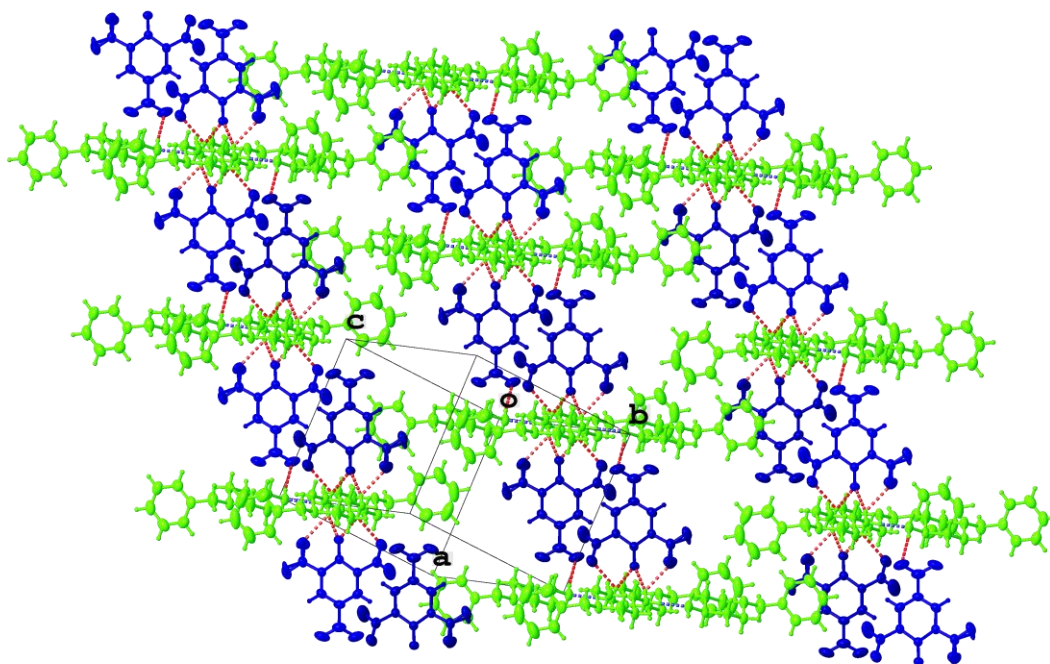


Fig.3.2.5. Packing projections of N-H...O interactions in BPAP

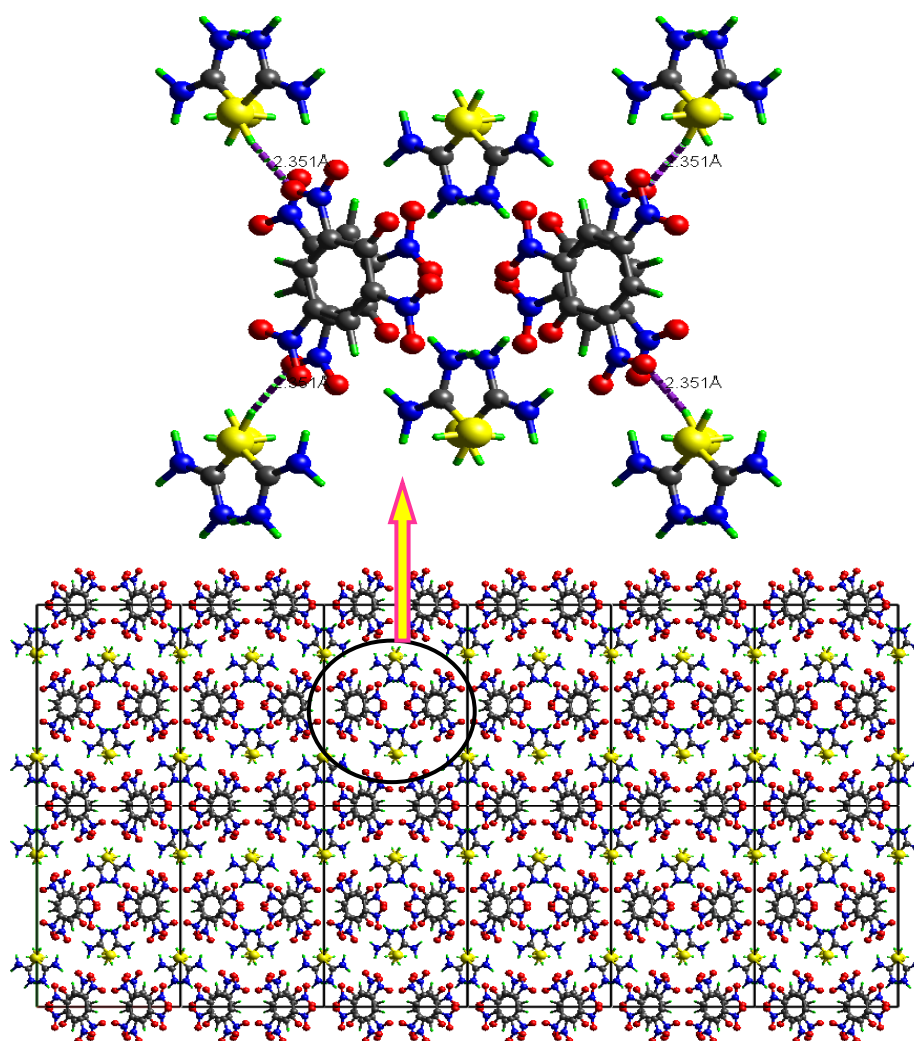


Fig3.2.6. Packing projections of S-H...O interactions in DSP

DSP

DSP belongs to the monoclinic crystal system with space group $C2/c$ consisting of eight molecules in an unit cell. Crystal cohesion is achieved by strong and weak $S-H\cdots O$ and $C-H\cdots O$ intermolecular interactions (**Fig.3.2.6**). The $S-H\cdots O$ interactions were assembled by distances of 2.507 and 2.35 Å.

FDBP

FDBP belongs to the monoclinic crystal system with space group $P2_1/c$ consisting four molecules in an unit cell. Crystal cohesion is achieved by $N-H\cdots O$ intermolecular interactions. The $C-H\cdots O$ and $N-H\cdots O$ interactions were assembled with a distance of 2.351 Å (**Fig.3.2.7**).

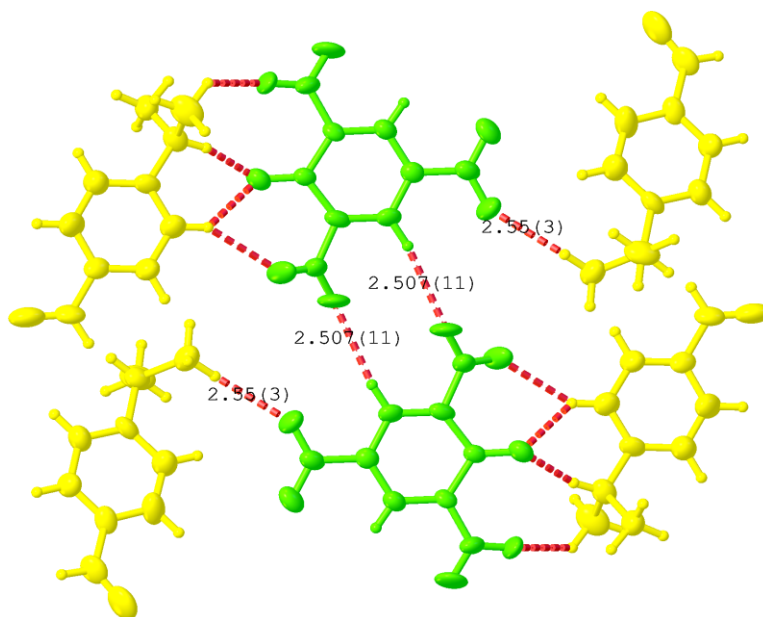


Fig.3.2.7. Packing projections of $C-H\cdots O$ interactions in FDBP

Powder-XRD analysis

In order to investigate the bulk formation behaviour of this supramolecular system, the X-ray powder diffraction patterns were recorded. Experimental

peaks coincide with simulated PXRD patterns (**Fig.3.2.8**). Sharp peaks indicate the good crystallinity of the synthesised compounds.

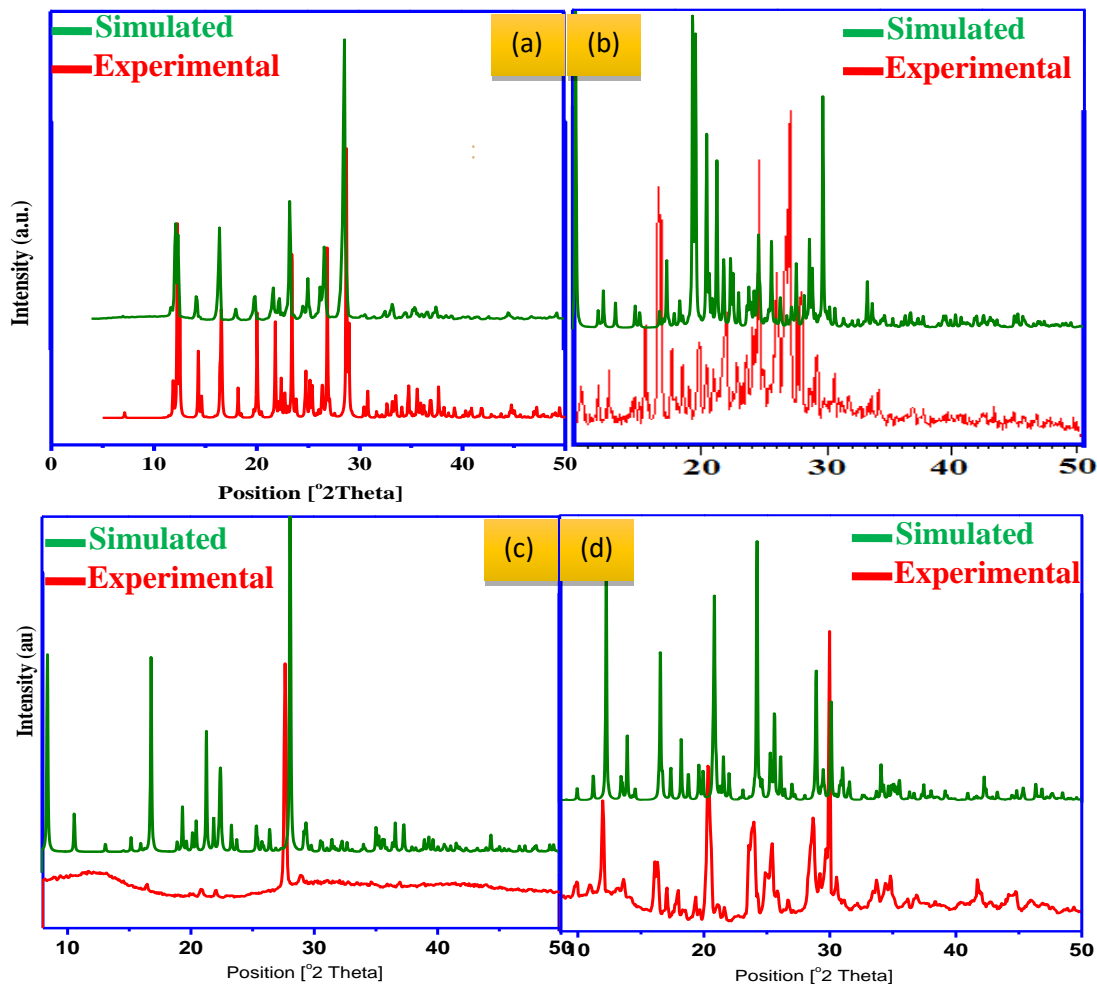


Fig.3.2.8. Experimental and simulated powder XRD patterns

(a) ABP (b) BPAP (c) DSP and (d) FDBP

Scanning Electron Microscopy

The SEM micrographs of the as-grown specimens are shown in **Fig.3.2.9**. Lot of imperfections are observed and the surface roughness could be due to macro steps. It reveals patches and defect centers with crystal voids.

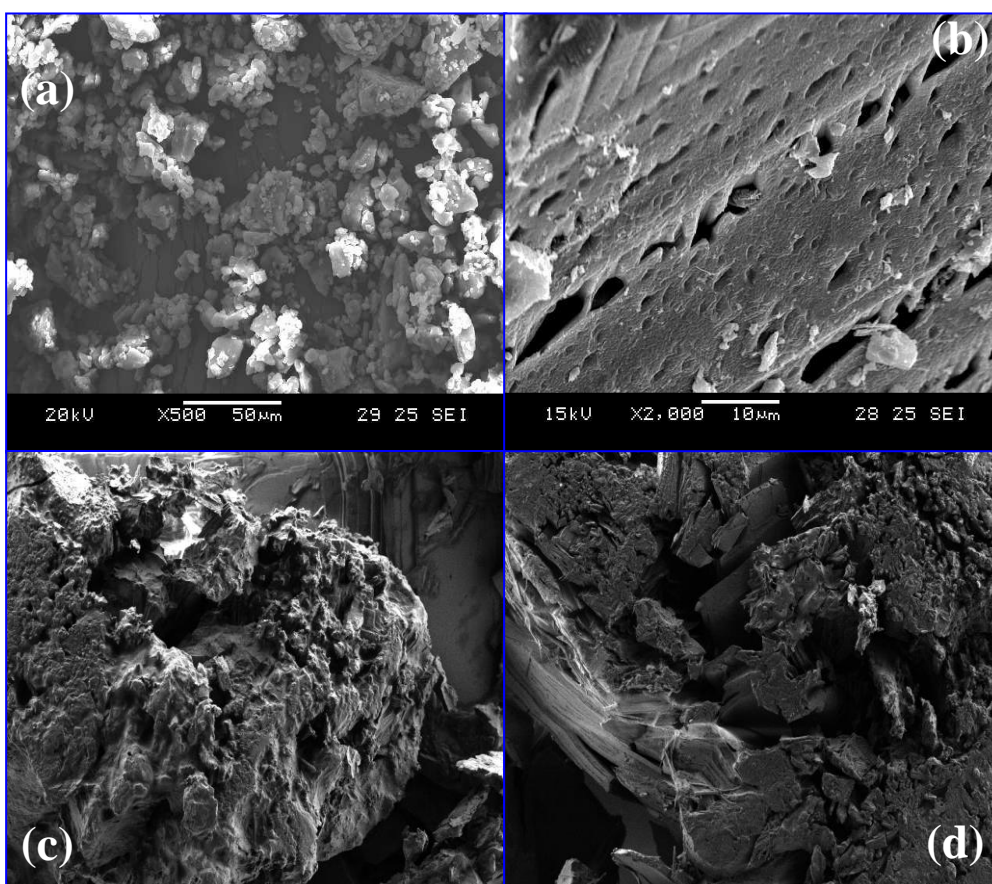


Fig.3.2.9. Scanning electron microscopic images of
 (a) ABP
 (b) BPAP
 (c) DSP and
 (d) FDBP

Hirshfeld surface analysis

The Hirshfeld surfaces (6) of all specimens are exhibited in **Fig.3.2.10**, showing surfaces that have been mapped over a *dnorm*. The surfaces representing the circular depressions (deep red) are indicative of hydrogen bonding contacts and other visible spots are due to $O\cdots H$, $H\cdots O$ and $O\cdots O$ contacts. The dominant interactions such as $O\cdots H$ can be seen in *dnorm* surface plots as the bright red area in **Fig.3.2.10**.

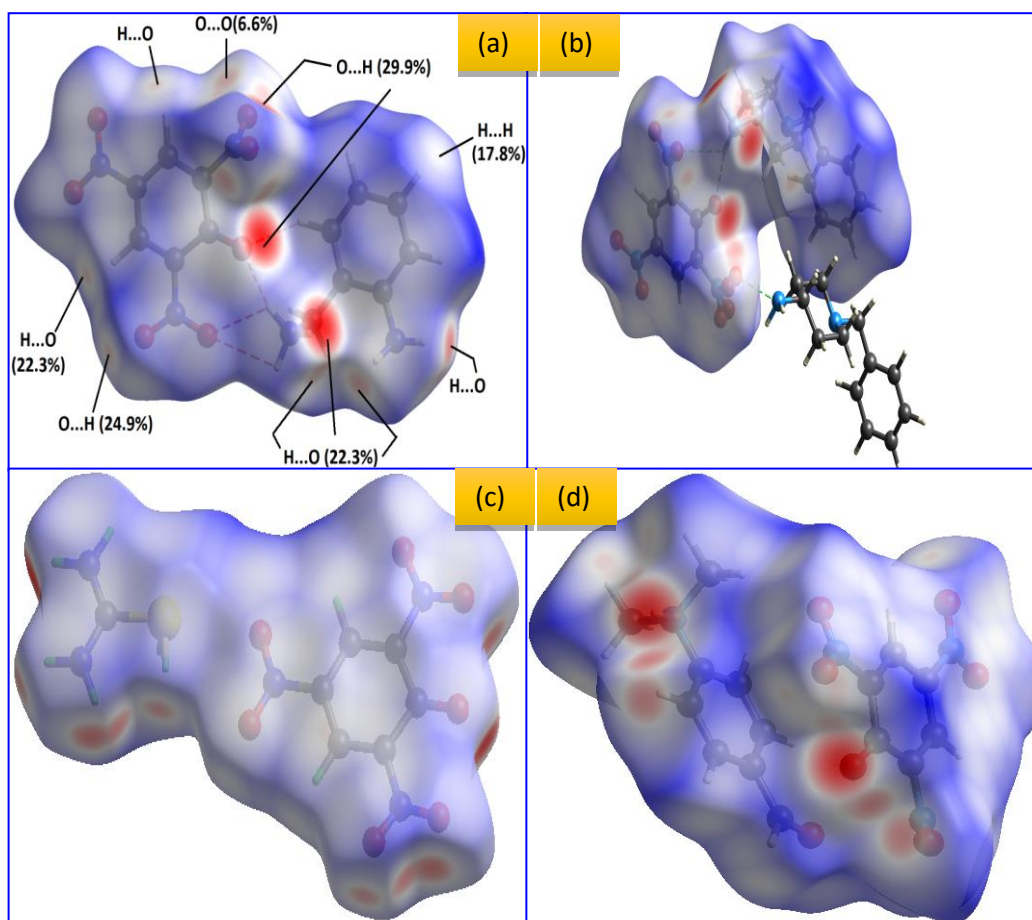


Fig.3.2.10. Hirshfeld surfaces of (a) ABP (b) BPAP (c) DSP and (d) FDBP

Fingerprint analysis

The two-dimensional fingerprint plots [7, 8] illustrate the picture of intermolecular interaction patterns. In the fingerprint region (**Fig.3.2.11**), the O...H interactions are represented by a spike at the bottom area whereas H...O interactions are represented by a spike at the top left region. The surfaces are calculated using DFT method with 3-21G as basis set. All the molecular interactions were quantified and represented in a pie chart (**Fig.3.2.12**).

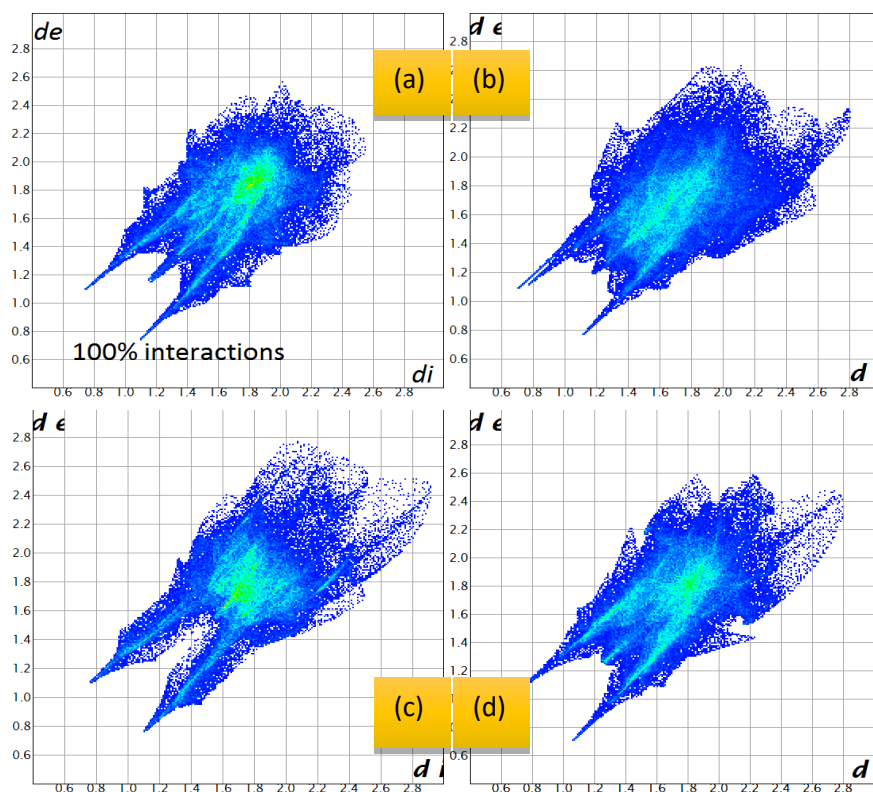


Fig.3.2.11. Fingerprint plots of (a) ABP (b) BPAP (c) DSP and (d) FDBP

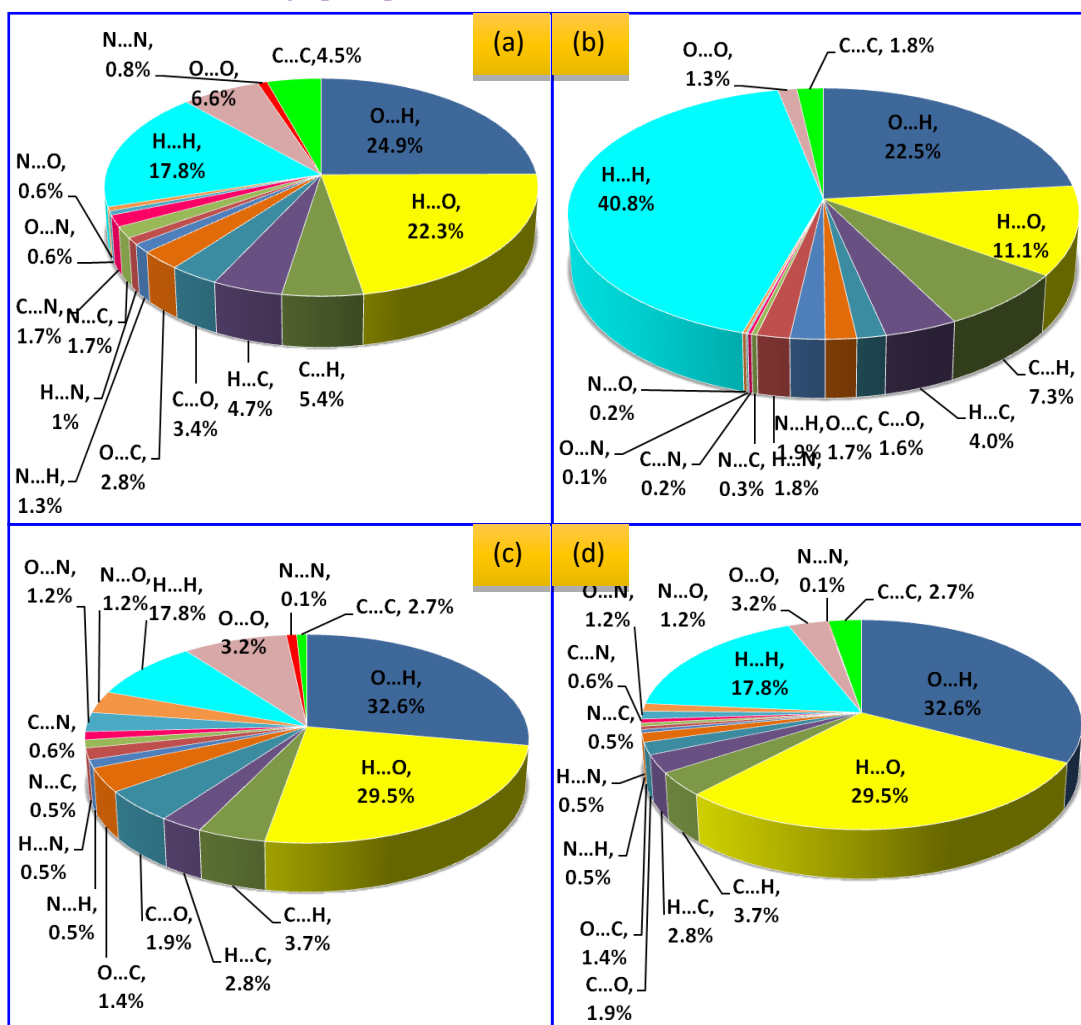


Fig.3.2.12. Pie chart representing all intermolecular interactions (a) ABP (b) BPAP (c) DSP and (d) FDBP

First-order molecular hyperpolarizability

Theoretical hyperpolarizability calculations were performed using the *GAUSSIAN09W* by DFT method, a program package on a personal computer without any constraints on the geometry using 3-21G as the basis with *GAUSSIAN VIEW* molecular visualization. The estimated first-order molecular hyperpolarizability (β) and dipole moment (μ) of all specimens are listed in **Table 3.2.2**. High β , due to nonzero μ values, is a required property of a nonlinear optical material. Extended π -conjugation and presence of structural groups like $-\text{CH}_3$ and $-\text{H}-\text{C}=\text{O}$ in the structure enhance the β value significantly as observed in the case of FDBP and DSP. This significant value of β and hence nonlinearity could not be translated at the macro level and negligible second harmonic generation efficiency is observed due to orientation effect resulting in a centrosymmetric structure. Large β clearly evidences that ABP, BPAP, DSP and FDBP are promising NLO materials at molecular level.

Table 3.2.2. The calculated β components and β_{tot} value (in esu) of picrates

	ABP	BPAP	DSP	FDBP
β_{xxx}	560.610	-16.713	-39.330	-463.490
β_{xxy}	161.650	-283.829	-220.330	-634.650
β_{xyy}	-338.670	-259.831	-723.680	-256.650
β_{yyy}	-56.520	-218.059	-1171.460	158.840
β_{xxz}	288.800	-519.065	-60.200	186.960
β_{xyz}	-9.280	-243.907	-545.600	-76.020
β_{yyz}	-100.920	-77.088	-1633.780	-308.110
β_{xzz}	150.360	24.646	-66.180	111.770
β_{yzz}	-4.050	155.749	-1137.360	-145.620
β_{zzz}	17.400	180.159	334.920	-549.890
$\beta_{tot} (\times 10^{-30})$	3.770	5.156	25.810	9.480

Conclusions

Novel supramolecular picrate crystals were synthesized and characterised. Crystal cohesion was achieved by N–H···O, C–H···O, N–H··· π and S–H···O intermolecular interactions. Hydrogen bonding controlled supramolecularity was studied by quantifying the molecular interactions. The interactions are estimated using Hirshfeld surface analysis and the hydrogen bonding interactions play a major role in crystal packing arrangement. All picrates possess high β values in comparison with standard urea and FDBP has a maximum value due to facile charge transfer atmosphere because of orientation. High β implies that ABP, BPAP, DSP and FDBP are promising NLO materials at molecular level.

References

- [1] M. Botoshansky, F. H. Herbstein and M. Kapon, *Acta Cryst.*, **B50** (1994), 589-596.
- [2] K. M. Priyadarshini, A. Chandramohan, T. Uma Devi., *J. Cryst. Process & Tech.*, **3** (2013), 123-129.
- [3] M. Obulichetty, D. Saravanabharathi, *Spectrochimica Acta Part A: Molecular and Biomolecular Spectroscopy*, **118** (2014), 861–866.
- [4] Valerio Bertolasi, Paola Gilli, and Gastone Gilli, *Crystal Growth & Design*, **11** (2011), 2724–2735
- [5] Kalle I. Nattinen and Kari Rissanen, *Crystal Growth & Design*, **3** (2003), 3.
- [6] F. L. Hirshfeld, *Theor. Chim. Acta.*, **44** (1977), 129.
- [7] M. A. Spackman, J. J. McKinnon, *CrystEngComm.*, **4** (2002), 378.
- [8] M. A. Spackman, D. Jayatilaka, *CrystEngComm.*, **11** (2009), 19-32.

CHAPTER-3.3

Supramolecular architecture of third-order nonlinear optical ammonium picrate crystals: DFT approach

Single crystals of ammonium picrate, having potential applications in optical devices, were grown from a mixed solvent system methanol-acetone (2:1, v/v) by slow evaporation technique at constant temperature. The structure is elucidated by single crystal X-ray diffraction analysis. Inter- and intramolecular hydrogen bonding interactions show supramolecular architecture in the crystal packing. The molecule is associated with accommodating weak C-H \cdots O, N-H \cdots O, C-H \cdots N, $\pi\cdots\pi$ and H \cdots H stacking interactions, very much responsible for the formation and strengthening of supramolecular assembly. Two different types of architecture, *i.e.*, a column like packing and cluster network type of infrastructure are observed. Fingerprint analysis was used to locate and quantify the molecular interactions. Third-order nonlinear optical properties of the grown crystal were derived by employing a single beam Z-scan technique at a wavelength of 532 nm with He-Ne laser system. Theoretical calculations were performed using density functional theory (DFT) method to derive the optimized geometry, dipole moment, polarizability, HOMO-LUMO energies at different levels, excited state energy, oscillator strength and Mulliken charge population. Estimated large first-order molecular hyperpolarizability of ~ 10 times of urea suggests a facile charge transfer atmosphere facilitating micro level nonlinearity. Idea about the size, shape, charge density distribution

and site of chemical reactivity of the molecule has been obtained by mapping electron density with electrostatic potential.

Introduction

Picric acid derivatives possess charge transfer, due to the presence of phenolic OH favouring the formation of salts with various organic bases. The hyperpolarizability can be enhanced by facile intramolecular charge transfer interaction, achieved by extending π -conjugated system. Proton transfer complexes are designed for the enhancement of first-order molecular hyperpolarizability (β) [1,2]. Our studies are mainly focused on the use of nitrogen-based hydrogen bond interaction assemblies such as amides [3]. The influence of hydrogen bonding will depend on whether it is inter- or intramolecular. For push-pull systems, the charge transfer from the donor to acceptor brings large variations in the molecular dipole moment and molecular polarizability. Hydrogen bonding interactions are one of the essential contacts in the process of molecular aggregation and designed to accumulate supramolecular architectures [4-6]. Intermolecular H-bonding leads to the close packing of molecules within the crystal medium, facilitate charge transfer leading to nonlinear optical properties. Recently, we have investigated some picrates for the development of charge transfer complexes [7-12]. In the present work, the synthesis, crystal growth, structure, spectral characterization, supramolecular architecture and the exhibited third-order nonlinear optical activity of ammonium picrate are analysed. Computational

studies were used to investigate density of states, HOMO-LUMO, excitation energies and molecular electrostatic potential.

Crystal Growth

Ammonium picrate (AP) was synthesized by mixing stoichiometric quantities of picric acid (Aldrich) and ammonium dihydrogen phosphate (Aldrich) in the molar ratio of 1:1. The reactants were dissolved in methanol-acetone (2:1, v/v) and thoroughly mixed using a magnetic stirrer for about 5 h. The solution was filtered and kept in constant temperature water bath. Single crystals were grown from various mixed solvent systems, water-acetic acid (2:1, v/v), methanol-acetone (1:1, v/v) and water-methanol (1:1, v/v) by slow evaporation growth technique at constant temperature (20 °C). Some tiny crystals appeared at the bottom of the container due to secondary nucleation. Photographs of as-grown crystals are displayed in **Fig.3.3.1**. All characterization studies were carried out using good quality crystals grown from methanol-acetone.



Fig 3.3.1. Photographs of as-grown crystals in various mixed solvent systems

(a) Water-acetic acid (b) Methanol-acetone (c) Water-methanol

Results and discussion

X-ray diffraction analysis

The structural analysis was carried out for the crystal grown from methanol-acetone and it crystallizes in the orthorhombic system with space group *Ibca*. The cell parameters are, $a = 7.13$ (3) Å, $b = 13.48$ (5) Å, $c = 19.78$ (8) Å, $\alpha = \beta = \gamma = 90^\circ$, and $V = 1904.07$ (13) Å³. No significant variation in cell parameter values are observed in the other mixed solvent systems used for crystallization. The solved structure is represented as three dimensional graphical images. **Fig.3.3.2a** displays the overlaid image of X-ray structure elucidated by single crystal XRD analysis and optimised structure derived by computational studies. The *ORTEP* with 50% probability is shown in **Fig.3.3.2b**. The packing projection is assembled like a regular network arrangement by C–H \cdots O interactions with distance of ~ 2.381 Å. Crystal packing arrangement along a-axis is displayed in **Fig.3.3.3**. The C–H bond lengths of the donor groups are significant, particularly for such short C–H \cdots O interactions. The N–H \cdots π interactions (2.696 Å) are weaker than C–H \cdots O hydrogen bonding interactions. Ammonium cation is interconnected between two picrate anions in a systematic ladder shaped aggregation. Intramolecular hydrogen bonding interactions are formed by N–H \cdots O with the interaction distance of ~ 1.86 Å and intermolecular N–H \cdots O interactions are modelled with an interaction distance of ~ 2.07 Å. Inter- and intramolecular hydrogen bonding interactions are displayed in **Fig.3.3.4**. Weak supramolecular interactions are modelled with $\pi\cdots\pi$ interactions, with an interaction distance of ~ 3.317 Å as shown in **Fig.3.3.5**.

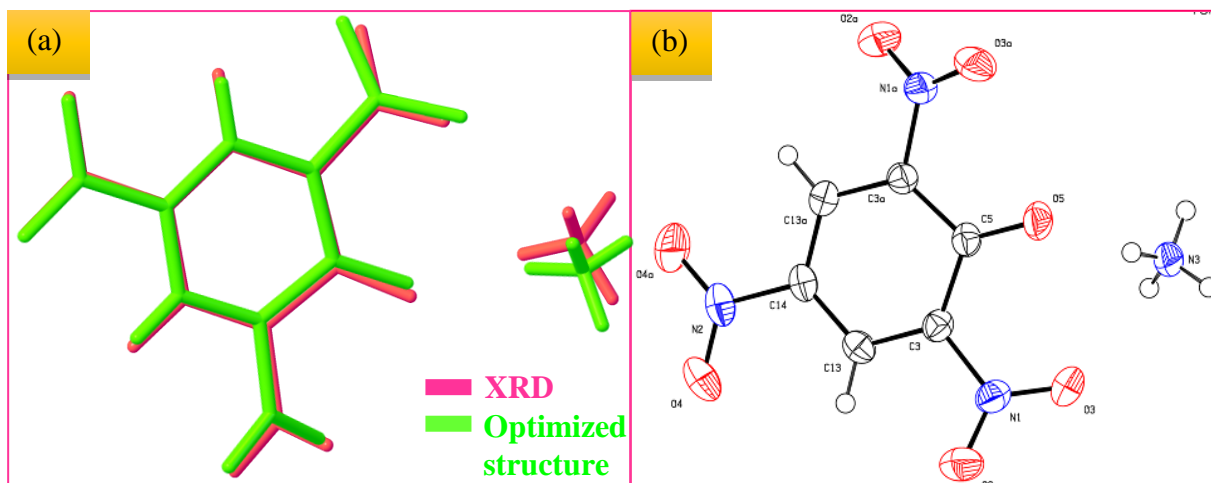


Fig.3.3.2 (a) Overlay of XRD structure and optimized structure
(b) ORTEP with 50% ellipsoid probability

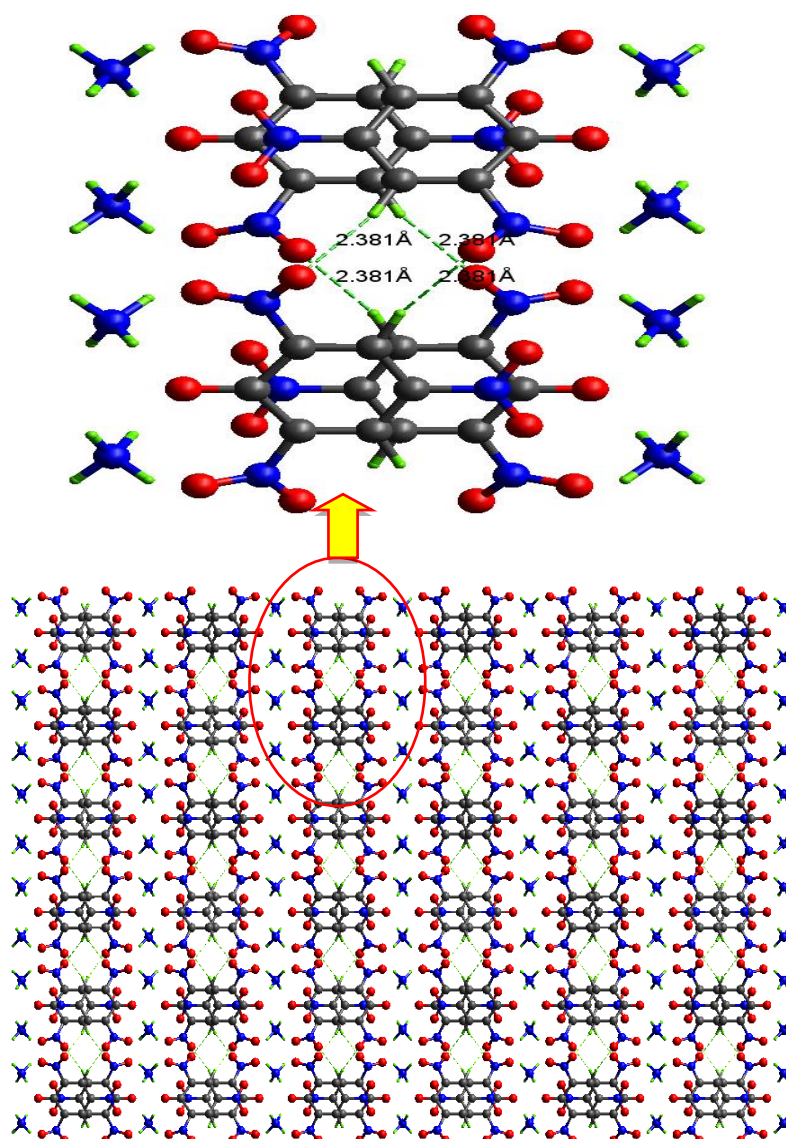


Fig.3.3.3 Packing projection of C-H...O interactions down along a-axis

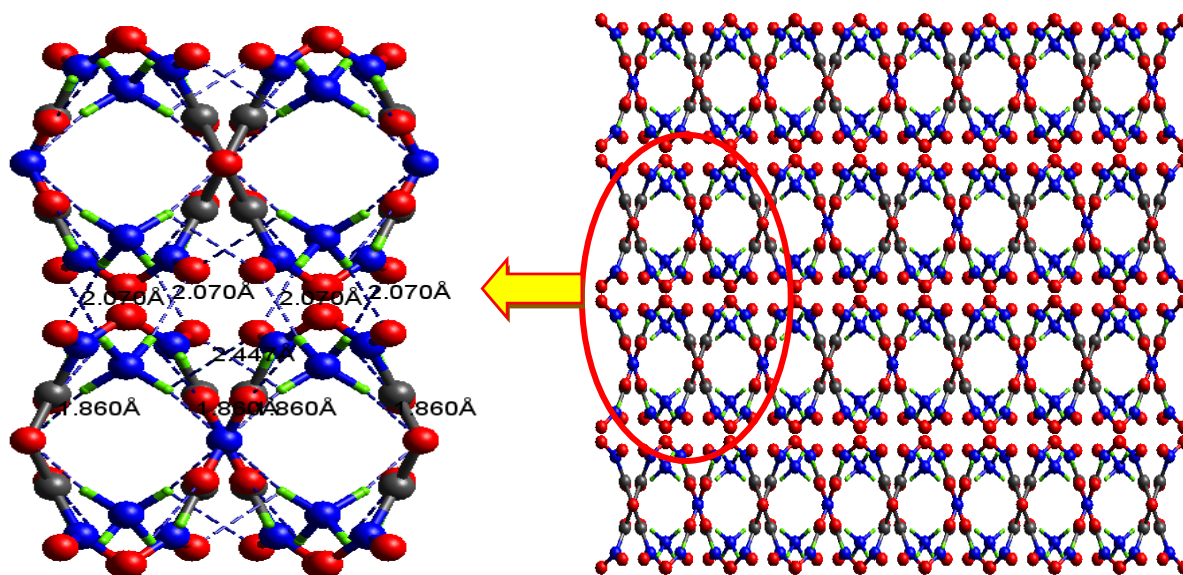


Fig.3.3.4 Packing projection of N-H...O interactions down along b-axis

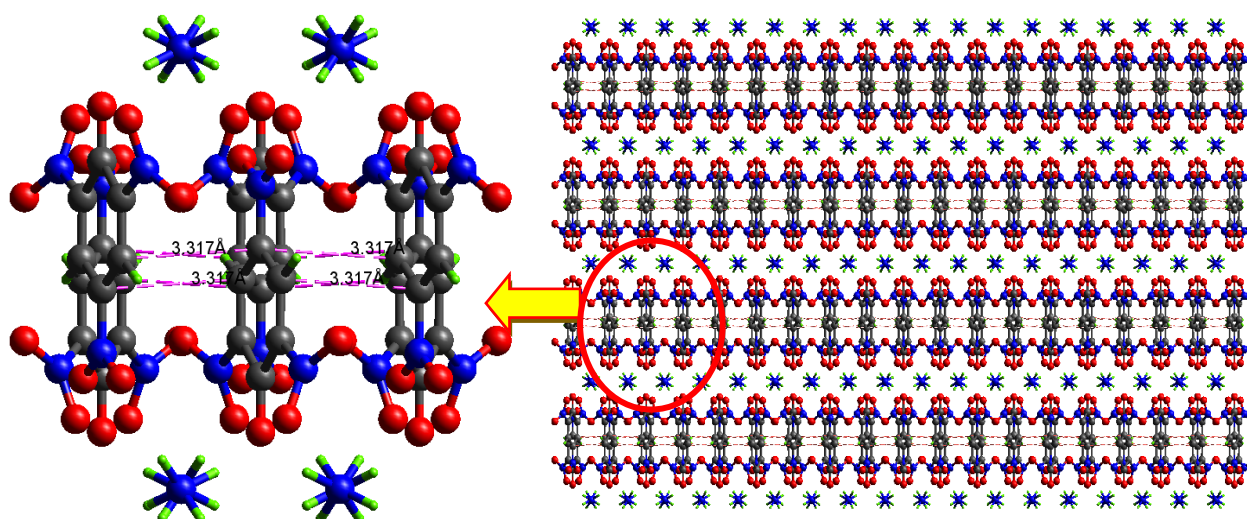


Fig.3.3.5 Packing projection of $\pi\cdots\pi$ interactions down along c-axis

In order to investigate the bulk formation behaviour of this supramolecular system, the X-ray powder diffraction patterns were recorded. Experimental peaks coincide with simulated patterns (**Fig.3.3.6**). Observed diffraction peaks were indexed. However, the relative intensities vary due to difference in the mosaic spread of powder and single crystal patterns.

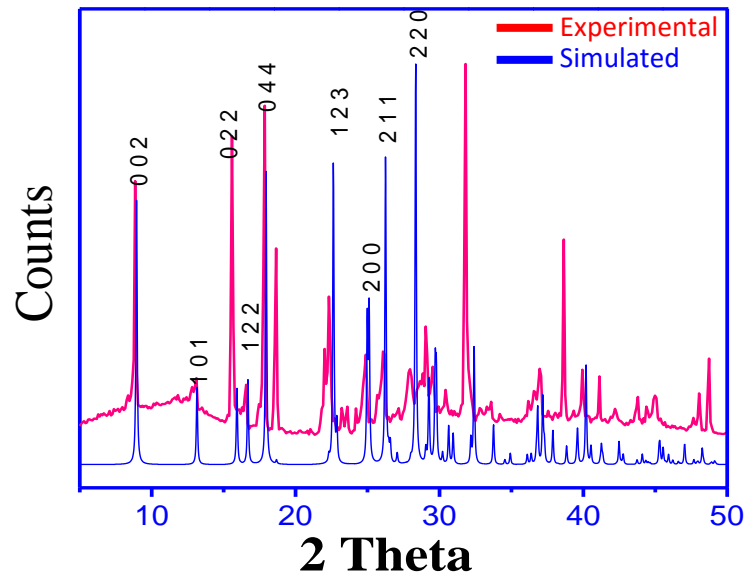


Fig.3.3.6. Experimental and simulated powder XRD patterns

Z-scan studies

The open aperture Z-scan transmittance is insensitive to the nonlinear refraction and effective for the nonlinear absorption while the closed aperture Z-scan transmittance is sensitive to determine both nonlinear absorption and nonlinear refraction [19]. Fig.3.3.7 displays the recorded closed and open aperture normalized transmittance curves of the given crystal. The pre-focal transmittance maximum (peak) followed by a post-focal transmittance minimum (valley) obtained from the closed aperture Z-scan method, indicates that the sign of the nonlinear refractive index is negative *i.e.* self-defocusing effect [20]. The self-defocusing effect explains the local variation of the nonlinear refractive index with temperature. In the open aperture, decrease in transmission near the focus is suggestive of the reverse saturated absorption (RSA), which evidences for the increase of nonlinear absorption coefficient of the crystal with an increase of light intensity. It is an essential parameter of crystal for optical limiting applications.

From the closed aperture, the difference between the peak and valley (ΔT_{p-v}) normalized transmission can be written in terms of the on-axis phase shift at the focal point

$$\Delta T_{p-v} = 0.406(1-S)^{0.25} |\Delta\Phi_0| \quad \text{Eqn. (3.3.1)}$$

where S is the linear transmittance aperture, calculated using the standard relation,

$$S = 1 - \exp\left(\frac{-2r_a^2}{\omega_a}\right) \quad \text{Eqn. (3.3.2)}$$

where r_a is denoting the radius of the aperture and ω_a is the beam radius at the aperture. The nonlinear refractive index (n_2) of the given crystal was estimated by using the following systematic relation [21],

$$n_2 = \frac{\Delta\Phi_0}{KI_0L_{\text{eff}}} \quad \text{Eqn. (3.3.3)}$$

where K is wave vector ($K= 2\pi/\lambda$) and I_0 is the intensity of the laser beam at the focal point ($I_0=26.50 \text{ MW/m}^2$). The effective thickness of the crystal (L_{eff}) can be estimated by the following equation,

$$L_{\text{eff}} = \frac{[1 - \exp(\alpha L)]}{\alpha} \quad \text{Eqn. (3.3.4)}$$

where α is the linear absorption coefficient and L denotes the thickness of the crystal. The nonlinear absorption coefficient (β) can be estimated from the open aperture using the standard relation [22],

$$\beta = \frac{2\sqrt{2}\Delta T}{I_0 L_{\text{eff}}} \quad \text{Eqn. (3.3.5)}$$

where ΔT is indicating one valley value at the open aperture Z-scan curve. The calculated values of n_2 and β can be used to calculate the real and imaginary part of the third-order nonlinear optical susceptibility and it is given by [23]

$$\text{Re } \chi^{(3)} (\text{esu}) = \frac{10^{-4} (\epsilon_0 C^2 n_0^2 n_2)}{\pi} \left(\frac{\text{cm}^2}{\text{W}} \right) \quad \text{Eqn. (3.3.6)}$$

$$\text{Im } \chi^{(3)} (\text{esu}) = \frac{10^{-2} (\epsilon_0 C^2 n_0 \lambda \beta)}{4\pi^2} \left(\frac{\text{cm}^2}{\text{W}} \right) \quad \text{Eqn. (3.3.7)}$$

where ϵ_0 is the permittivity of the free space, n_0 is the linear refractive index of the crystal and C is the velocity of light in vacuum. The absolute value of $\chi^{(3)}$ can be calculated by the following relation

$$|\chi^{(3)}| = \left[\left(\text{Re}(\chi^{(3)}) \right)^2 + \left(\text{Im}(\chi^{(3)}) \right)^2 \right]^{1/2} \quad \text{Eqn. (3.3.8)}$$

Table 3.3.1 lists the experimental results of the third-order nonlinear optical parameters of the given crystal. The material has a defocusing nature (negative refractive index), clearly confirming its suitability for applications such as protection of optical sensors and night vision devices [24]. The open aperture Z-scan curves reveal the reverse saturable absorption (RSA) due to large excited state absorption when compared to ground state absorption [25]. Thus, the grown crystal possesses excellent nonlinear optical properties and hence, it is a suitable candidate for nonlinear optical devices.

First-order molecular hyperpolarizability

Intermolecular interaction has important effects on electric hyperpolarizabilities which are related to the nonlinear optical (NLO) phenomena. Hydrogen bonding has a clear effect on increasing the hyperpolarizability, resulting in enhanced NLO activity because of facile charge transfer.

$$\beta_0 = (\beta_x^2 + \beta_y^2 + \beta_z^2)^{1/2} \quad \text{Eqn. (3.3.9)}$$

$$\beta_x = \beta_{xxx} + \beta_{xyy} + \beta_{xzz} \quad \text{Eqn. (3.3.10)}$$

$$\beta_y = \beta_{yyy} + \beta_{xxy} + \beta_{yzz} \quad \text{Eqn. (3.3.11)}$$

$$\beta_z = \beta_{zzz} + \beta_{xxz} + \beta_{yyz} \quad \text{Eqn. (3.3.12)}$$

The first-order molecular hyperpolarizability (β) values of some picrates are listed in **Table 3.3.2**. Hyperpolarizability value of AP is 3.66×10^{-30} esu (~ 10 times of urea) and dipole moment is estimated as 16.98 D. It is interesting to observe that the picrate possesses a larger β in comparison with standard urea as a consequence of proton transfer assisted facile charge transfer.

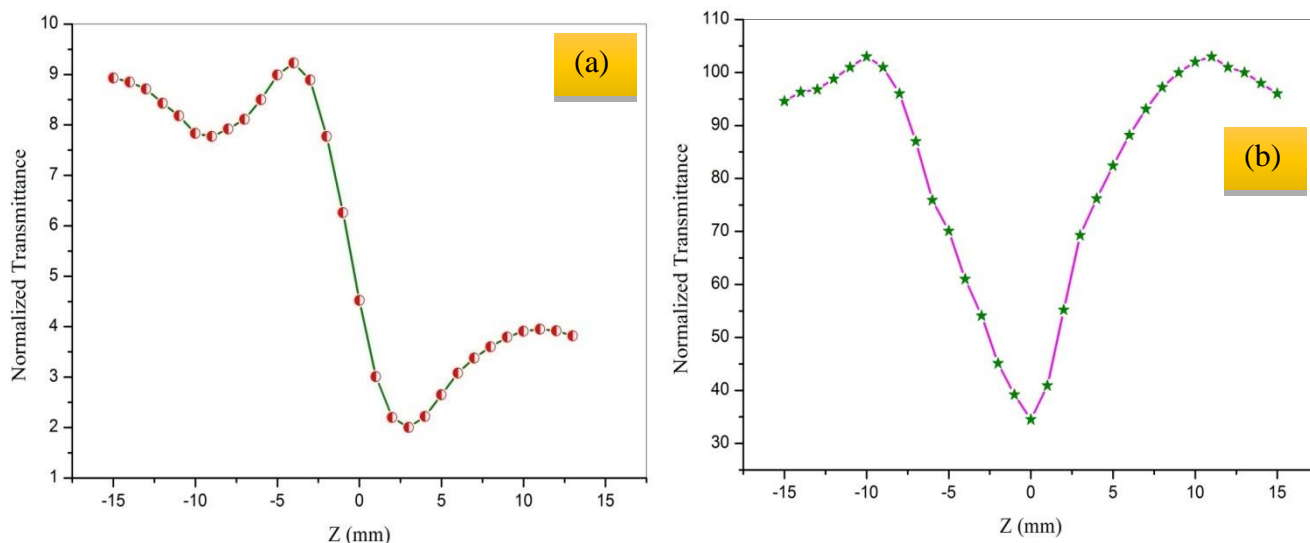


Fig .3.3.7 Z-scan curves

(a) Closed aperture (self-focusing) curve (b) Open aperture curve

Table 3.3.1. Third-order nonlinear optical parameters of AP

Laser beam wavelength (λ)	632.8 nm
Lens focal length (f)	30 mm
Aperture radius (r_a)	2 mm
Beam radius of the aperture (ω_a)	3.5 mm
Effective thickness of the sample (L_{eff})	1.485×10^{-3} m
Nonlinear refractive index (n_2)	5.408×10^{-11} m ² W ⁻¹
Nonlinear absorption coefficient (β)	2.498×10^{-3} mW ⁻¹
Third-order nonlinear optical susceptibility ($\chi^{(3)}$)	5.939×10^{-3} esu

Table 3.3.2. The calculated β components and β_{tot} value (in esu) of some picrates

	APP ^(a)	ABPP ^(b)	LASP ^(c)	LVP ^(d)	DCAP ^(e)	NP ^(f)	IP ^(g)	ONAP ^(h)	AP ⁽ⁱ⁾
β_{xxx}	1217.40	586.38	39.66	-3.61	981.65	681.33	-368.7	-10993.44	615.24
β_{xxy}	270.23	-422.92	0.012	-4.49	132.75	-1.92	-5.6	-6261.47	-455.97
β_{xyy}	-490.60	-490.60	-2.64	-5.31	-413.04	6.24	-6.02	-1073.23	-340.08
β_{yyy}	-83.43	-341.94	3.91	4.69	-242.29	-0.54	-1.68	2349.98	174.94
β_{xxz}	156.79	965.07	9.25	0.37	-140.12	-180.89	-612.26	6829.93	118.08
β_{xyz}	-243.90	289.46	-0.10	-1.31	-4.38	2.97	10.79	243.21	-23.45
β_{yyz}	-41.02	-30.76	-1.64	-1.17	10.21	2.59	6.88	-6157.94	6.14
β_{xzz}	94.33	146.37	0.54	-0.38	39.54	-270.36	-64.12	1043.03	-2.45
β_{yzz}	15.79	-57.75	1.87	-0.52	-18.96	8.59	48.67	11427.46	-12.44
β_{zzz}	15.35	64.31	-2.54	-0.35	-9.38	610.89	362.69	-18425.87	13.66
β_{tot} ($\times 10^{-30}$)	7.39	7.007	4.307	9.39	5.503	5.19	4.35	1.918	3.660

(a) 2-Aminopyridinium picrate (**15**)
(b) 4-Aminobenzophenonium picrate (**14**)
(c) L-Asparaginium picrate (**26**)
(d) L-Valinium picrate (**27**)
(e) 2,5-Dichloroanilinium picrate (**28**)
(f) Naphthalene picrate (**29**)
(g) Imidazolium picrate (**30**)
(h) Orthonitroaniline picrate (**31**)
(i) Ammonium picrate (**Present study**)

Hirshfeld surface and Fingerprint analysis

Hirshfeld surface (Fig.3.3.8) is represented by d_{norm} , d_e , d_i and curvedness [32]. It is a powerful tool [33, 34] for investigating intermolecular interactions existing in the crystal lattice. Fingerprint plots [35] are useful for quantifying molecular interactions present in the crystal packing. The bright red colour spots on the surface indicate the strong interactions (Fig.3.3.8a). The strong interactions are, O \cdots H (30.9%) and H \cdots O (25.4%), indicated as spikes in fingerprint plots. 2-Dimensional fingerprint plots were displayed in Fig.3.3.9. Other intermolecular interactions are quantified as O \cdots O (15.8%), H \cdots H (1.9%), O \cdots N (3.1%) and C \cdots H (3%). The C \cdots C (3.7%) interactions are represented at the middle part of the fingerprint plot. All the intra- and intermolecular interactions are quantified and displayed as a pie chart in Fig.3.3.10. Hydrogen bonding geometry is given in Table 3.3.3.

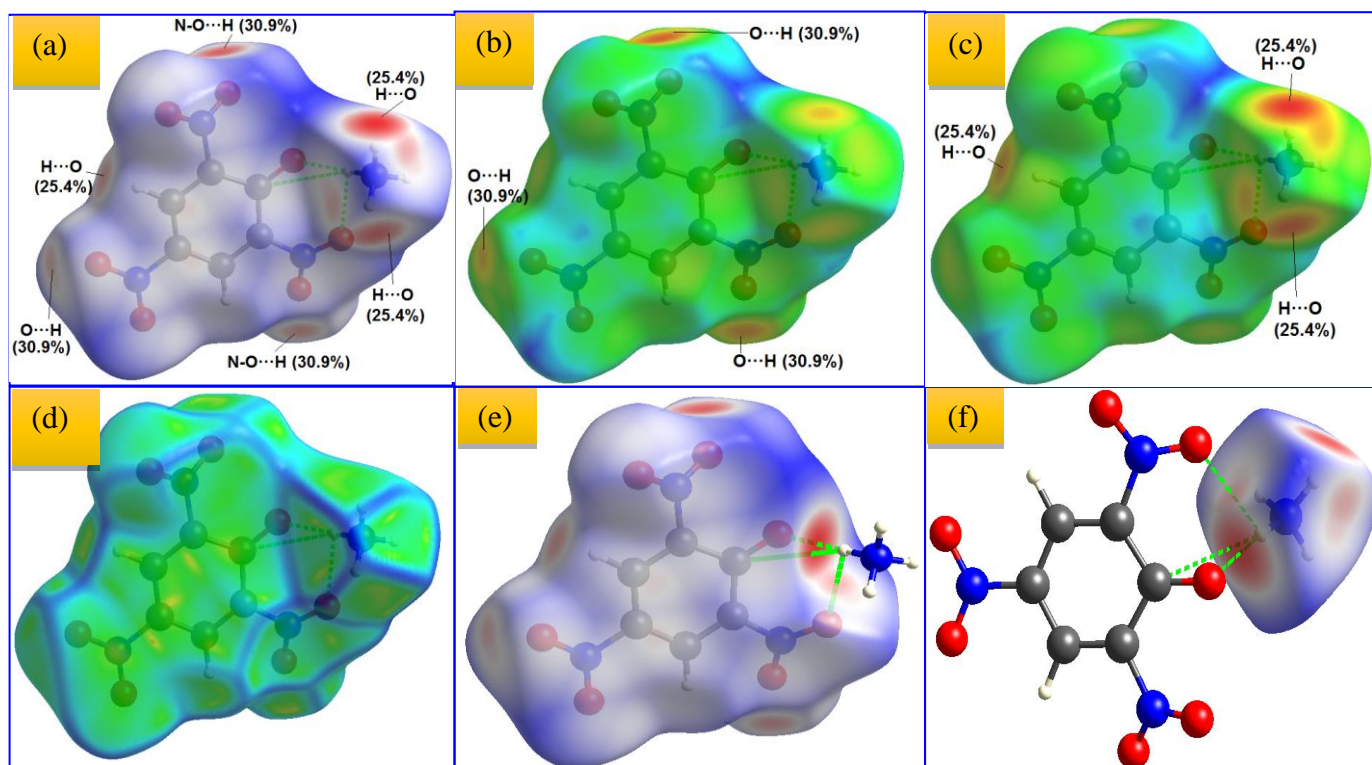


Fig.3.3.8. Hirshfeld surface plots (a) d_{norm} (b) d_e (c) d_i (d) curvedness (e) Red colour spots on Hirshfeld surface around picric acid indicating close contacts to ammonium cation (f) Red colour spots on Hirshfeld surface around ammonium cation indicating close contacts to picric acid anion

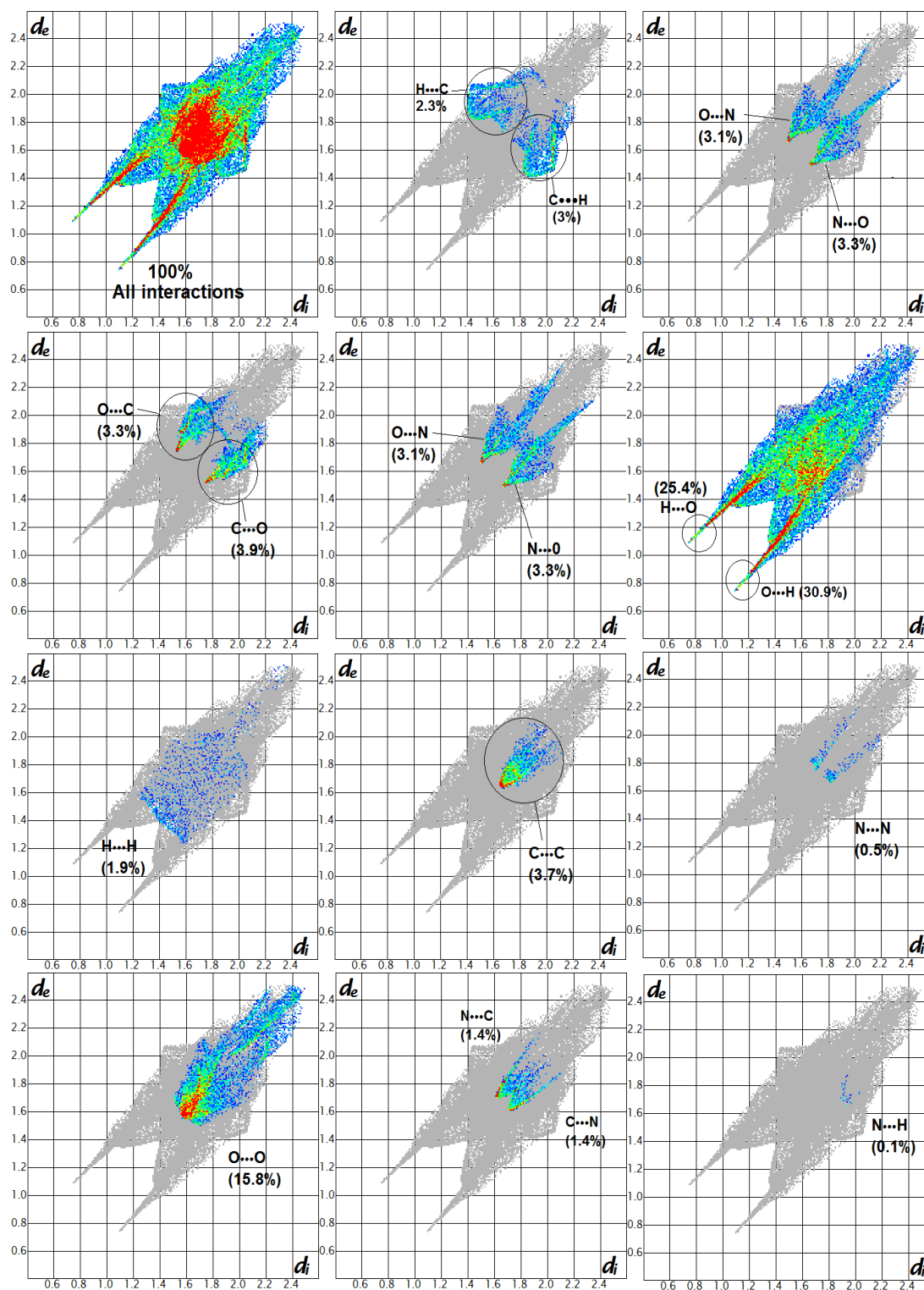


Fig.3.3.9. 2D Fingerprint plots

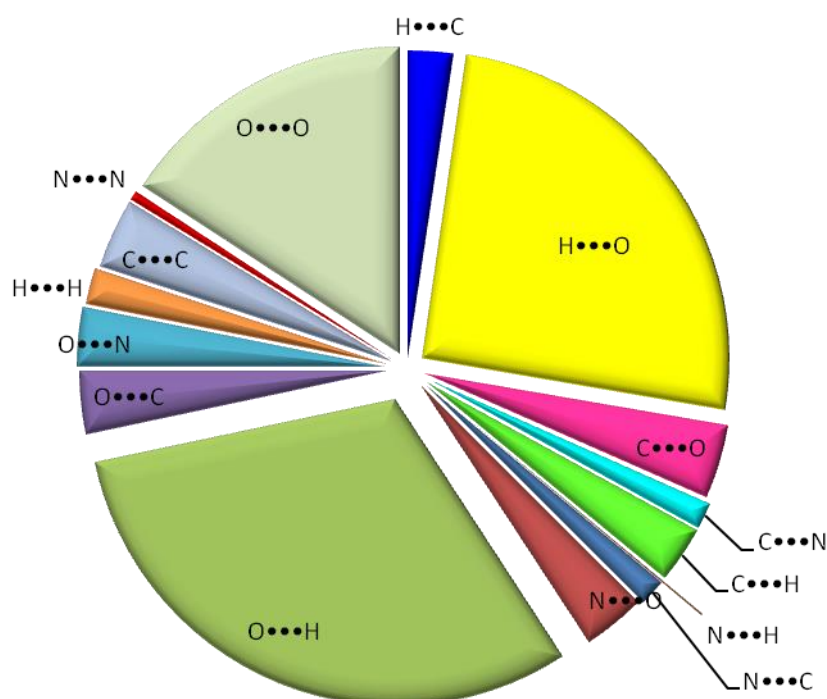


Fig.3.3.10. Pie chart representing the quantity of molecular interactions

Table 3.7.3 Hydrogen bonds geometry of AP (Å, °)

D-H...A	d(D-H)	d(H...A)	d(D...A)	<(DHA)
C(13)-H(13)···N(1)#2	0.920(2)	3.270(2)	4.151(17)	160.60(15)
C(13)-H(13)···O(2)#2	0.920(2)	2.530(2)	3.442(18)	173.90(16)
N(3)-H(3A)···O(5)	0.880(2)	1.980(2)	2.843(13)	168.00(19)
N(3)-H(3A)···O(3)	0.880(2)	2.490(2)	2.957(14)	114.40(15)
N(3)-H(3A)···N(1)	0.880(2)	3.320(2)	3.883(13)	124.80(15)
N(3)-H(3B)···O(3)#3	0.850(2)	2.240(2)	3.056(18)	160.30(19)
N(3)-H(3B)···N(1)#3	0.850(2)	3.020(2)	3.849(17)	164.00(17)
N(3)-H(3B)···O(2)#3	0.850(2)	3.110(2)	3.853(16)	147.20(17)
N(3)-H(3B)···O(4)#4	0.850(2)	2.510(2)	2.940(13)	111.90(16)

Symmetry transformations used to generate equivalent atoms:

#1 -x+1,-y+3/2,z **#2** x,-y+1,-z+3/2 **#3** -x+1,-y+1,-z+1

#4 -x+1,y,z-1/2

Thermal analysis

In order to estimate the thermal stability, the thermogravimetric analysis (TG) and differential thermal analysis (DTA) have been carried out (**Fig.3.3.11**). The studies reveal the purity of the material. No decomposition up to the melting point ensures the stability of the material. The sharp endotherm is indicative of solid state transition for relatively pure material. The melting point of crystal is $\sim 270^{\circ}\text{C}$ and decomposition started from $\sim 300^{\circ}\text{C}$.

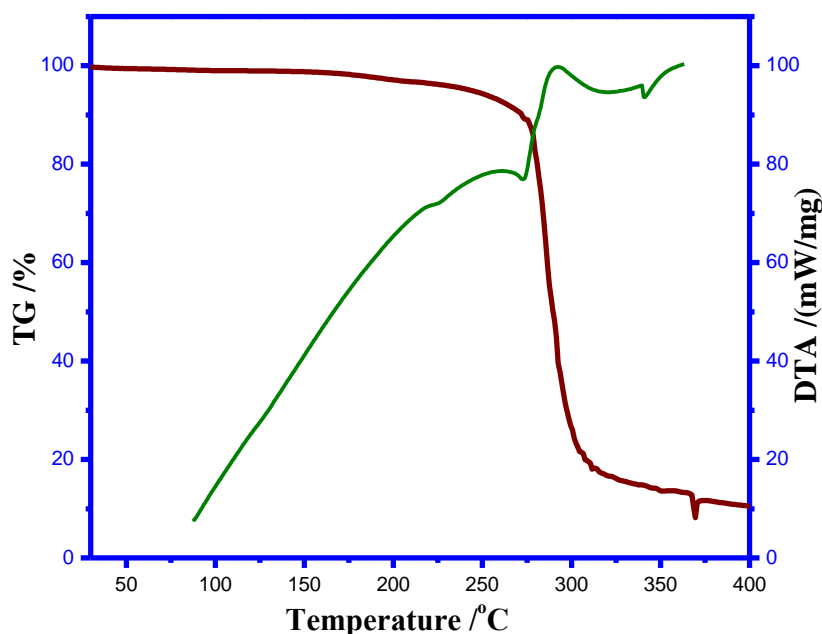


Fig.3.3.11. TG-DTA plot of AP

Computational studies

The structure parameters of the AP along with XRD data are listed in **Table 3.3.4**. As seen, slight variations in the bond lengths and angles are observed because the molecular states are different for experimental and computational processes. The difference between the

theoretical and experimental results has been computed by root mean square (RMSD) deviation using the following expression,

$$RMSD = \sqrt{\frac{1}{n-1} \sum_i^n (\gamma_i^{exp} - \gamma_i^{cal})^2} \quad Eqn. (3.3.13)$$

where n is the number of the experimental or calculated data. The RMSDs of bond length and angles are 0.0035 and 1.3 deviation respectively.

Table 3.3.4. Comparison of bond lengths and angles

Atoms	Experimental (XRD) Length/Å	Theoretical (DFT) Length/Å
O5-C5	1.250	1.240
O3-N1	1.220	1.206
C5-C3	1.449	1.438
N1-C3	1.460	1.440
N1-O2	1.224	1.191
C3-C13	1.376	1.381
C13-C14	1.382	1.374
N2-O4	1.215	1.195
N2-C14	1.451	1.439
Atoms	Angle/°	Angle/°
C5-C5-O5	124.05	122.05
C3-N1-O3	119.31	118.83
O2-N1-O3	122.93	122.74
N1-C3-C5	119.81	120.80
C3-C5-C5	124.38	123.09
C13-C3-N1	115.74	116.09
C14-C13-	118.63	119.91
C14-N2-O4	118.37	117.80
N2-C14-	118.97	119.74

The density of states spectrum is displayed in **Fig.3.3.12**. It is representing the excitation energies of occupied and virtual orbitals. The highest occupied molecular orbital (HOMO) and lowest unoccupied

molecular orbital (LUMO) at different energy levels are displayed in **Fig.3.3.13**. The frontier molecular orbitals have significant role in the chemical reactions, UV-Vis spectra, electrical and optical properties [36-38].

Red and green colours represent positive and negative lobes respectively. It is clear from **Fig.3.3.13** that HOMO is localized on benzene ring, C=C, N-O and LUMO are localized on C-O, C=N, while HOMO -1 is localized on phenol ring whereas LUMO +1 is localized almost on the whole molecule. The HOMO -2 is localized on the phenolic ring, C=O and LUMO +2 are localized almost on the ammonium and nitro groups. The calculated energy values of HOMO, -1, -2, levels are -5.8, -6.43 and -7.02 eV respectively and LUMO, +1, +2, levels are -1.93, -1.34 and -1.29 eV respectively. Also, the value of energy gap between the HOMO and LUMO is 3.87 eV. Small HOMO-LUMO gap means more polarizability and hence this picrate is a promising optically active material.

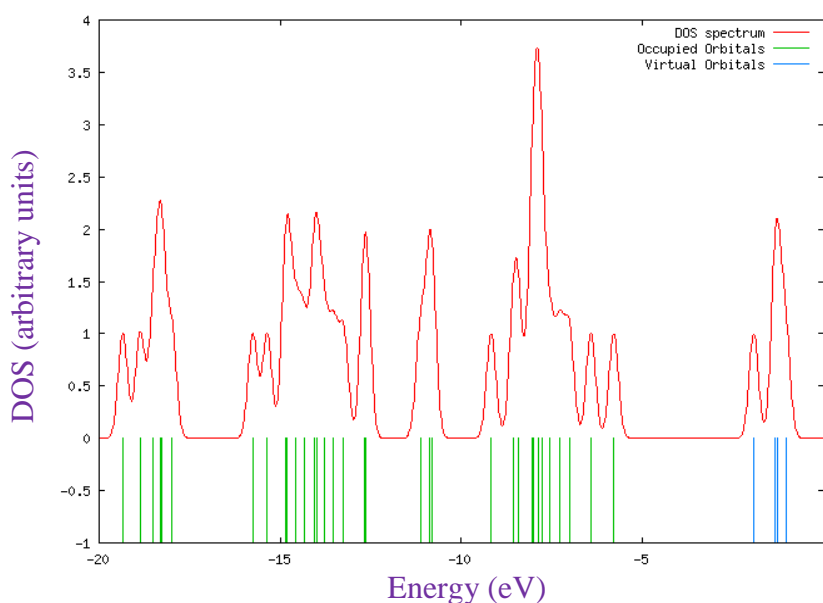


Fig.3.3.12. Density of States spectrum of AP

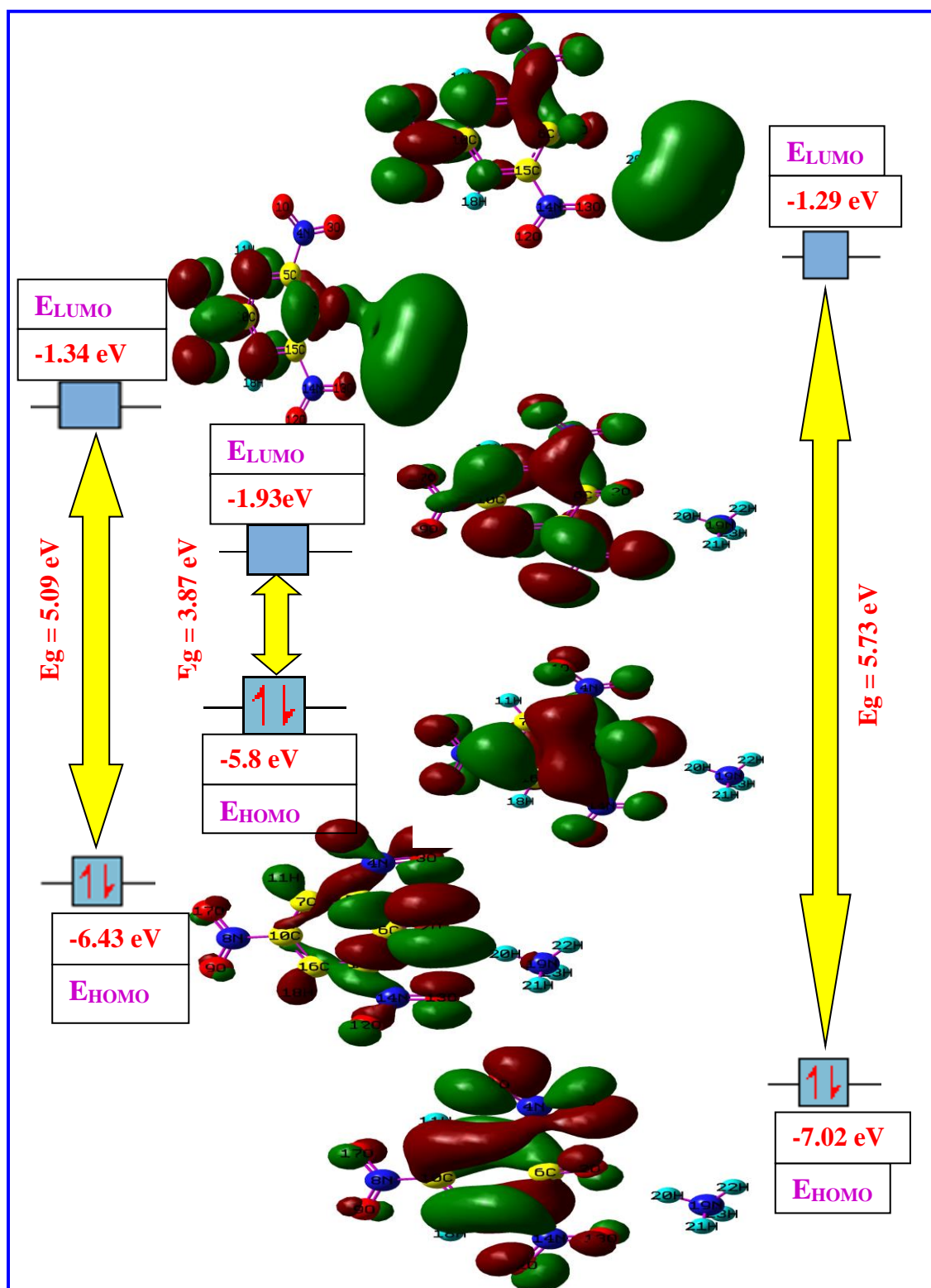


Fig.3.3.13 HOMO-LUMO energy gaps

The UV-vis excitation energies of experimental and computational studies are compared and displayed in **Fig.3.3.14**. The computational electronic excitation energies, absorption wavelengths and oscillator strengths were computed by the CIS-FC, TD-DFT (methanol), TD-DFT (gaseous state) and ZINDO methods using the *GAUSSIAN09W* program with basis set 6-31G. In ZINDO calculation, the excitation energy is high and it is about ~ 477.75 nm with less oscillator strength, $0.0796 f$. In TD-DFT method excitation energies are ~ 372.77 nm (gaseous state), ~ 345.9 nm (methanol) and oscillator strengths are $\sim 0.1208 f$, $\sim 0.1782 f$ respectively. In CIS-FC method excited energy is ~ 253.7 nm (gaseous state) and oscillator strength is $\sim 0.2801 f$. Comparatively CIS-FC method excited wavelength is less than the TD-DFT and ZINDO methods for the title compound. High oscillator strength is observed for CIS-FC method. Experimental excitation wavelength is 353.4 nm and TD-DFT (methanol) method well predicts a close value of 345.9 nm. Theoretical electronic absorption values are listed in **Table 3.3.5**.

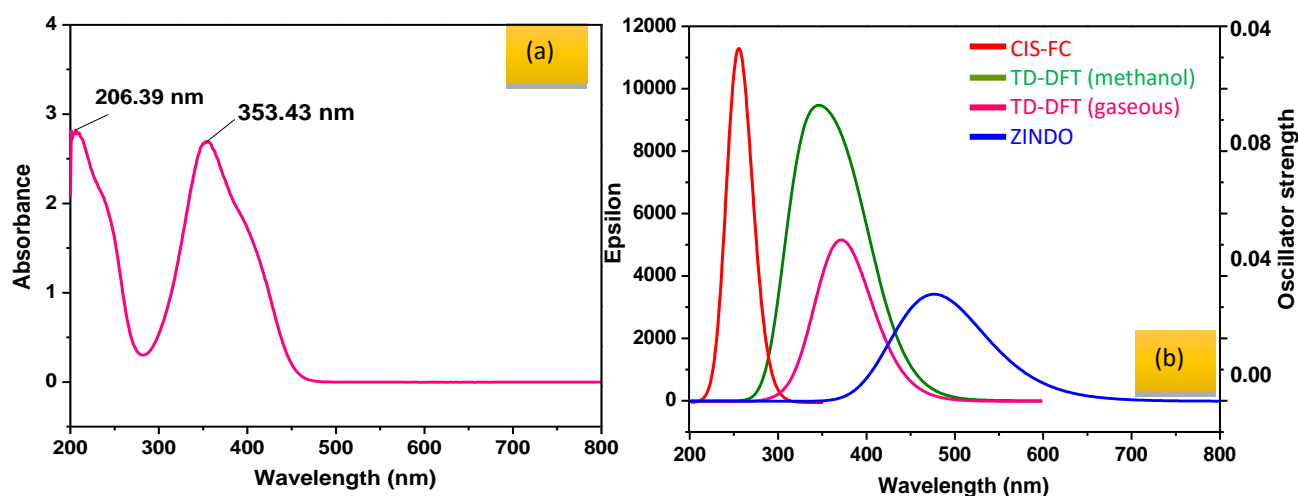


Fig.3.3.14 UV-visible spectra of AP (a) Experimental (b) Computational

Table 3.7.5. Theoretical electronic absorption spectral values of AP

Method	λ_{\max} (nm)	Excitation energies (eV)	Oscillator strengths (<i>f</i>)
CIS-FC	253.72	8.44	0.280
TD-DFT (methanol)	345.90	6.16	0.178
TD-DFT (gaseous)	372.77	5.80	0.120
ZINDO	477.75	8.24	0.079

Molecular electrostatic potential (MEP) represents surface around a molecule which gives information about the electrostatic effect responsible for total charge distribution of the molecule with dipole moment, electronegativity and chemical reactivity. It provides a visual method to understand the relative polarity of the molecule. An electron density isosurface mapped with electrostatic potential surface depicts the size, shape, charge density and site of chemical reactivity of the molecules. MEP and contour images are displayed in [Fig.3.3.15](#).

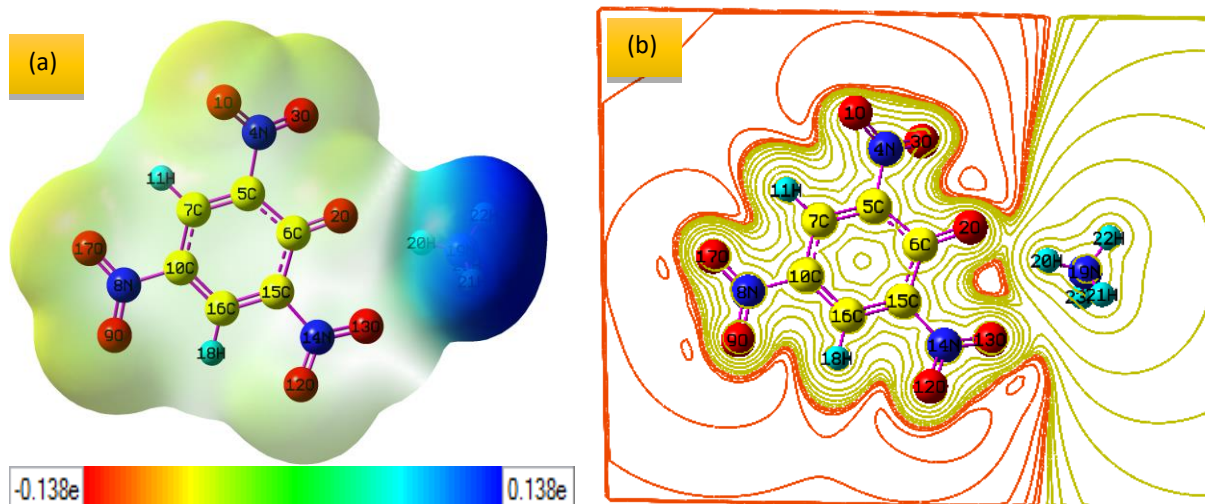


Fig.3.7.15 (a) Molecular electrostatic potential image (b) Counter map of MEP

Conclusions

Single crystals of ammonium picrate were grown, characterized and experimental observations are well supported by theoretical studies. The product formation was confirmed by FT-IR and single crystal XRD analysis. Comparison of bond lengths and angles of theoretical and experimental data shows slight variations. The crystal cohesion is achieved by inter- and intramolecular hydrogen bond interactions of C-H \cdots O, N-H \cdots O, C-H \cdots N, $\pi\cdots\pi$ and H \cdots H, responsible for charge transfer and they are visually evidenced. The third-order nonlinear absorption coefficient, nonlinear refractive index, and optical susceptibility by using the Z-scan technique indicate the suitability of the material for nonlinear optical devices. Hirshfeld surface and fingerprint analysis are used to quantify the hydrogen bonding interactions. TD-DFT (methanol) excitation energies are close to the experimental values. Further, a significantly higher value of first-order molecular hyperpolarizability in comparison with urea as standard indicates a promising nonlinear optical material. Efforts are on to sustain nonlinearity at the macro level by proper designing.

References

- [1] G. Anandha Babu, S. Sreedhar, S. Venugopal Rao, P. Ramasamy, *J. Cryst. Growth*, **312** (2010), 1957–1962.
- [2] V. Ramkumar, S. Anandhi, P. Kannan and R. Gopalakrishnan, *CrystEngComm.*, **15** (2013), 2438-2449.

- [3] Juan Saulo González-González, Francisco Javier Martínez-Martínez, Ana Lilia Peraza Campos, Maria de Jesus Rosales-Hoz, Efrén V. García-Báez and Itzia I. Padilla-Martínez, *CrystEngComm.*, **13** (2011), 4748-4761.
- [4] Shuo-ping Chen, Yu-qin Zhang, Le Hu, Hong-zhen He and Liang-jie Yuan, *CrystEngComm.*, **12** (2010), 3327-3336.
- [5] K. Thukral, N. Vijayan, B. Singh, I. Bdikin, D. Haranath, K. K. Maurya, J. Philip, H. Soumya, P. Sreekanth and G. Bhagavannarayana, *CrystEngComm.*, **16** (2014), 9245-9254.
- [6] A. Krishna, N. Vijayan, S. Gupta, K. Thukral, V. Jayaramakrishnan, B. Singh, J. Philip, S. Das, K. K. Maurya and G. Bhagavannarayana, *RSC Adv.*, **4** (2014), 56188-56199.
- [7] A. Aditya Prasad and S.P. Meenakshisundaram, *Cryst. Res. Technol.*, **50** (2015), 395-404.
- [8] A. Aditya Prasad, K. Muthu, M. Rajasekar, V. Meenatchi, S.P. Meenakshisundaram, *SpectrochimicaActa Part A: Molecular and Biomolecular Spectroscopy*, **135** (2015), 46-54.
- [9] A. Aditya Prasad, K. Muthu, M. Rajasekar, V. Meenatchi, S.P. Meenakshisundaram, *SpectrochimicaActa Part A: Molecular and Biomolecular Spectroscopy*, **135** (2015), 805-813.
- [10] K. Muthu, Subbiah Meenakshisundaram, *J. Cryst. Growth*, **352** (2012), 163-166.
- [11] K. Muthu, Subbiah Meenakshisundaram, *Mate. Lett.*, **84** (2012), 56-58.

- [12] A. Aditya Prasad, K. Muthu, V. Meenatchi, M. Rajasekar, S. P. Meenakshisundaram, SC. Mojumdar, *J. Therm. Anal. Calorim.*, **119** (2015), 885–890.
- [13] M. J. Frisch. *et al*, Gaussian 09 Revision-C.01, Gaussian, Inc., Wallingford, CT(2009).
- [14] Roy Dennington, Todd Keith and John Millam (2009) GaussView, Version **5**, Semichem Inc., Shawnee Mission KS.
- [15] D. Jayatilaka, D. J. Grimwood, A. Lee, A. Lemay, A. J. Russell, *et al*. (2006). TONTO-A, *system for computational chemistry*.
- [16] S. K. Wolff, D. J. Grimwood, J. J. McKinnon, D. Jayatilaka, M. A. Spackman, (2007). Crystal Explorer 2.1, University of Western Australia, Perth, Australia.
- [17] O. V. Dolomanov, L. J. Bourhis, R. J. Gildea, J. A. K. Howard, & H. Puschmann, *J. Appl. Cryst.*, **42** (2009), 339-341.
- [18] L. J. Bourhis, O. V. Dolomanov, R. J. Gildea, J. A. K. Howard, H. Puschmann, *Acta Cryst.*, **A71** (2015), 59-75.
- [19] M. Sheik-Bahae, A. A. Said, T. H. Wei, D. J. Hagan, E. W. Van Stryland, *J. Quant. Electron.*, **26** (1990), 760–769.
- [20] S. Shettigar, G. Umesh, K. Chandrasekaran, B. Kalluraya, *Synth. Met.*, **157** (2007), 142–146.
- [22] T. Kanagasekaran, P. Mythili, P. Srinivasan, A. Y. Nooraldeen, P. K. Palanisamy, R. Gopalakrishnan, *Cryst. Growth & Des.*, **8** (2008), 2335-2239.

- [23] M. Sheik-Bahae, A. A. Said, E. W. Van Stryland, *Opt. Lett.*, **14** (1989), 955–957.
- [24] P. Sathy, R. Philip, V. P. N. Nampoore, C. P. G. Vallaban, *J. Phys.*, **D27** (1994), 2019–2022.
- [25] Y. Z. Wei, S. Sridhar, *J. Chem. Phys.*, **99** (4) (1993), 3119.
- [26] F. Z. Henari, *J. Opt. A: Pure Appl. Opt.*, **3** (2001), 188.
- [27] N. Elleuch, W. Amamou, A. B. Ahmed, Y. Abid, H. Feki, *Spectrochimica Acta Part A: Molecular and Biomolecular Spectroscopy*, **128** (2014), 781–789.
- [28] Xiaojing Liu, Xijin Xu, Changwen Zhang, *Spectrochimica Acta Part A: Molecular and Biomolecular Spectroscopy*, **137** (2015), 378–382.
- [29] N. Sudharsana, S. Muthunatesan, G. Jasmine Priya, V. Krishnakumar, R. Nagalakshmi, *Spectrochimica Acta Part A: Molecular and Biomolecular Spectroscopy*, **121** (2014), 53–62.
- [30] M. Amalanathana, I. Hubert Joe, V. K. Rastogi, *Spectrochimica Acta Part A: Molecular and Biomolecular Spectroscopy*, **108** (2013), 256–267.
- [31] S. Anandhi, K. Mani Rahulan, T. S. Shyju, *Optik.*, **125** (2014), 7132–7135.
- [32] S. Anandhi, T. S. Shyju, R. Gopalakrishnan, *J. Cryst. Growth*, **312** (2010), 3292–3299.
- [33] M. A. Spackman and D. Jayatilaka, *CrystEngComm.*, **11** (2009), 19–32.
- [34] F. L. Hirshfeld, *Theor. Chim. Acta.*, **44** (1977), 129–138.

- [35] M. A. Spackman and J. J. McKinnon, *CrystEngComm.*, **4** (2002), 378–392.
- [36] J. J. McKinnon, M. A. Spackman, and A. S. Mitchell, *Acta Cryst.*, **B60** (2004), 627–668.
- [37] R. V. Solomon, P. Veerapandian, S. A. Vedha, P. Venuvanalingam, *J. Phys. Chem., A*, **116** (2012), 4667–4677.
- [38] P. Umadevi, L. Senthilkumar, M. Gayathri, P. Kolandaivel, *Spectrochimica Acta Part A: Molecular and Biomolecular Spectroscopy*, **132** (2014), 821–832.
- [39] C. Maria Ashok Kumar, S. Arulmozhi, J. Madhavan and M. Arul Thalpathi, *Archives of Applied Science Research*, **7 (5)** (2015), 69–72.

CHAPTER-3.4

Crystal growth, characterization and theoretical studies of 4-aminopyridinium picrate

Single crystals of 4-aminopyridinium picrate (APP) were grown by slow evaporation of a solution of mixed solvent system methanol-acetone (1:1, v/v) containing equimolar quantities of 4-aminopyridine and picric acid. Structure is elucidated by single crystal X-ray diffraction. The crystal belongs to the monoclinic system with four molecules in an unit cell (space group $P2_1/c$) and the cell parameters are, $a = 8.513 (\pm 0.015) \text{ \AA}$, $b = 11.33 (\pm 0.02) \text{ \AA}$, $c = 14.33 (\pm 0.03) \text{ \AA}$ and $\beta = 104.15^\circ (\pm 0.019)$, $V = 1340 (\pm 6) \text{ \AA}^3$ with refined R factors $R_1 = 0.0053$ and $wR_2 = 0.0126$. The electron density mapping is interpreted to find coordinates for each atom in the crystallized molecules. The functional groups present in the molecule are confirmed by FT-IR analysis. UV-visible spectral analysis was used to determine the band gap energy of picrate. Powder X-ray diffraction pattern reveals the crystallinity and it closely resembles the simulated one derived from the single crystal XRD data. Scanning electron microscopy reveals the surface morphology of the grown crystal. Optimized geometry is derived by Hartree - Fock calculations. The first-order molecular hyperpolarizability (β), bond lengths, bond angles and excited state energy from theoretical UV-vis spectrum were estimated.

Introduction

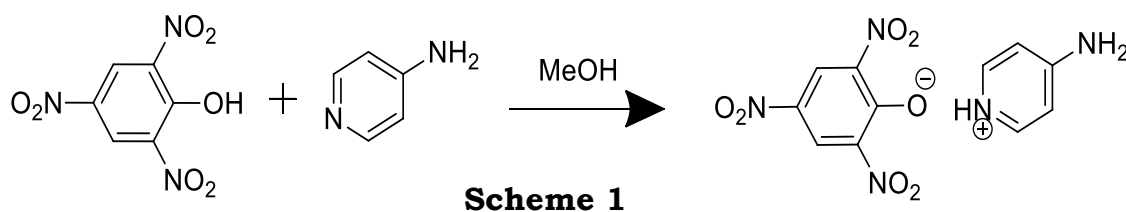
Despite numerous theoretical and experimental studies, several fundamental questions concerning the geometries of charge transfer
Published in *Spectrochimica Acta Part A: Molecular and Biomolecular Spectroscopy*, **135** (2015) 805–813.

complexes remain unanswered. In particular, little is known about the relative importance of classical van der Waals interactions and charge transfer forces in controlling the overall configuration and donor-acceptor contacts in charge-transfer interactions on the internal geometries. Pyridinium cations have been studied extensively [1-3] and particular attention has been given to the donor-acceptor properties. Several complexes of picric acid with organic molecules exhibit nonlinear optical applications [4]. During the past decade there has been considerable interest in the physical and structural properties of charge transfer complexes [5-8].

The crystal structure of 4-aminopyridinium picrate was reported earlier [9]. In the present work, we report the growth, characterization, electron density mapping and theoretical studies using Hartree – Fock and DFT methods.

Synthesis and growth

4-Aminopyridinium picrate was synthesized by mixing stoichiometric amounts of 4-aminopyridine (Sigma-Aldrich) and picric acid (Sigma-Aldrich) in an equimolar ratio using methanol as solvent (Scheme 1). The mixture was stirred at room temperature for 3 h and APP was obtained as yellow color precipitate. The product was purified by repeated recrystallization.



Recrystallized APP was dissolved in mixed solvent system (methanol:acetone, 1:1, v/v) and the solution warmed with constant stirring for an hour to avoid co-precipitation of multiple phases. Transparent crystals were grown by slow evaporation solution growth technique and the crystals were harvested after a period of 8-10 d. Photographs of as-grown APP crystals are shown in **Fig. 3.4.1**.



Fig.3.4.1 Photographs of as-grown APP

Results and discussion

FT-IR

Fourier transform infrared spectrum (FT-IR) was recorded using AVATAR 330 FT-IR spectrometer by KBr pellet technique in the spectral range of 400–4000 cm^{-1} . Experimental and theoretical FT-IR spectra are shown in **Fig. 3.4.2** as a comparative measure. The calculated wavenumbers all are positive and confirm the optimized structure of the title molecule as the most stable conformer. Some bands in theoretical IR spectra were not observed in the experimental one because the wavenumbers correspond to gaseous phase of isolated molecular state and this result in variations in wavenumbers.

NH₂ vibrations

The NH₂ asymmetric stretching vibrations give rise to a strong band in the region ~3365 cm⁻¹ and the symmetric NH₂ stretching was observed as a weak band at ~3235 cm⁻¹. The theoretically computed wavenumbers for the normal modes fall at ~3457, ~3456, ~3432, ~3415, ~3402 and ~3401 cm⁻¹ by DFT/B3LYP/6-31G (*d, p*) method. The lowering of NH₂ group stretching vibration wavenumbers is due to the intramolecular hydrogen bonding of nitro group of picrate to pyridinium amine as evidenced by the single crystal XRD.

C–O vibrations

The carbonyl stretching vibrations are observed in the region ~1648 cm⁻¹ with a strong intense peak and the theoretical values are predicted at ~1672 cm⁻¹. The C–O–C bending modes of vibrations are observed as weak bands at ~686 cm⁻¹ and theoretically computed vibration mode is predicted at ~663 cm⁻¹.

C=C and C–C vibrations

The ring stretching vibrations are very much important in the spectrum of benzene ring and its derivatives, highly characteristic of aromatic ring itself. The ring C=C and C–C stretching vibrations, known as semicircular stretching usually occurs in the region 1400-1625 cm⁻¹. The observed bands are observed at ~1648, ~1598, ~1269, ~988 and ~822 cm⁻¹. Theoretically computed vibrations are predicted at ~1672, ~1548, ~1254 and ~891 cm⁻¹. The C–C–C bending vibrations correspond to ~1189, ~1277, ~377, ~1189 and ~724 cm⁻¹. The C–C–C–C torsion mode of vibrational peaks

is predicted at ~ 965 , ~ 609 and ~ 540 cm^{-1} . Theoretical vibrational frequencies are slightly varied from the experimental frequencies.

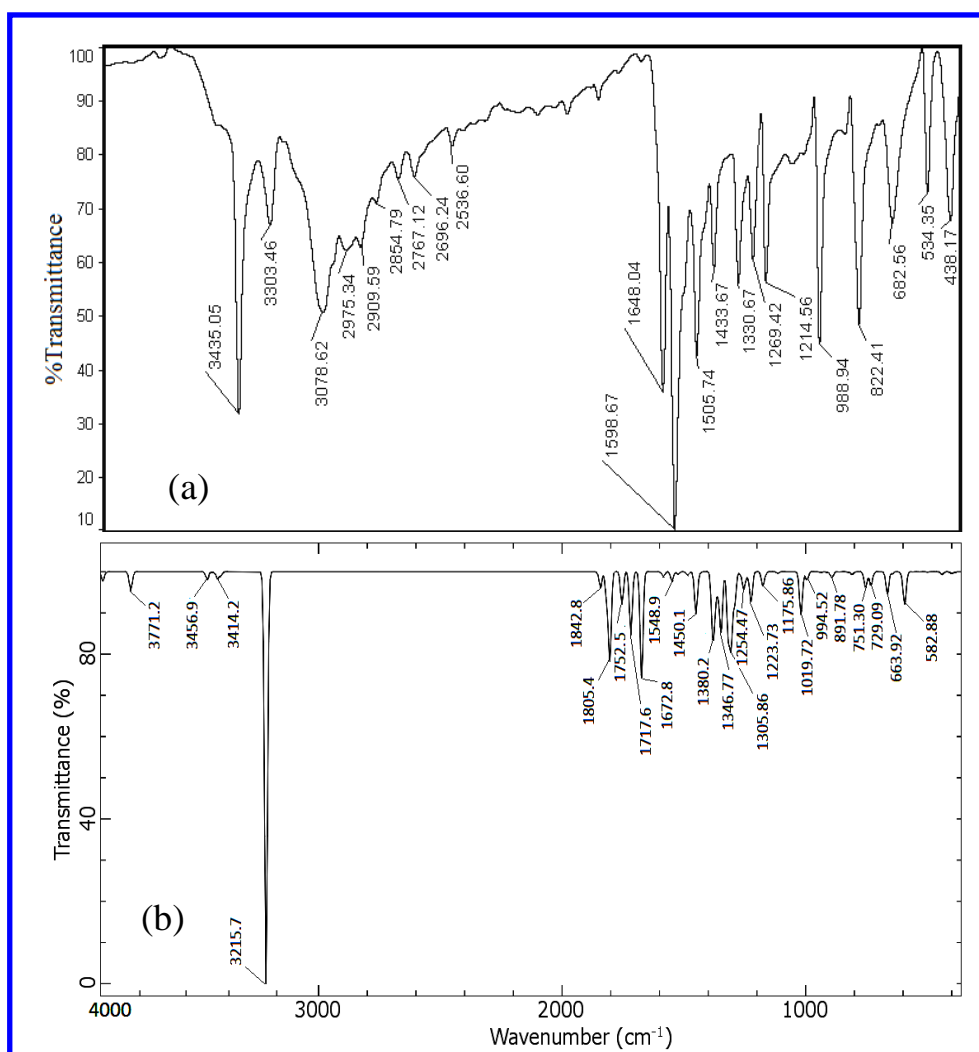


Fig.3.4.2 FT-IR spectra of APP (a) Experimental (b) Theoretical

O–N vibrations

A broad peak at ~ 1505 cm^{-1} corresponds to NO_2 asymmetric stretching. The sharp peak at ~ 822 cm^{-1} is attributed to NO_2 wagging. Theoretically assigned O–N stretching vibrations are observed at ~ 1672 , ~ 1450 , ~ 1330 and ~ 1433 cm^{-1} . The O–N–O bending vibrations are observed at ~ 988 , ~ 822 cm^{-1} and theoretically at ~ 994 , 891 cm^{-1} . The O–N–C bending modes of vibrations are observed at ~ 534 , ~ 438 cm^{-1} and theoretically at ~ 582 cm^{-1} .

The peaks are showing less intensity in the theoretical calculations because theoretical computations pertain to gaseous state and experimental spectra are recorded in solid state.

N-H vibrations

The very broad peak at $\sim 1598\text{ cm}^{-1}$ corresponds to NH asymmetric bending. Theoretically calculated H-N-C bending modes of vibrations are observed at $\sim 1548\text{ cm}^{-1}$. The H-N-H bending modes of vibrations are observed at ~ 1433 , ~ 1330 and $\sim 1269\text{ cm}^{-1}$ and theoretically predicted at ~ 1450 , ~ 1380 and $\sim 1254\text{ cm}^{-1}$.

UV-vis studies

The theoretical electronic excitation energies, absorption wavelengths and oscillator strengths were calculated by the CIS-FC, ZINDO and TD-DFT methods using *GAUSSIAN09W* [10] program with 6-31G (d, p) as basis set. Excitation energy from CIS-FC method is 266.9 nm. The theoretical absorption spectrum of APP obtained from CIS-FC method is shown in

Fig.3.4.3.

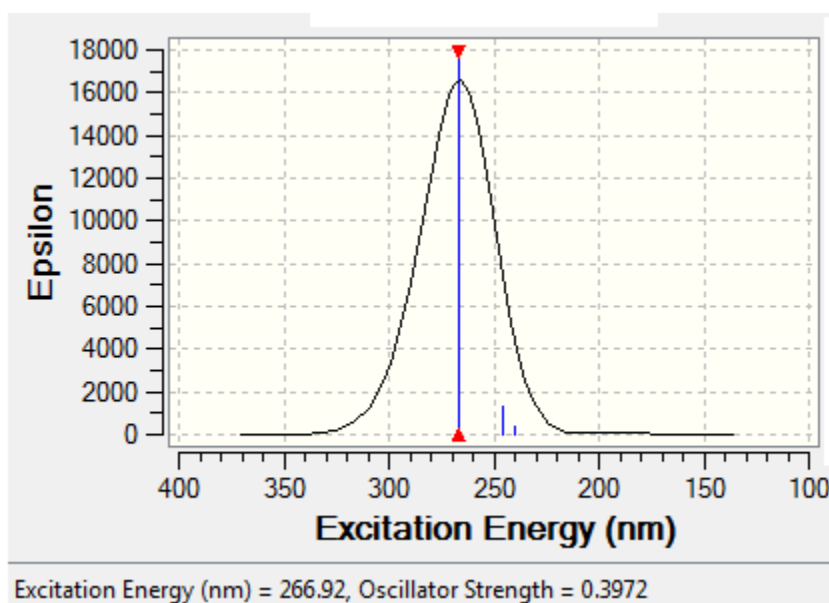


Fig.3.4.3 UV-vis spectrum of APP

The highest occupied molecular orbital (HOMO) and lowest unoccupied molecular orbital (LUMO) of APP are shown in **Fig.3.4.4**. The red and green colors represent the positive and negative values for the wave function. The energy gap between HOMO (-0.3114 a.u.) to LUMO (0.0634 a.u.) of the molecule is about 0.3749 a.u. The HOMO and LUMO energy gap explains the eventual charge transfer interactions taking place within the molecule.

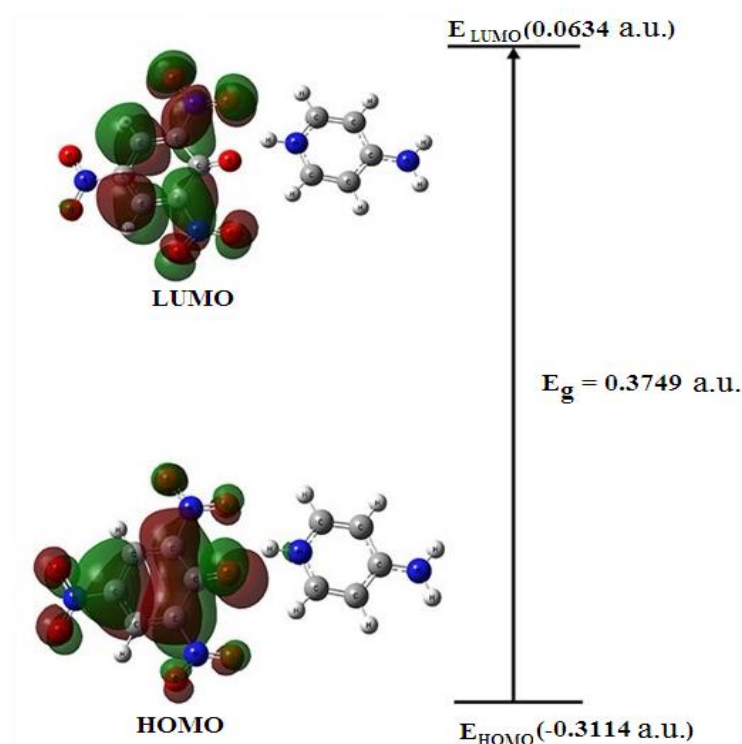


Fig.3.4.4 HOMO-LUMO energy gap

Mulliken [11] has derived the wave functions for the ground state and excited states of the complex and the charge distribution over the atoms thus provides a way of examining the proton transfer process. The proton transfer occurs from picric acid to pyridine. The charge distributions calculated by the Mulliken method [12] for the equilibrium geometry of APP is given in **Table 3.4.1**. The charge distribution on the molecule has an important influence on the vibrational spectra. Mulliken charge transfer is

differentiated by colour as shown in **Fig.3.4.5**. The direct and indirect band gap energies (**Fig.3.4.6**) of the specimen are calculated as 4.79 and 4.96 eV respectively from the Tauc plot by the application of Kubelka–Munk algorithm [13].

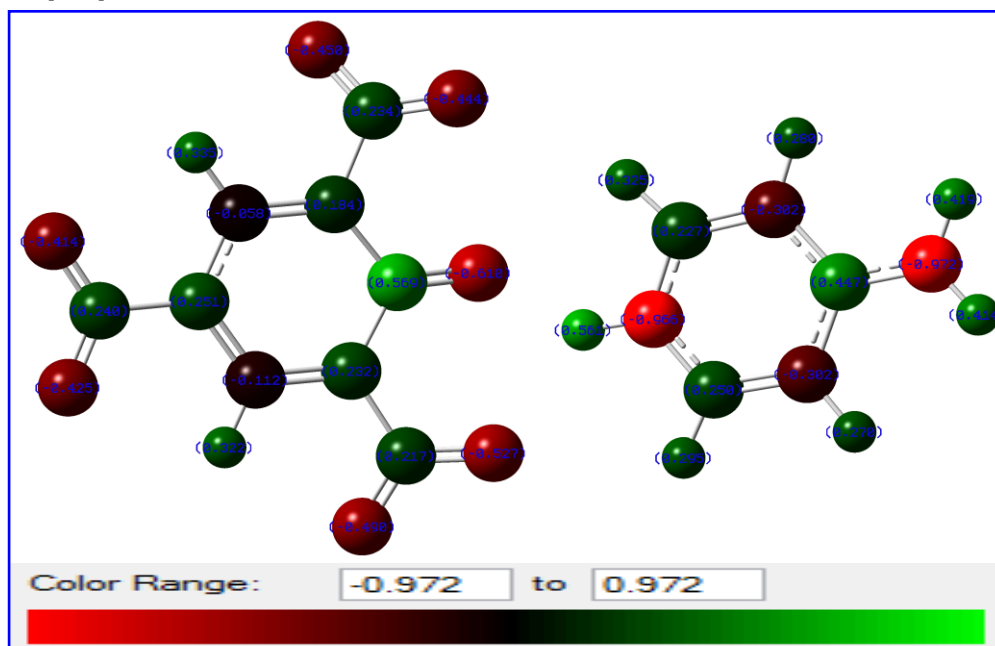


Fig.3.4.5 Mulliken charge transfer of APP indicated by colour

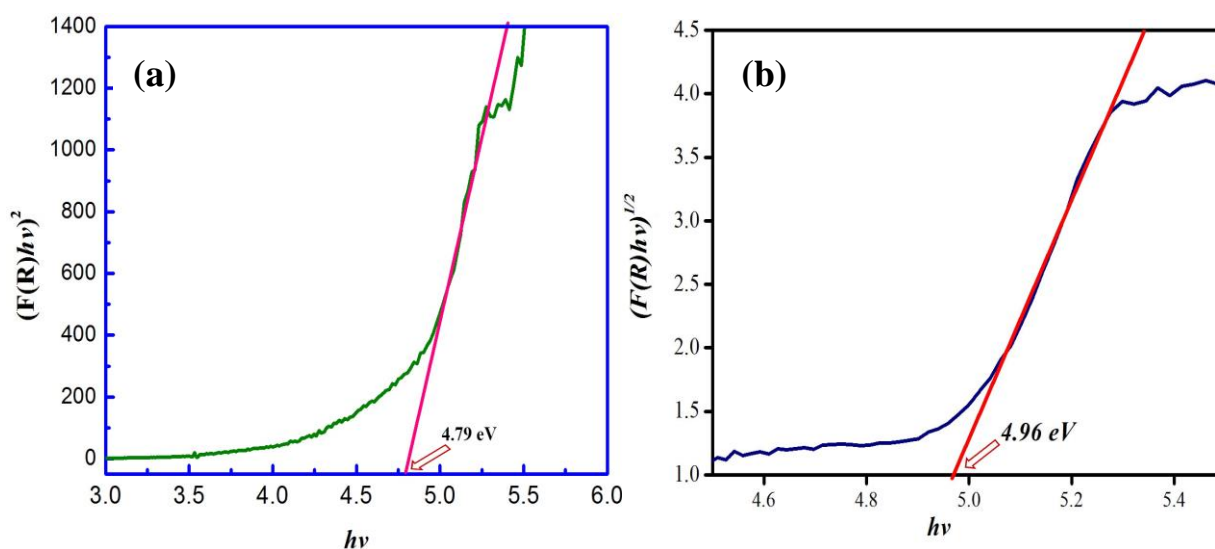


Fig.3.4.6 Tauc plots (a) Direct band gap energy (b) Indirect band gap energy

Table 3.4.1. Mulliken charge population of APP

Atom	Mulliken atomic charge/ e
1 O	-0.6087
2 O	-0.4549
3 O	-0.4593
4 O	-0.4204
5 O	-0.4191
6 O	-0.4729
7 O	-0.5192
8 C	0.5697
9 C	0.1868
10 C	-0.0653
11 C	0.2499
12 C	-0.1056
13 C	0.2265
14 N	0.2290
15 N	0.2405
16 N	0.2231
17 N	-0.9657
18 C	0.2279
19 C	-0.3044
20 C	0.4475
21 C	-0.3020
22 C	0.2521
23 N	-0.9737
24 H	0.3284
25 H	0.3265
26 H	0.5624
27 H	0.3226
28 H	0.2734
29 H	0.2738
30 H	0.3012
31 H	0.4147
32 H	0.4149

Scanning electron microscopy (SEM) analysis

SEM images of the APP are shown in **Fig.3.4.7**. Microscopic structure shows patches with rod like shapes confirming the roughness of the crystal.

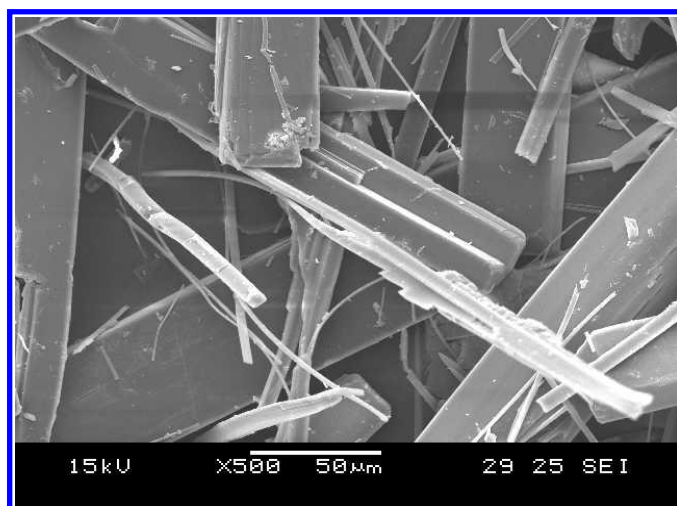


Fig.3.4.7 SEM photograph of APP

Single crystal XRD

APP crystallizes in the monoclinic system with space group $P2_1/c$ and the cell parameters are, $a = 8.51 (\pm 0.015) \text{ \AA}$, $b = 11.33 (\pm 0.02) \text{ \AA}$, $c = 14.33 (\pm 0.03) \text{ \AA}$, $\beta = 104.15^\circ (\pm 0.019)$ and $V = 1340 (\pm 6) \text{ \AA}^3$, in good agreement with reported values [14], derived using the *SHELXS97* program. In the present study the structure was solved with the *Olex2* [15] structure solution program using charge flipping [16] and refined with the *Olex2.Refine* refinement package using Gauss-Newton minimization. R_1 factor is very low with final $R_1 = 0.0053$ (number of reflections 2167). The solved structure is shown as three dimensional graphical images (**Fig.3.4.8**).

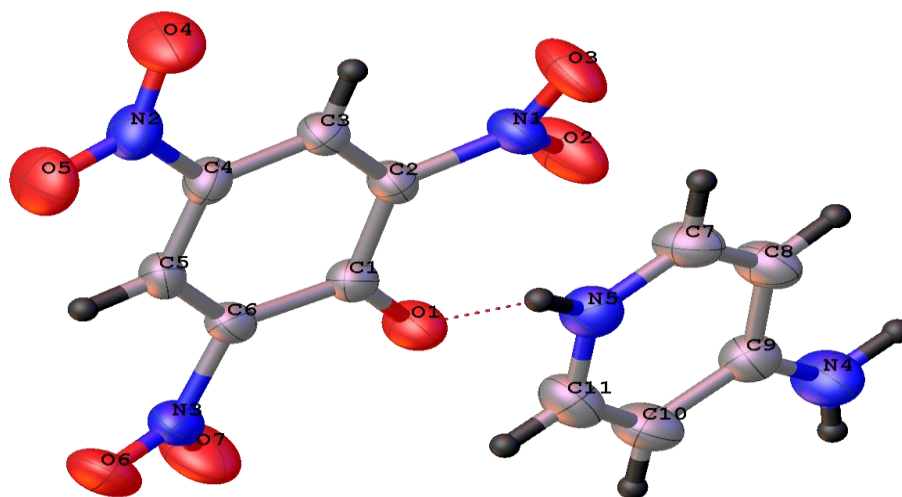


Fig.3.4.8 Molecular structure and numbering scheme of APP showing $O \cdots H - N$ interaction

Table 3.4.2. Experimental, theoretical bond lengths (Å) and angles (°) of APP.

Atom	Single crystal XRD	[HF, 6-31G (d, p)]
	Bond lengths (Å)	
O(1)-C(1)	1.236(5)	1.225
N(3)-O(7)	1.208(5)	1.204
N(3)-O(6)	1.217(5)	1.193
N(3)-C(6)	1.444(6)	1.441
O(3)-N(1)	1.226(6)	1.196
N(1)-O(2)	1.203(6)	1.196
N(1)-C(2)	1.453(6)	1.449
O(4)-N(2)	1.218(6)	1.197
N(5)-C(10)	1.329(7)	1.333
N(5)-C(9)	1.338(7)	1.335
N(5)-H(5A)	0.860	1.020
N(2)-O(5)	1.222(6)	1.197
N(2)-C(4)	1.436(6)	1.434
C(1)-C(6)	1.450(6)	1.448
C(1)-C(2)	1.452(6)	1.449
C(5)-C(6)	1.368(6)	1.373
C(5)-C(4)	1.379(6)	1.382
C(5)-H(5)	0.930	1.070
C(2)-C(3)	1.356(7)	1.362
C(4)-C(3)	1.379(7)	1.393
C(3)-H(3)	0.930	1.070
C(7)-N(4)	1.321(7)	1.339
C(7)-C(8)	1.402(7)	1.408
C(7)-C(11)	1.403(7)	1.411
N(4)-H(4A)	0.860	0.992
N(4)-H(4B)	0.860	0.992
C(9)-C(8)	1.344(7)	1.362
C(9)-H(9)	0.930	1.073
C(8)-H(8)	0.930	1.073
C(11)-C(10)	1.353(8)	1.361
C(11)-H(11)	0.930	1.073
C(10)-H(10)	0.930	1.072
	Bond angles (°)	
O(7)-N(3)-O(6)	120.97(4)	122.74
O(7)-N(3)-C(6)	120.46(4)	118.98
O(6)-N(3)-C(6)	118.57(4)	118.24
O(2)-N(1)-O(3)	122.49(4)	123.79
O(2)-N(1)-C(2)	119.83(4)	118.59
O(3)-N(1)-C(2)	117.65(4)	117.55
C(10)-N(5)-C(9)	120.13(5)	121.71
C(10)-N(5)-H(5A)	119.90	121.66
C(9)-N(5)-H(5A)	119.90	116.61
O(4)-N(2)-O(5)	122.85(5)	124.25
O(4)-N(2)-C(4)	118.58(4)	117.80
O(5)-N(2)-C(4)	118.57(4)	117.93
O(1)-C(1)-C(6)	125.31(4)	124.54
O(1)-C(1)-C(2)	123.54(4)	122.88
C(6)-C(1)-C(2)	111.09(4)	112.48
C(6)-C(5)-C(4)	119.03(4)	119.85
C(6)-C(5)-H(5)	120.50	120.04
C(4)-C(5)-H(5)	120.50	120.09

C(3)-C(2)-C(1)	124.51(4)	123.88
C(3)-C(2)-N(1)	115.80(4)	116.88
C(1)-C(2)-N(1)	119.68(4)	119.23
C(5)-C(6)-N(3)	115.71(4)	116.59
C(5)-C(6)-C(1)	124.66(4)	123.36
N(3)-C(6)-C(1)	119.59(4)	120.03
C(5)-C(4)-C(3)	121.00(4)	120.52
C(5)-C(4)-N(2)	119.73(4)	119.74
C(3)-C(4)-N(2)	119.24(4)	119.71
C(2)-C(3)-C(4)	119.67(4)	119.56
C(2)-C(3)-H(3)	120.20	120.21
C(4)-C(3)-H(3)	120.20	120.22
N(4)-C(7)-C(8)	120.65(5)	121.02
N(4)-C(7)-C(11)	122.46(5)	120.87
C(8)-C(7)-C(11)	116.88(5)	118.10
C(7)-N(4)-H(4A)	120.00	121.06
C(7)-N(4)-H(4B)	120.00	121.19
H(4A)-N(4)-H(4B)	120.00	117.72
N(5)-C(9)-C(8)	121.24(5)	120.90
N(5)-C(9)-H(9)	119.40	115.22
C(8)-C(9)-H(9)	119.40	123.86
C(9)-C(8)-C(7)	120.35(5)	119.15
C(9)-C(8)-H(8)	119.80	119.92
C(7)-C(8)-H(8)	119.80	120.91
C(10)-C(11)-C(7)	119.42(5)	119.07
C(10)-C(11)-H(11)	120.30	120.04
C(7)-C(11)-H(11)	120.30	120.87
N(5)-C(10)-C(11)	121.98(5)	121.04
N(5)-C(10)-H(10)	119.00	115.87
C(11)-C(10)-H(10)	119.00	123.08

Slight variations in the bond lengths and angles of theoretical and experimental values are observed (**Table 3.4.2**). A three-dimensional view of the electron density in crystal structure is determined from X-ray diffraction experiments. X-rays scatter from the electron clouds of atoms in the crystal lattice. The diffracted waves from scattering planes h,k,l are described by structure factors. The electron density as a function of position x,y,z is the Fourier transform of the structure factors.

$$\rho(xyz) = 1/V \sum_{hkl} F(hkl) \exp[-2\pi i(hx + ky + lz)] \quad \text{Eqn. (3.4.1)}$$

The intensity of these reflections is measured for determining the distribution of electrons in the crystal. The result is a map of the crystal that

shows the distribution of electrons at each point which may then be interpreted to find coordinates for each atom in the crystallized molecules. Electron density mapping is generated by using *ShelXle* [17]. Electron density mapping of F(obs) and Fo-Fc is shown in **Fig.3.4.9** and 2132 reflections are used for refinement. An electron density map $\rho(x, y, z)$, describes the intensity of the electron density at each point in real space. This reflects the fact that regions in space with a higher electron density will scatter more X-rays, although this is not what is measured directly. Once the mean and the standard deviation (σ) of the intensity across the entire map are calculated, the intensity of every point in $\rho(x, y, z)$ can be described in standard deviation (σ) units away from the mean.

$$\mathbf{R} = \frac{\sum [\mathbf{F}(\text{obs}) - \mathbf{F}(\text{calc})]}{\sum [\mathbf{F}(\text{obs})]} \quad \text{Eqn. (3.4.2)}$$

Fo-Fc Map = 0.04 eÅ⁻³ (σ = 0.014)

Fo Map = 1.3 eÅ⁻³ (σ = 1.1)

From the electron density mapping one can observe that there is no structural disorder in the solved structure so that R factor is very low (0.005) compared to the reported value (**18**). In the crystal, the cations and anions are linked *via* N—H···O hydrogen bonds involving the phenolate O atom and the nitrogen atom in the pyridinium ring. The ionic pairs are linked into a ribbon-like structure along by C—H···O hydrogen bonds. This is due to the aggregation of the donor-acceptor molecules, contributing to the bulk susceptibility from intermolecular hydrogen bonding.

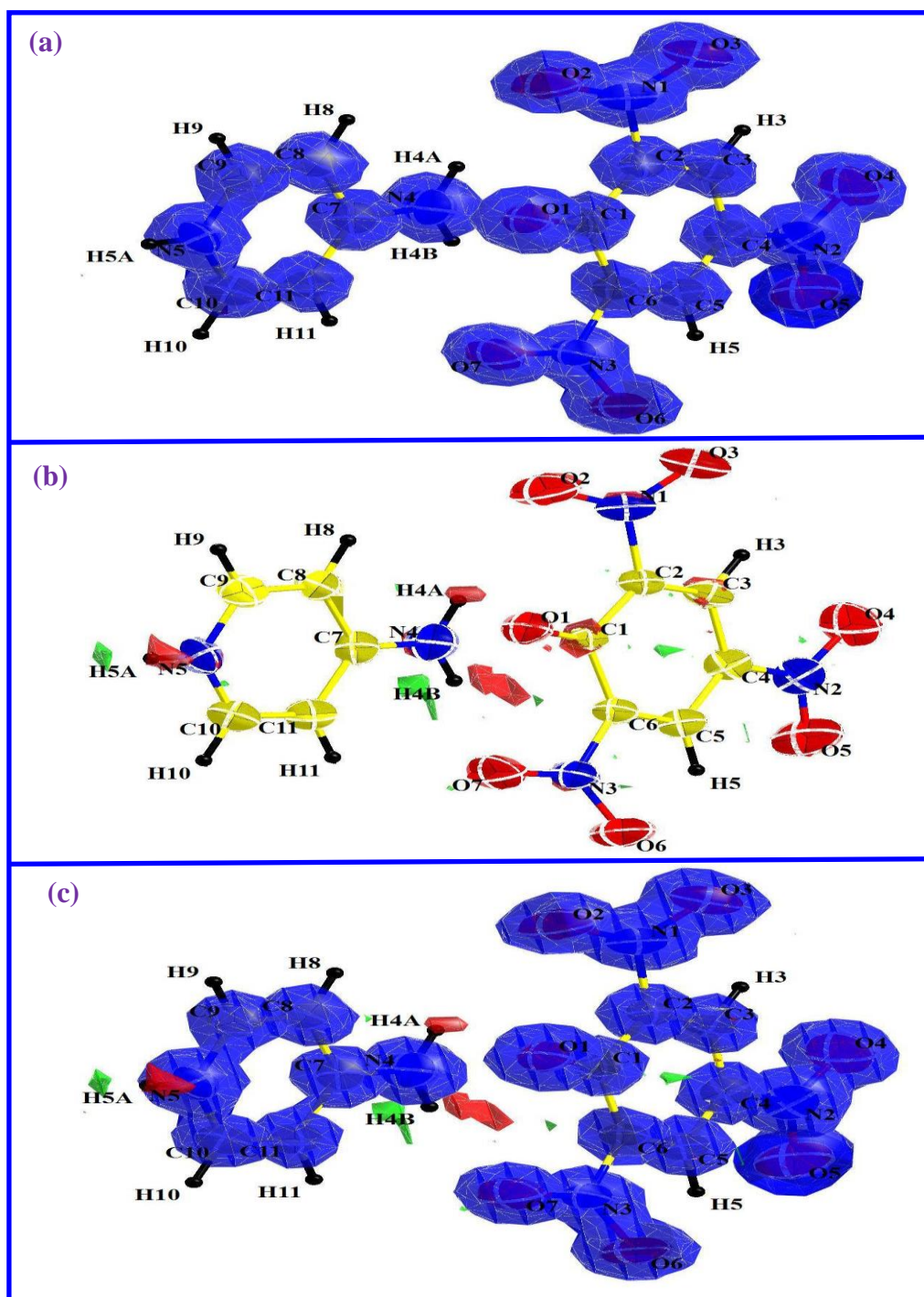


Fig.3.4.9. Electron density mappings of APP (a) F_{obs} (b) $F_{obs} - F_{cal}$ (c) F_{obs} & $F_{obs} - F_{cal}$

Powder XRD

The sharp peaks in XRD pattern indicate the good crystallinity. All observed diffraction peaks were indexed. Most of the peak positions in powder X-ray

diffraction and simulated pattern from single crystal XRD coincide (**Fig.3.4.10**). However, the relative intensities differ. This could be due to the preferred orientation of the sample used for diffractogram measurement. Also, the mosaic spread of powder and single crystal pattern may differ resulting in intensity variations.

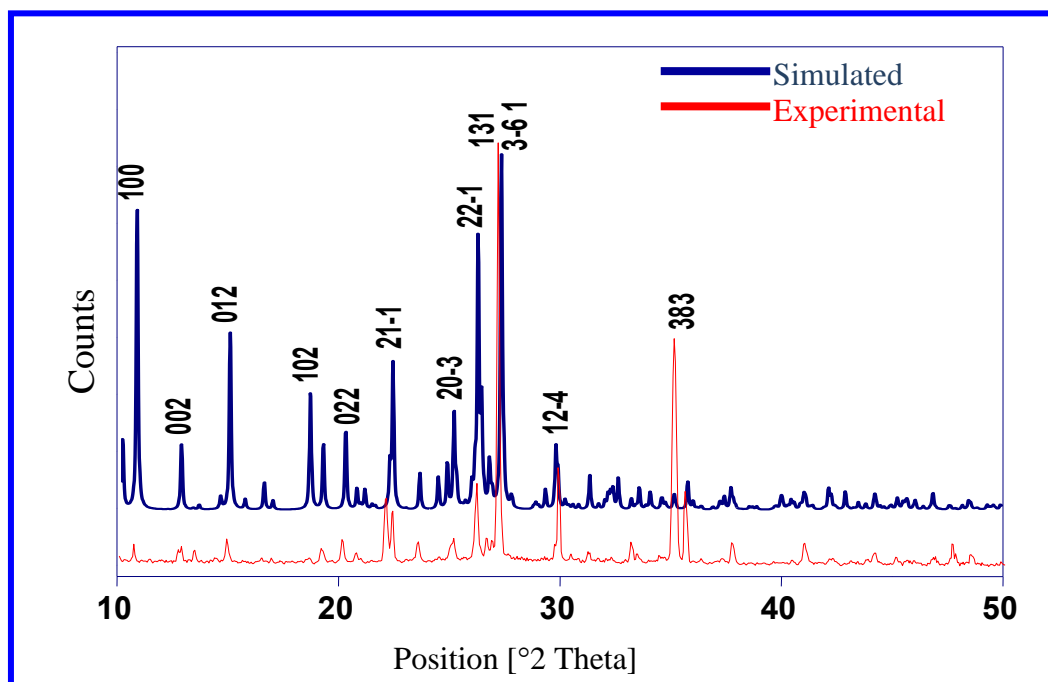


Fig.3.4.10 Simulated and experimental powder XRD patterns of APP

First-order molecular hyperpolarizability

Theoretical calculations were performed using the *GAUSSIAN09W* [10] by Hartree – Fock method, a program package on a personal computer without any constraints on the geometry using 6-31G (d, p) as the basis set [19] with *GAUSSVIEW 5.0* molecular visualization [20]. The calculated first-order molecular hyperpolarizability (β) is 7.394×10^{-30} esu (> 26 times of urea) (**Table 3.4.3**). High beta value is a required property of an NLO material and it appears that by proper designing it is possible to sustain nonlinearity at the macro level.

Table 3.4.3 The calculated β components, β_{tot} value (esu), dipole moment (μ , D) and HOMO – LUMO (eV) of APP

β_{xxx}	1217.401
β_{xxy}	270.237
β_{xyy}	-490.608
β_{yyy}	-83.433
β_{xxz}	156.793
β_{xyz}	-243.907
β_{yyz}	-41.029
β_{xzz}	94.337
β_{yxx}	15.795
β_{zzz}	15.357
$\beta_{tot} (\times 10^{-30})$	7.394
μ	18.880
E_{HOMO}	-0.311
E_{LUMO}	0.063
$E_{HOMO} - E_{LUMO}$	0.374

Conclusions

Pale yellow coloured 4-aminopyridinium picrate crystals were grown from an equimolar mixture of methanol and acetone and characterized. The product formation was confirmed by FT-IR and single crystal XRD analysis. Comparison of bond lengths and angles of theoretical and experimental studies shows slight variations. APP crystallizes in a space group $P2_1/c$ with four molecules in an unit cell. A good transmission in the visible region is observed with a direct band gap energy of 4.79 eV and an indirect band gap

energy of 4.96 eV. The powder X-ray diffraction study shows the good crystallinity of the material. The crystal cohesion is achieved by intermolecular hydrogen bonds between picrate anions and amino groups of 4-aminopyridinium ions. The electron density mapping shows no structural disorder in the solved structure with low R factor. High β value is associated with facile charge transfer.

References

- [1] A. S. Dayananda, J. P. Jasinski, J. A. Golen, H. S. Yathirajan, C. R. Raju, *Acta Cryst.*, **E67** (2011), o2502.
- [2] M. Sethuram, G. Bhargavi, M. V. Rajasehakaran, M. Dhandapania, G. Amirthaganesan, *Optik.*, **125** (2014), 55.
- [3] V. Bertolasi, P. Gilli, G. Gilli, *Cryst. Growth Des.*, **11** (2011), 2724.
- [4] R. P. Sharma, R. Sharma, R. Bala, P. Venugopalan, *J. Coord. Chem.*, **58** (2005), 899.
- [5] R. S. Mulliken, W. B. Person, *Wiley-Interscience*, New York and London (1969), 498.
- [6] A. Chandramohan, R. Bharathikannan, M. A. Kandhaswamy, J. Chandrasekaran, V. Kandavelu, *Cryst. Res. Technol.*, **43** (2008), 93.
- [7] A. Chandramohan, R. Bharathikannan, J. Chandrasekaran, P. Maadeswaran, R. Renganathan, V. Kandavelu, *J. Cryst. Growth.*, **310** (2008), 5409.
- [8] G. Anandha Babu, A. Chandramohan, P. Ramasamy, G. Bhagavannarayana, Babu Varghese, *Mater. Res. Bull.*, **46** (2011), 464.

- [9] P. Ramesh, R. Akalya, A. Chandramohan, M. N. Ponnuswamy, *Acta Cryst.*, **E66** (2010), o1000.
- [10] M. J. Frisch *et al.*, Gaussian 09 Revision-C.01, Gaussian, Inc., Wallingford, CT, (2009).
- [11] R. S. Mulliken, *J. Am. Chem. Soc.*, **74** (1952), 811.
- [12] R. S. Mulliken, *J. Chem. Phys.*, **23** (1955), 1833.
- [13] P. Kubelka, F. Munk, Ein Beitrag zur Optik der Farbanstriche, *Z. Tech. Phys. (Leipzig)*., **12** (1931), 593.
- [14] G. M. Sheldrick, *Acta Cryst.*, **A64** (2008), 112.
- [15] O. V. Dolomanov, L. J. Bourhis, R. J. Gildea, J. A. K. Howard, H. Puschmann, *J. Appl. Cryst.*, **42** (2009), 339.
- [16] L. Palatinus, *Acta Cryst.*, **B69** (2013), 1.
- [17] C. B. Hubschle, G. M. Sheldrick, B. Dittrich ShelXle: a Qt graphical user interface for SHELXL, *J. Appl. Cryst.*, **44** (2011), 1281.
- [18] P. Ramesh, R. Akalya, A. Chandramohan, M. N. Ponnuswamy, *Acta Cryst.*, **E66** (2010), o1000.
- [19] B. Schlegel, *J. Comput. Chem.*, **3** (1982), 214.
- [20] A. Frisch, A. B. Nielson, A. J. Holder, GAUSSVIEW User Manual, Gaussian Inc., Pittsburgh, PA, (2000).

CHAPTER-3.5

Synthesis, structure, crystal growth and computational studies of tetrakis(thiourea)copper(I) picrate

Single crystals of tetrakis(thiourea)copper(I) picrate (TCP) were grown by slow evaporation technique at constant temperature. The structure is elucidated by single crystal XRD analysis. The investigations disclose that the molecule is assembled with N-H \cdots O, C-H \cdots S and H \cdots H stacking interactions. Intra- and intermolecular hydrogen bonding interactions demonstrate supramolecular architecture in the crystal packing. The copper metal is coordinated by four thiourea groups with Cu-S-C bond angles ranging from 113.94 to 113.99° and Cu-S bond lengths lying in the range 2.270 to 2.285 Å. Hirshfeld surface and fingerprint plot analysis were used to quantify the percentage of bonding interactions in the title compound. Scanning electron microscopy reveals the surface morphology of the grown crystal. Optimized molecular geometry, vibrational patterns of TCP were derived from density functional theory (DFT) computations and the results compared with experiment. A very large first-order molecular hyperpolarizability of ~43 times of urea possessed by the title compound is rationalized by proton transfer induced charge transfer. HOMO-LUMO energy gaps were calculated for the unit cell and it matches with the values derived by density of states (DOS) spectrum.

Introduction

A number of copper thiourea complexes have been reported [1-6]. Tris(thiourea)copper(I) chloride, a promising candidate, has been extensively

studied for its linear and nonlinear optical properties, crystal growth, mechanical properties, and laser induced damage [7,8]. The modifying of organic crystal structure to meet the demands of particular applications have been predicated upon the understanding the principles of supramolecular aggregation patterns. Recently, we have reported the growth and characterization of cadmium(II) picrate [9] and tetrakis(thiourea)zinc(II) picrate [10].

In the present work, we report the structure of tetrakis(thiourea)copper(I) picrate for the first time, characterized by FT-IR, FT-Raman and density functional theory computations. This computational approach is purely on geometrical basis to study molecular structural properties by theoretical methods. All the interactions were quantified using fingerprint and Hirshfeld surface analysis.

Synthesis and Crystal growth

Tetrakis(thiourea)copper(I) picrate was synthesized by mixing stoichiometric quantities of copper chloride (Qualigens), thiourea (EM), and picric acid (Qualigens) in the molar ratio of 1:4:1. The reactants were dissolved in water, thoroughly mixed using a magnetic stirrer (3 h), and TCP was obtained as yellow color precipitate. The precipitate was then collected on a filter and recrystallized using water–acetone mixture (1:1, v/v). Single crystals of TCP were grown at room temperature (35 °C) by slow evaporation of water–acetone mixture (40:60 v/v). Numerous tiny crystals were formed at the bottom of the container due to spontaneous nucleation. Good optical quality green crystals were harvested after a period of 6–7 d (Fig.3.5.1).

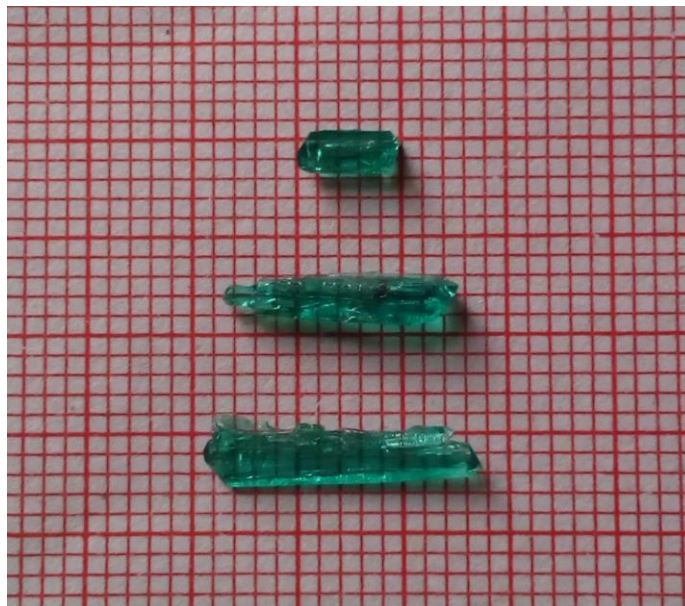


Fig.3.5.1 Photographs of as-grown crystals of TCP

Results and discussion

Structure descriptions

Structure is elucidated by single crystal X-ray diffraction technique. The *ORTEP* and packing diagrams of TCP are given in **Figs.3.5.2** and **3.5.3**. It crystallizes in the orthorhombic system with centrosymmetric space group *Fddd* and the crystal data are given in the **Table 3.5.1**. The crystal packing of this complex is mainly determined by N-H \cdots O and C-H \cdots S intermolecular hydrogen bonds. Tetrahedran image of TCP indicating N-H \cdots O interactions are displayed in **Fig.3.5.4**. The crystal structure can be described as being made up of discrete complex molecule formed by Cu-centered coordination tetrahedra with four sulfur atoms from four thiourea molecules and one picrate molecule at the apices. The Cu-S-C bond angles range from 113.94 to 113.99°, S-Cu-S bond angles widely range from 112–129° and Cu-S bond lengths lying in the range 2.20 – 2.30 Å. The distance between the cadmium and oxygen atom of picrate anions is 5.32 Å. The internal angle at

the carbon atom to which oxygen bonded is at $\sim 118.56^\circ$, while the internal angles at the adjacent carbon atoms in the ring are 118.21 and 119.92° . There are intermolecular hydrogen bonds between picrate anion and $[\text{Cu}(\text{tu})_4]\text{C}_6\text{H}_2\text{O}_7$. The strongest hydrogen bonds are observed for $\text{N}(1)\text{--H}(1\text{b})\text{--O}(2)$ and $\text{N}(3)\text{--H}(3\text{A})\text{--O}2$. Hydrogen bonding interactions of TCP are listed in **Table 3.5.2**. The bifurcated hydrogen bonding interactions are assembled with distances of 2.072 and 2.097 \AA (**Fig.3.5.5**).

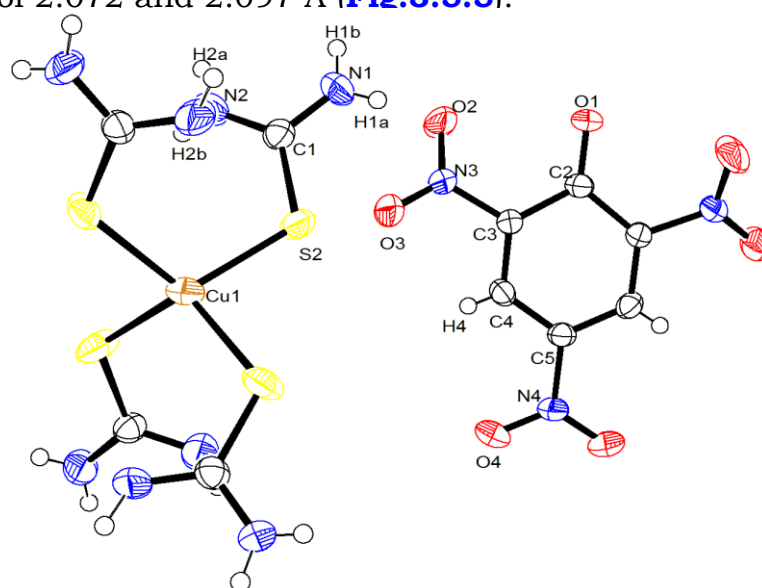


Fig.3.5.2 The *ORTEP* of the asymmetric unit of TCP. Ellipsoids are drawn at the 40% probability level

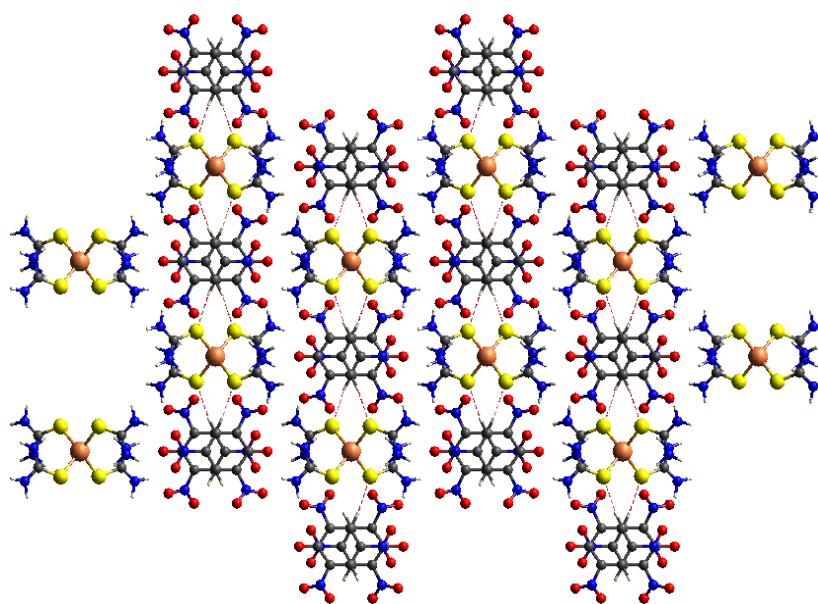


Fig.3.5.3 (a) Packing network of the molecules connected with the $\text{C}\text{--H}\cdots\text{S}$ chain down along the a -axis

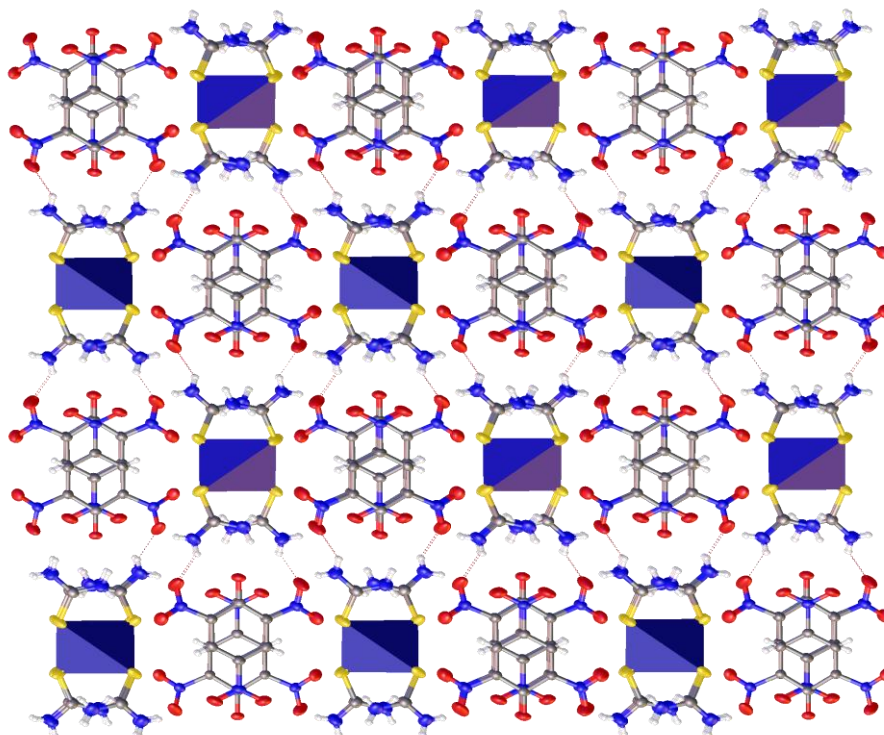


Fig.3.5.4 Packing projections of N-H...O along *ab*-axis

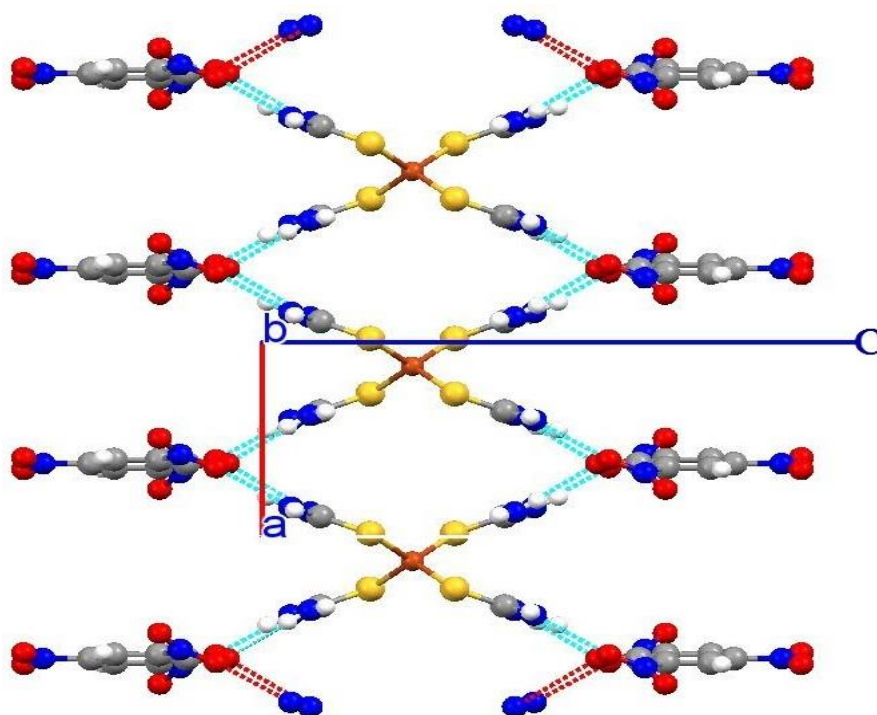


Fig.3.5.5. Bifurcated N-H...O interactions along *b*-axis

Table 3.5.1 Crystal data and structure refinement for TCP.	
Empirical formula	C ₁₆ H ₂₀ CuN ₁₄ O ₁₄ S ₄
Formula weight	824.28
Temperature/K	100
Crystal system	orthorhombic
Space group	<i>Fddd</i>
a/Å	6.9531(12)
b/Å	24.499(4)
c/Å	36.193(6)
α/°	90
β/°	90
γ/°	90
Volume/Å ³	6165.2(18)
Z	8
ρ _{calc} /cm ³	1.7760
μ/mm ⁻¹	1.068
F(000)	3360.7
Crystal size/mm ³	0.3 × 0.3 × 0.3
Radiation	Mo Kα (λ = 0.71073)
2θ range for data collection/°	4.02 to 52.02
Index ranges	-8 ≤ h ≤ 8, -30 ≤ k ≤ 30, -44 ≤ l ≤ 44
Reflections collected	16024
Independent reflections	1145 [R _{int} = 0.0812, R _{sigma} = 0.0498]
Data/restraints/parameters	1145/0/135
Goodness-of-fit on F ²	1.082
Final R indexes [I ≥ 2σ (I)]	R ₁ = 0.0621, wR ₂ = 0.1493
Final R indexes [all data]	R ₁ = 0.0621, wR ₂ = 0.1493
Largest diff. peak/hole / e Å ⁻³	0.72/-0.77
CCDC number	CCDC1061517

Table 3.5.2. Hydrogen Bonds for TCP				
D – H ...A	d(D-H)/Å	d(H-A)/Å	d(D-A)/Å	D-H-A/°
N1 H1b O2 ¹	0.79 (7)	2.09 (8)	2.762 (7)	144 (7)

¹3/2-X,1/2-Y,-Z

External morphology

Scanning electron microscopic images are given in **Fig.3.5.6**. From the microscopic images, one can observe the existence of large patches on the surface. Small prismatic shaped particles appeared at the surface. Energy dispersive spectroscopy confirms the quantities of elements present (**Table 3.5.3**).

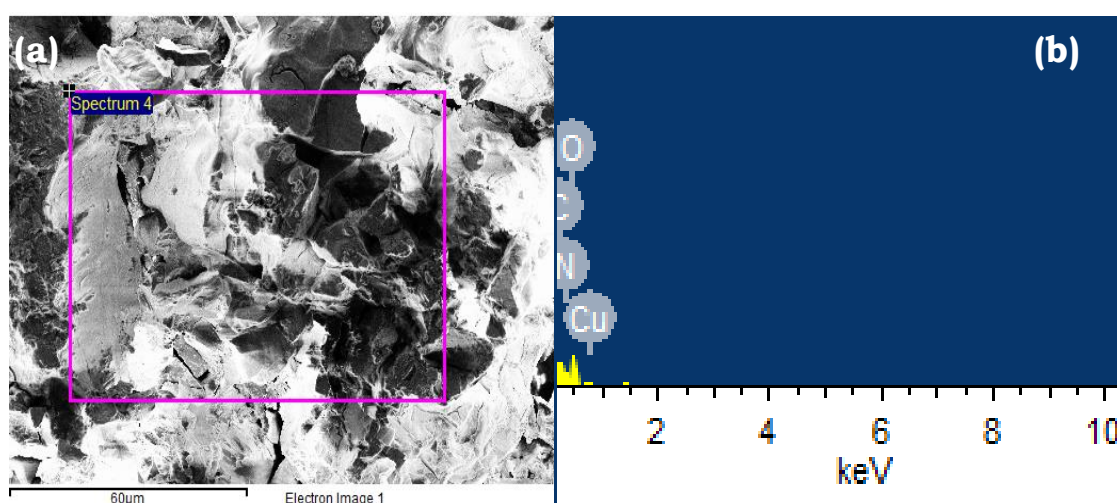


Fig.3.5.6 (a) SEM micrographs of TCP (b) EDS spectrum

Table 3.5.3. EDS of TCP

Element	Weight%	Atomic%
C	25.27	30.99
N	25.54	26.85
O	43.26	39.82
S	4.22	1.94
Cu	1.70	0.39
Total	100.00	

FT-IR

The aromatic ring S-C stretching and N-C bending vibrations are at 1545 cm^{-1} , whereas they are computationally at 1528 cm^{-1} . Aliphatic C-N stretching vibrations appeared at 1855 cm^{-1} , but it is at $\sim 1859\text{ cm}^{-1}$ in computational studies. The C-H stretching vibrations were observed at 3201 cm^{-1} and 3212 cm^{-1} whereas in computational studies no peaks observed. Experimental and theoretical FT-IR vibrational patterns were displayed in

Fig.3.5.7.

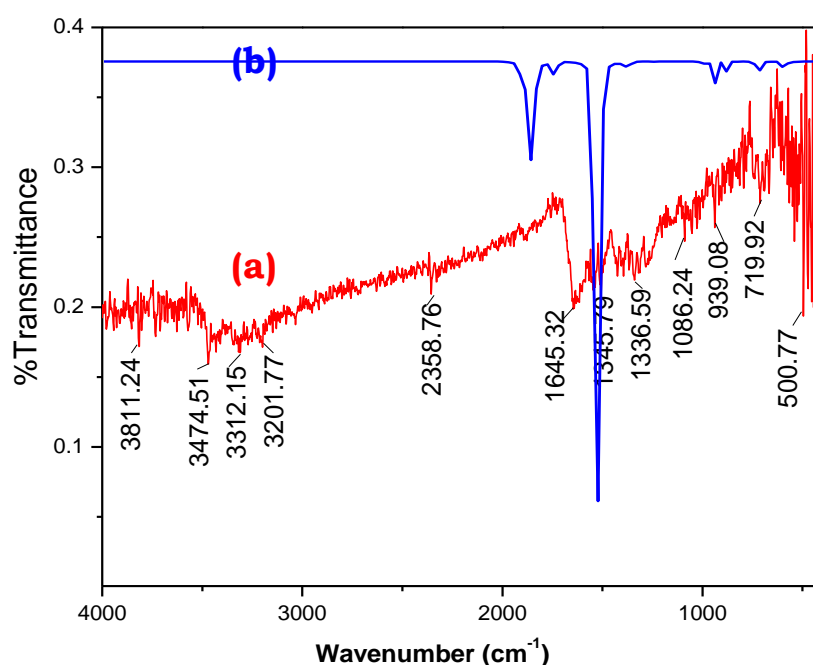


Fig.3.5.7 FT-IR vibrational patterns (a) Experimental (b) Computational

Hirshfeld and Fingerprint analysis

The Hirshfeld surfaces were mapped using d_{norm} , which is a normalized contact. Multiple N-H \cdots O interactions are indicated as spikes at the fingerprint region on either side of the diagonal d_e and d_i . The N-H \cdots O interactions contribute 52.7% to the total area of the Hirshfeld surface while those of the H \cdots O (d_i) and O \cdots H (d_e) contribute 52.7%, and 5.9%

respectively. These contacts display different characteristic ranges of d_e and d_i . The $O\cdots H$ interactions, shown as sharp spikes directed towards the lower left corner of each plot, are due to the intramolecular hydrogen bonding interactions (Fig.3.5.8).

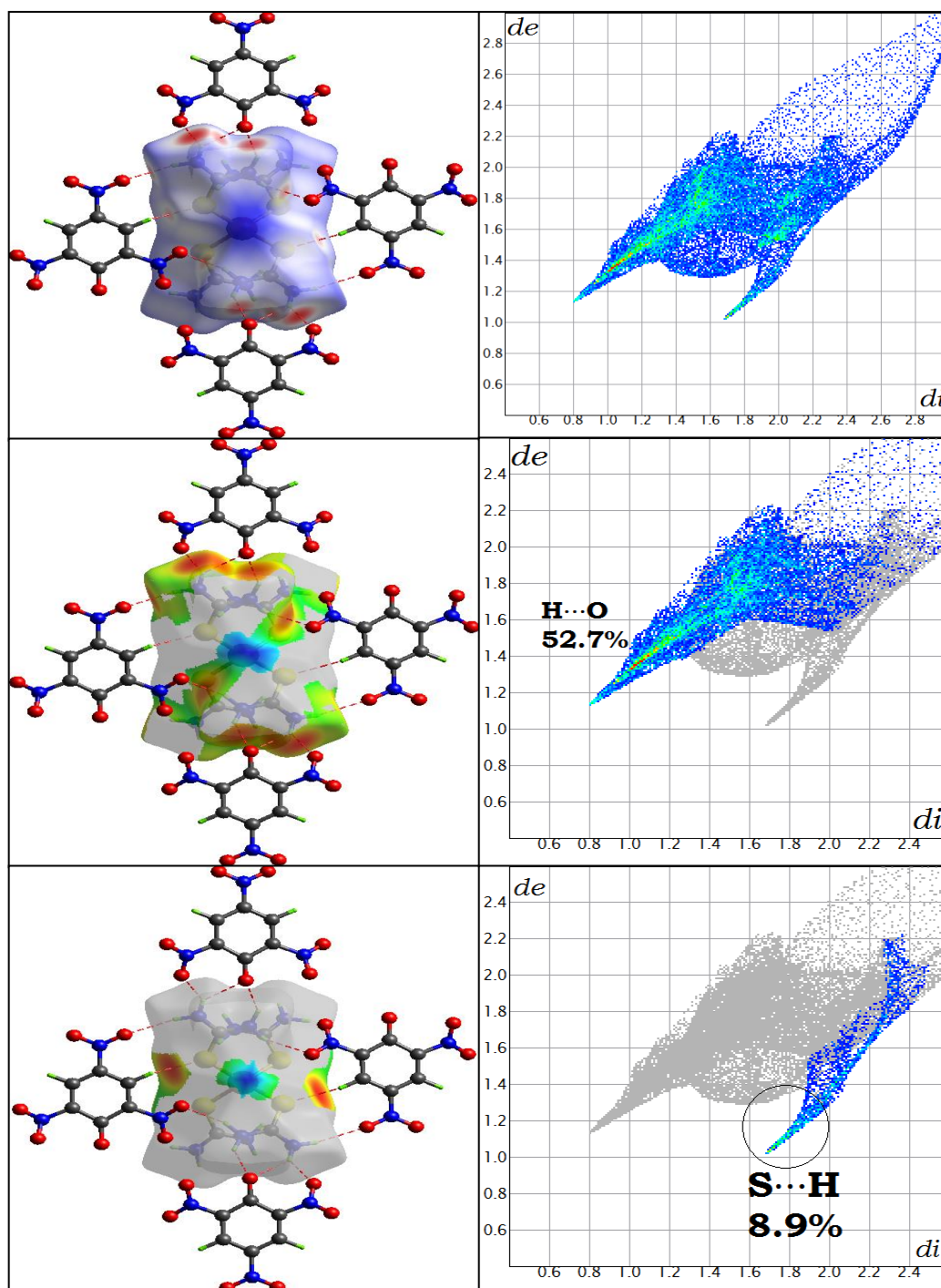


Fig.3.5.8 Hirshfeld surface analysis of TCP. [a] d_{norm} (All interactions) [b] d_e ($H\cdots O$ interactions in d_e surface) [c] d_i ($S\cdots H$ interactions in d_i surface) (d), (e), (f) 2D-Fingerprint plots of corresponding surfaces

Computational studies

Quantum chemical calculation was performed from the crystal data with DFT-B3LYP method at the 3-21G basis set, using *GAUSSIAN09W* program. The calculated first-order molecular hyperpolarizability (β) of the specimen is 11.29×10^{-30} esu *i.e.*, ~43 times of urea (**Table.3.5.4**). The maximum value of hyperpolarizability is due to the nonzero μ values. High β is associated with high charge transfer. The nonlinearity could not be translated at the macro level and negligible second harmonic generation efficiency is observed due to orientation effect resulting in a centrosymmetric structure. Large β clearly evidences that TCP is a promising NLO material in molecular level.

Table 3.5.4 The calculated dipole moment (in D), β components (a.u.) and β_{tot} value (in esu)

First-order molecular hyperpolarizability	
β_{xxx}	-178.690
β_{xyy}	-143.200
β_{yyy}	-219.590
β_{xxx}	-439.610
β_{yyz}	8.710
β_{xzz}	-776.680
β_{yzz}	-37.610
β_{zzz}	-104.520
β_{xzz}	-37.610
β_{yzz}	1803.580
β_{tot}	11.290
Dipole moment	
μ_x	36.730
μ_y	1.840
μ_z	1.470
μ	36.800

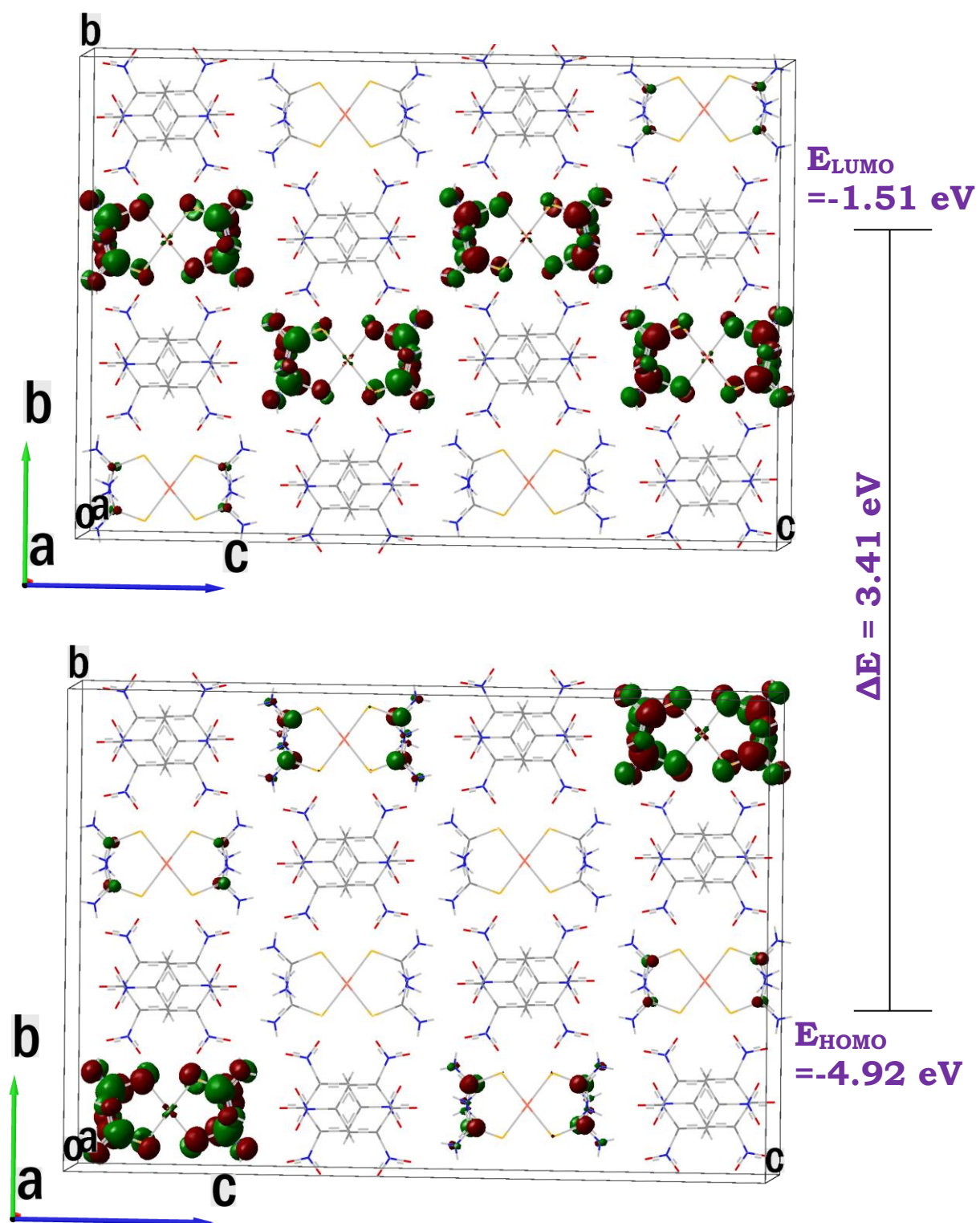


Fig.3.5.9. HOMO-LUMO energy gaps in an unit cell

Fig.3.5.9 shows the highest occupied molecular orbital (HOMO) and lowest unoccupied molecular orbital (LUMO) of TCP. Smallest HOMO-LUMO energy gap is responsible for intramolecular charge transfer. In the present work, the HOMO-LUMO energies for the unit cell are estimated. HOMO energy is located at the center of unit cell, whereas energy LUMO transfer is away from the unit cell and the energy gap is 3.41 eV.

Molecular electrostatic potential (MEP) is the common technique to identify the reactive site at the molecular surface. MEP at a point in the space around a molecule provides a sign of the net electrostatic effect generated at that point by the total charge distribution (electron + proton + nucleus) of the atom or molecule. The values of the electrostatic potential at the surface are indicated by dissimilar colors as mentioned in the previous chapter. The electrophiles tend to be negative and the nucleophiles tend to be the regions of positive MEP. In TCP (**Fig.3.5.9a**), the picrate region acts as more electrophilic region and it is denoted as red color. Likewise, the nucleophilic region was graphically shown as blue colour. The electrophilic and nucleophilic colour range is from -0.126 to 0.126 e. The corresponding contour maps are graphically represented in **Fig.3.5.9b**. The electronic density of states spectrum is displayed in **Fig.3.5.10**. The fundamental absorption spectrum of solid gives information about critical points in the optical density of states [11]. This information can be used to adjust parameters of the band structure. Theoretically determined energy gap well match with gap estimated using HOMO-LUMO (**Fig 3.5.11**).

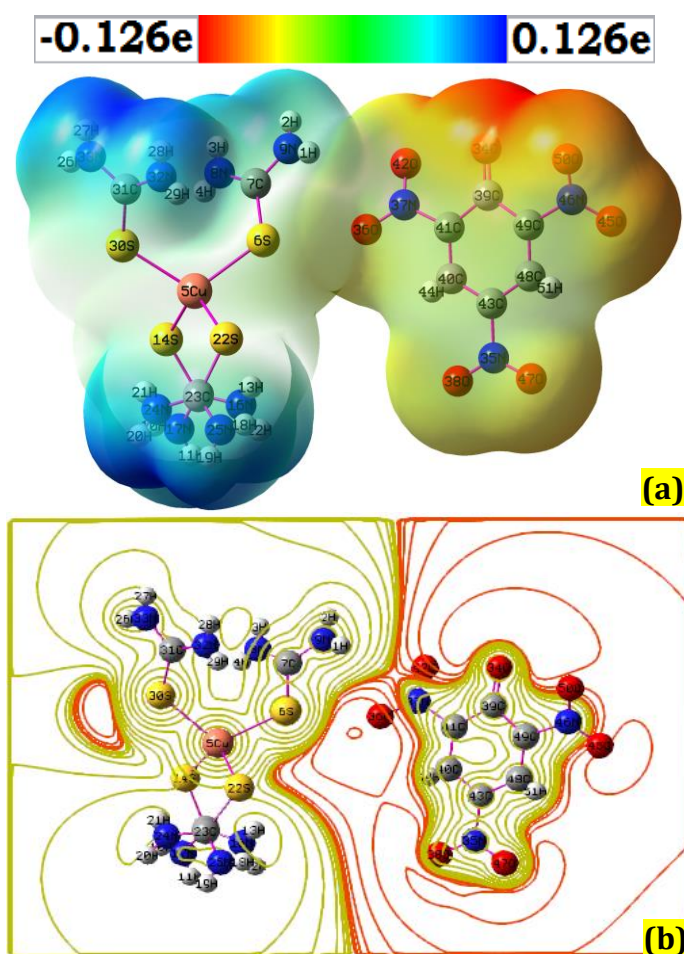


Fig.3.5.10 (a) Molecular electrostatic potential map (b) Contour map of ESP

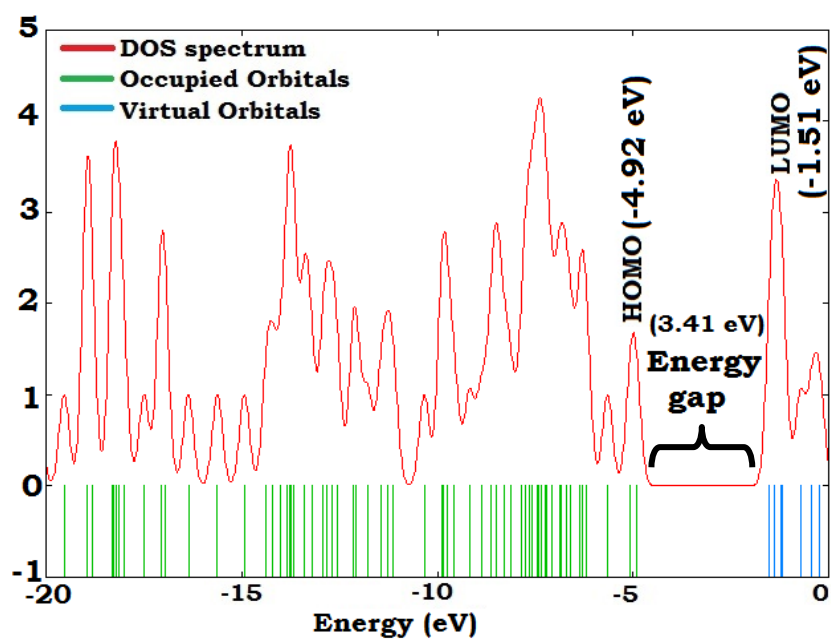


Fig. 3.5.11 Density of states spectra of TCP

Conclusions

The single crystals of TCP were successfully synthesized, grown by slow evaporation and characterized by FT-IR. The crystal cohesion is achieved by strong N–H···O and supramolecular C–H···S hydrogen bonding interactions. The external morphological differences were examined by scanning electron microscopic technique. Hirshfeld and fingerprint plots were used to quantify and analyze the intermolecular interactions in the crystal structures. The HOMO-LUMO energy gap was found to be 3.41 eV. Theoretically, the reactivity site around the surface is investigated by molecular electrostatic potential maps and it reveals the regions of electrophilic and nucleophilic sites. High values of hyperpolarizability, ~43 times of urea, are associated with facile charge transfer.

References

- [1] H. C. Mruthyunjaya, A. R. Vasudeva Murthy, *Anal. Chem.*, **41** (1) (1969), 186–188.
- [2] Salomea Krzewska, Halina Podsiadły, Lech Pajdowski, *J. Inorg. & Nuclear Chem.*, **42** (1980), 89-94.
- [3] V. Igor Mironov, Lidija D. Tsvetodub, *J. Sol. Chem.*, **25** (1996), 315-325.
- [4] C.J. Doona, D.M. Stanbury, *Inorg. Chem.*, **35** (11) (1996), 3210-3216.
- [5] D. Valigura, G. Ondrejovič and J. Krätšmár-Šmogrovič, *Chem.*, **41** (2) (1987), 183-93.

- [6] Petra Bombicz, Ilpo Mutikainen, Malle Krunk, Tuula Leskelä, János Madarász, Lauri Niinistö, *Inorganica Chimica Acta*, **357** (2004), 513–525.
- [7] Carolyn B. Knobler, Yoshiharu Okaya, Ray Pepinsky., *Zeitschrift für Kristallographie.*, **111** (2010), 385–397.
- [8] K. Obler, IBM Thomas J. Watson, *Acta Cryst.*, **17** (1964), 928.
- [9] K. Muthu, SP. Meenakshisundaram, SC. Mojumdar, *J Therm Anal Calorim.*, **112** (2013), 1039–1045.
- [10] K. Muthu, SP. Meenakshisundaram, *Materials Letters*, **84** (2012), 56–58.
- [11] Manuel Cardona, *Journal of Research of the National Bureau of Standards-A. Physics and Chemistry*, **74** (1970), 2.

CHAPTER-3.6

Hyperpolarizability, Hirshfeld and Density functional theory computations of a nonlinear optical picrate

bis(2-nitroaniline) picrate single crystals were grown by slow evaporation growth technique using mixed solvent system ethanol-acetone (1:1,v/v) at constant temperature and structure is interpreted by single crystal XRD analysis. Inter- and intramolecular hydrogen bonding interactions were interpreted and crystal cohesion is architected by N-H \cdots O, O-H \cdots O, C-H \cdots N, H \cdots H, O \cdots O and $\pi\cdots\pi$ staking interactions. All the intermolecular interactions occurring in the crystal lattice were calculated using fingerprint analysis. Interaction strengths were graphically illustrated by Hirshfeld surface analysis. The band gap energy of BNP was estimated by the application of Kubelka–Munk algorithm. Electrostatic resonance spectrum reveals paramagnetic activity of the compound. Nonlinear optical (NLO) behaviour is confirmed by Kurtz-perry technique. Optimized geometry is derived by density functional theory calculations. The first-order molecular hyperpolarizability (β) and excited state energies were estimated by TD-DFT.

1. Introduction

Nonlinear optical single crystals have been developing progressively from the past years and these are essential in the electro-optical field. Optical crystals exhibit several interesting physical properties such as phase transitions, electric, dielectric, ferroelectric and piezoelectric behavior [1,2].

Organic NLO materials usually possess π -electron conjugated system with an electron donor group on one end and an acceptor group on the other end, which leads to a push-pull conjugated structure, leading to their applications in optical and optoelectronic devices [3,4]. Structural variations ensure due to polymorphic transitions of simulated methodology are investigated earlier [5,6]. Most of the picrates are a family of conjugated NLO chromophores that reveal good second harmonic generation (SHG) and transparency [7,8]. Several complexes of picric acid with organic molecules exhibit nonlinear optical applications [9]. Recently, we have investigated the synthesis, structure, growth and characterization of p-toluidinium picrate [10], 2-amino-5-nitrobenzophenonium picrate [11], 4-aminobenzophenonium picrate [12] and 4-aminopyridinium picrate [13].

In the present work, we report the polymorphic structure, UV-DRS, Fluorescence, density functional theory computations of first order molecular hyperpolarisability, Hirshfeld surface analysis, fingerprint plots, excitation energies, mulliken & natural population analysis.

2. Experimental procedure

2.1. Synthesis and growth

Bis(2-Nitroaniline) picrate (BNP) was synthesized by mixing stoichiometric amounts of 2-nitroaniline (Sigma-Aldrich) and picric acid (Sigma-Aldrich) in the ratio of 2:1 using methanol as solvent. The mixture was stirred at room temperature for 3 h and BNP was achieved as yellow color precipitate. The product was purified by repeated recrystallization

process using mixed solvent, methanol and acetone (1:1, v/v). Recrystallized BNP was dissolved in mixed solvent system (methanol:acetone, 1:1, v/v) and the solution warmed with constant stirring for an hour to avoid co-precipitation of multiple phases. Transparent crystals were grown-up by slow evaporation solution growth technique and the crystals were collected after a period of 10-12 days. Photograph of BNP is displayed in [Fig. 3.6.1](#).

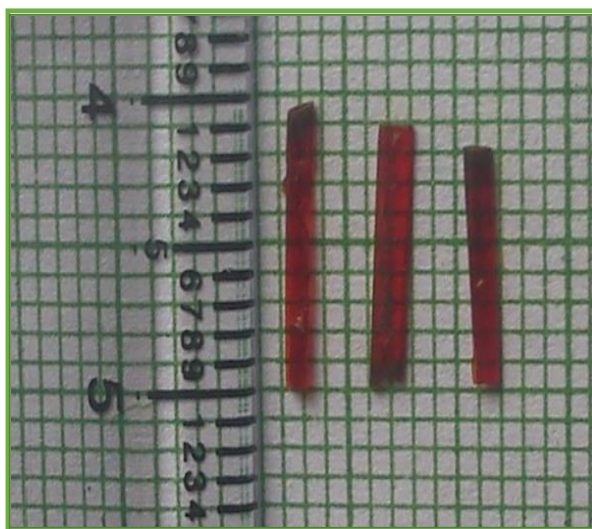


Fig. 3.6.1 Photograph of as-grown crystals of BNP

Computational details

The complete theoretical calculations were performed at density functional theoretical level with B3LYP/6-31G(d,p) as basis set using *Gaussian09W* [14] program package. Images are visualized using the *GaussView 5.0* visualization program [15]. The vibrational wavenumbers of the normal modes were calculated by total energy distribution (TED) using VEDA 4 package [16]. Excitation energy of the molecule is estimated by TD-DFT, CIS and ZINDO methods. Hirshfeld surfaces and fingerprint plots were generated from the crystal data using the DFT method with 6-31G(d,p) as basis set [17].

Characterization techniques

The structural analysis of BNP was carried out using Bruker AXS (Kappa APEXII) X-ray diffractometer with Mo K α radiation ($\lambda=0.71073$ Å). The crystal was kept at 293.15 K during data collection. Using *Olex2* [18], the structure was solved with the '*olex2.solve*' [19] structure solution program using Charge Flipping and refined with the '*olex2.refine*' [19] refinement package using Gauss-Newton minimisation. Crystal Data for C₃₆H₃₀N₁₄O₂₂ ($M=1010.72$ g/mol): monoclinic, space group *Cc*, μ (Mo K α) = 0.172 mm⁻¹, $D_{calc} = 2.0355$ g/cm³, 9444 reflections measured ($5.42^\circ \leq 2\theta \leq 56.06^\circ$), 3637 unique ($R_{int} = 0.0280$, $R_{sigma} = 0.0294$) which were used in all calculations. The final R_1 was 0.0585 ($I \geq 2u(I)$) and wR_2 was 0.1736 (all data). NLO property (SHG) of BNP is measured by Kurtz and Perry technique [20,21]. Electronic absorption spectra were recorded on a Varian Model Cary 100 UV-vis spectrometer. Diffuse reflectance spectra of the samples were recorded using the DRA-CA-30I. Fluorescence excitation and emission spectra were recorded on a Horiba Jobin Yvon Model FL3-22 Fluorolog spectrofluorimeter. ESR spectra were recorded using Bruker-ER073 instrument equipped with an EMX micro X-source for X band measurement.

3. Results and discussion

3.1 Optimized geometry

The optimized molecular structure of BNP is showed in Fig. 3.6.2b and it closely resembles the XRD structure. Fig 3.6.2a represents the intramolecular interactions in BNP. Red colour lines in contour map (Fig

3.6.2c) indicates high reactive site and yellow coloured lines represents very less reactivity.

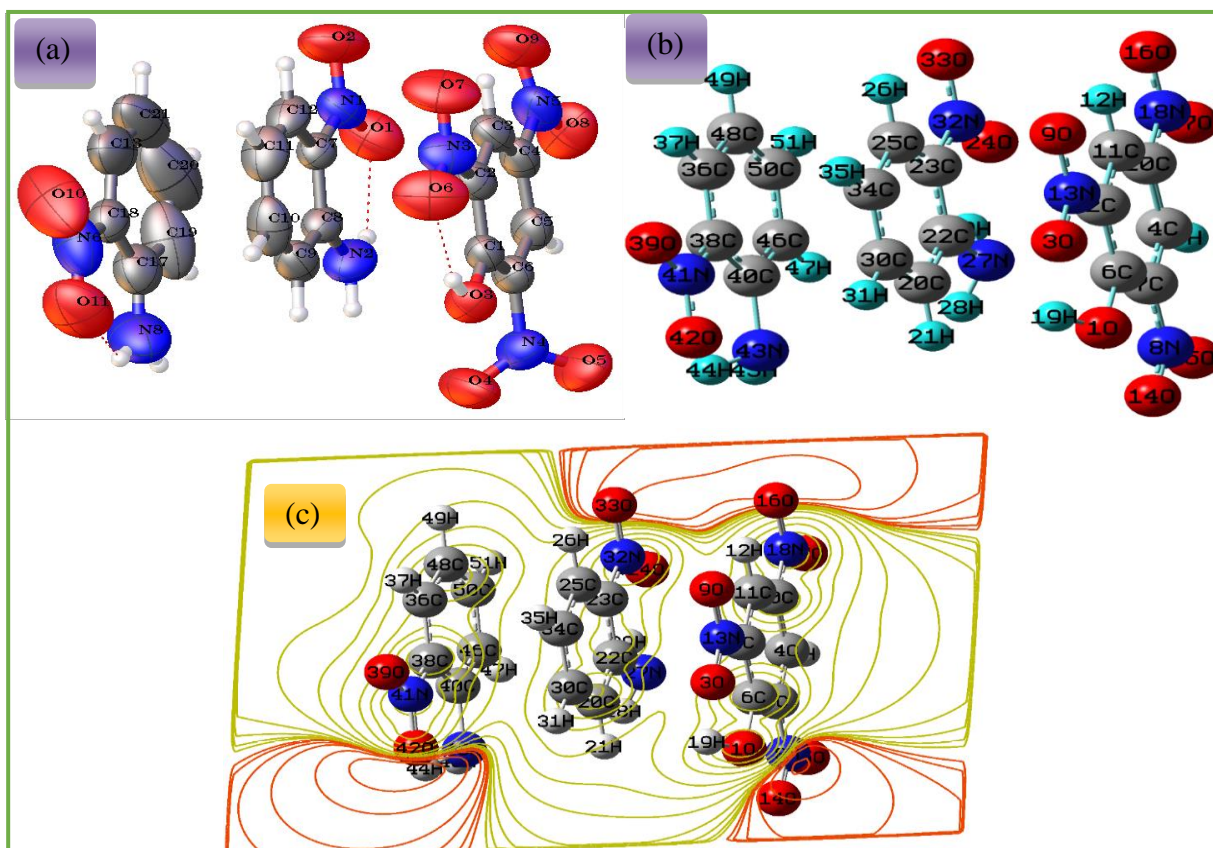


Fig. 3.6.2 Molecular structure of BNP (a) Ellipsoid plot (b) Optimized structure

The atomic charge transfer of the atoms present in BNP is accomplished by Mulliken population investigation [22,23], presented in Fig. 3.6.3 and the analogous charge values are recorded in Table 3.6.2. Mulliken atomic charges have an important portion in the applications of quantum mechanical calculation to molecular construction. From the detailed atomic charge values, nitrogen (-0.627,-0.814,-0.39,-0.88 e) and oxygen (-0.745, -0.792 e) in BNP had a large negative charge and acting as electron donors. All the hydrogen (0.216/0.206/0.229/0.387 e) atoms disclose positive charge, which are acceptor atoms and it might be due to the attachment of extra electronegative atoms.

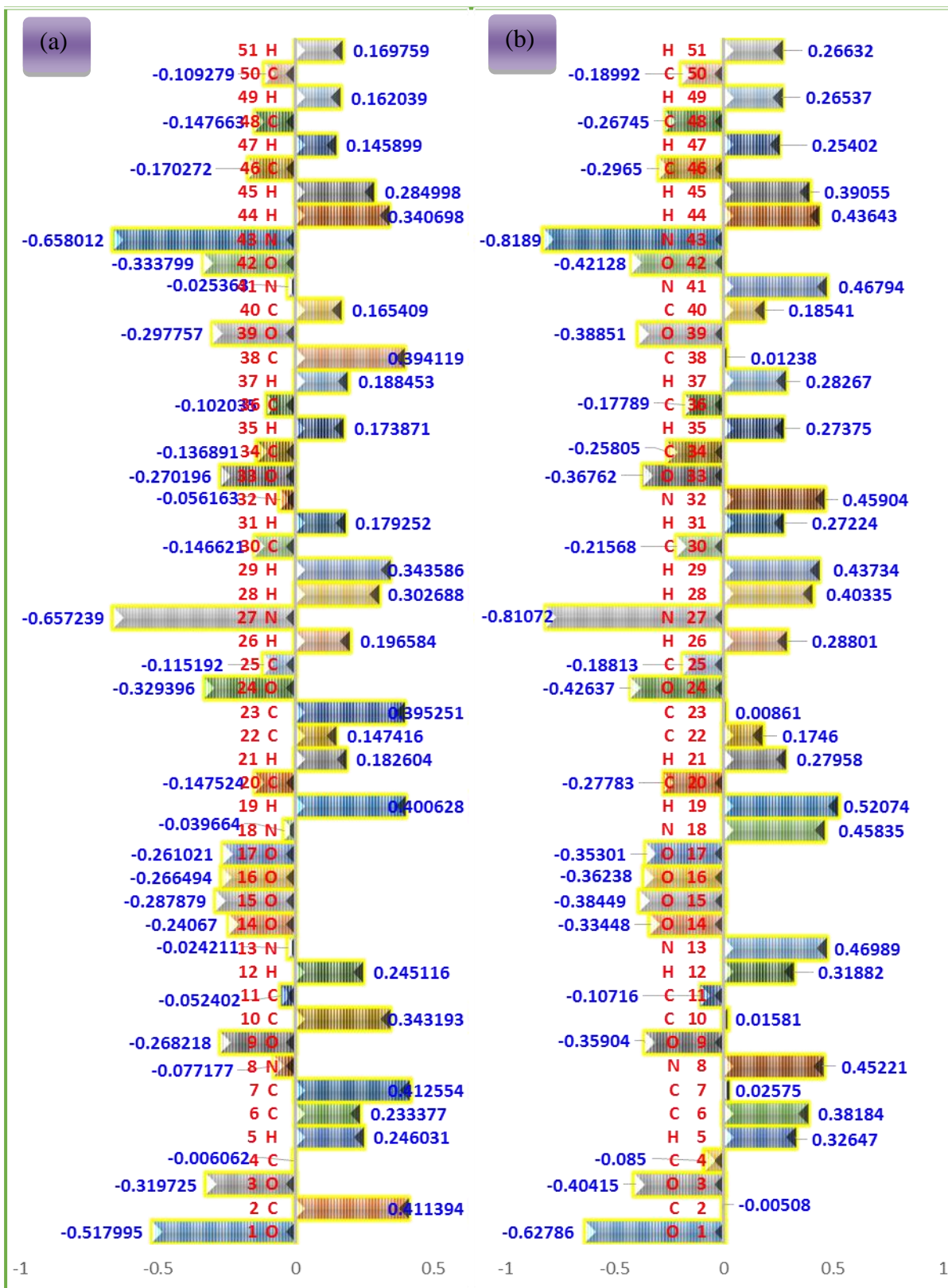


Fig. 3.6.3 (a) Bar-chart of Mulliken atomic charges (b) Bar-chart of Natural charges

Table 3.6.1. Atomic charge population [DFT, 6-31G (d, p)] of BNP.

Mulliken population		Natural	
Atom	Charge/e	Atom	Charge/e
1 O	-0.517995	O 1	-0.62786
2 C	0.411394	C 2	-0.00508
3 O	-0.319725	O 3	-0.40415
4 C	-0.006062	C 4	-0.085
5 H	0.246031	H 5	0.32647
6 C	0.233377	C 6	0.38184
7 C	0.412554	C 7	0.02575
8 N	-0.077177	N 8	0.45221
9 O	-0.268218	O 9	-0.35904
10 C	0.343193	C 10	0.01581
11 C	-0.052402	C 11	-0.10716
12 H	0.245116	H 12	0.31882
13 N	-0.024211	N 13	0.46989
14 O	-0.24067	O 14	-0.33448
15 O	-0.287879	O 15	-0.38449
16 O	-0.266494	O 16	-0.36238
17 O	-0.261021	O 17	-0.35301
18 N	-0.039664	N 18	0.45835
19 H	0.400628	H 19	0.52074
20 C	-0.147524	C 20	-0.27783
21 H	0.182604	H 21	0.27958
22 C	0.147416	C 22	0.1746
23 C	0.395251	C 23	0.00861
24 O	-0.329396	O 24	-0.42637
25 C	-0.115192	C 25	-0.18813
26 H	0.196584	H 26	0.28801
27 N	-0.657239	N 27	-0.81072
28 H	0.302688	H 28	0.40335
29 H	0.343586	H 29	0.43734
30 C	-0.146621	C 30	-0.21568
31 H	0.179252	H 31	0.27224
32 N	-0.056163	N 32	0.45904
33 O	-0.270196	O 33	-0.36762
34 C	-0.136891	C 34	-0.25805
35 H	0.173871	H 35	0.27375
36 C	-0.102035	C 36	-0.17789
37 H	0.188453	H 37	0.28267
38 C	0.394119	C 38	0.01238
39 O	-0.297757	O 39	-0.38851
40 C	0.165409	C 40	0.18541

Most of the atomic charges are matches with the natural atomic charges. Minor differences in the Natural atomic charges and Mulliken atomic charges are noticed. The variation error between the natural and mulliken charges results has been expressed by root mean square (RMSD) deviation [24,25] using the following expression.

$$\text{RMSD} = \sqrt{\frac{1}{n-1} \sum_i^n (\gamma_i^{\text{Natural}} - \gamma_i^{\text{Mulliken}})^2}$$

where n is the number of the natural or mulliken data. The RMSD values are found to be 0.00001% error for Natural atomic charge and Mulliken atomic charges.

3.2. Time dependent density functional theory (TD-DFT) analysis

Absorbance spectrum of BNP illustrates minimum absorption in the visible region. To support experimental observations, the theoretical electronic excitation energies, absorption wavelengths and oscillator strengths were calculated by TD-DFT methods using *GAUSSIAN09W* program with basis set 3-21G by CAMB3LYP method. TD-DFT excitation energy is observed at ~376nm, experimentally is at ~380nm wavelength (Fig.3.6.4). Excitation energies detected from ZINDO, CIS are ~577 nm, ~305 nm respectively. From this we can conclude that, TD-DFT method is more reliable method than the other methods. Oscillator strengths of TD-DFT, ZINDO, CIS methods are 0.0309*f*, 0.0001*f* and 0.0002 *f* respectively. Fluorescence emission peak is absolved at the range of ~428 nm wavelength (Fig.3.6.5).

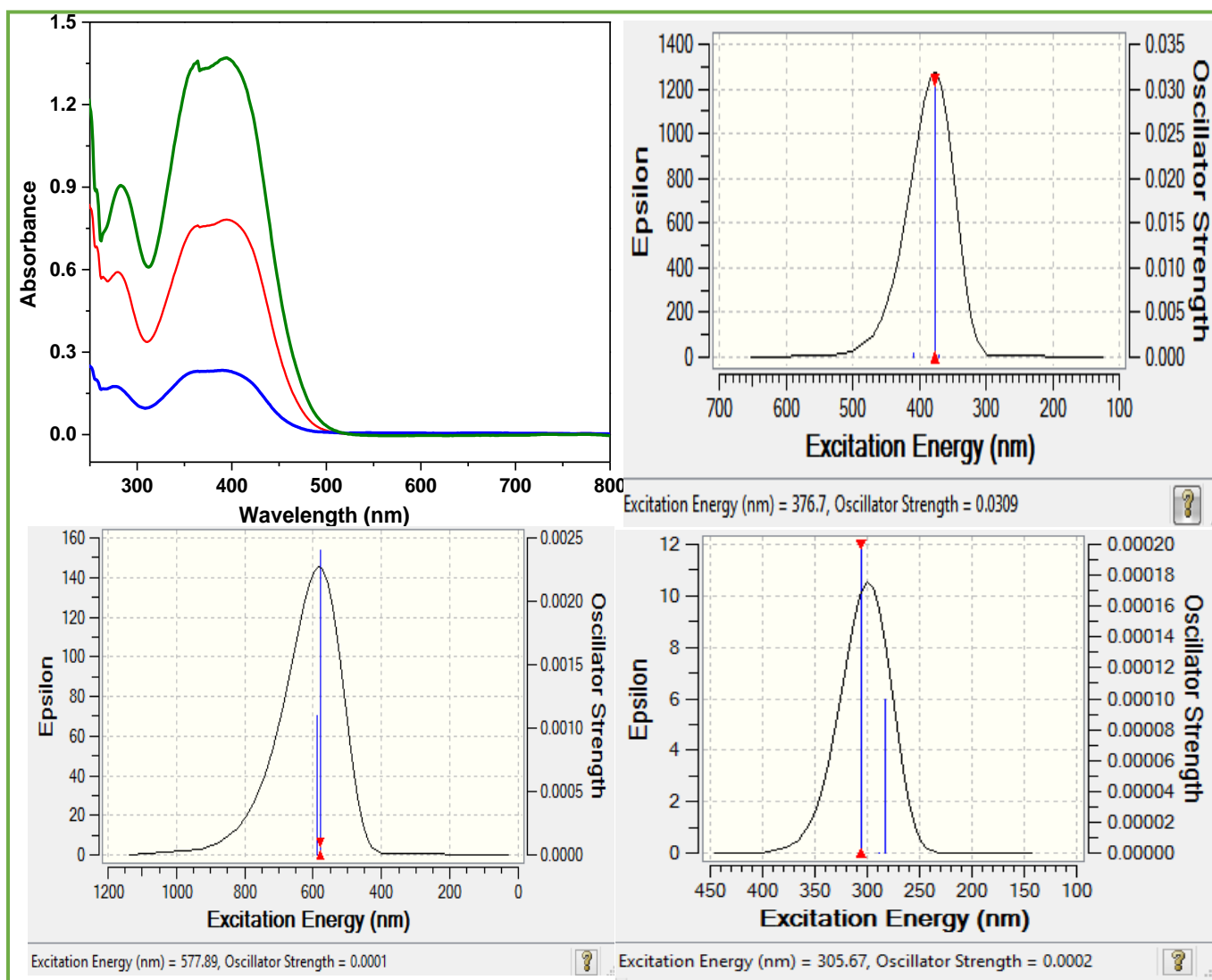


Fig. 3.6.4 Excitation energy of BNP (a) Experimental (b) TD-DFT (c) ZINDO (d) CIS

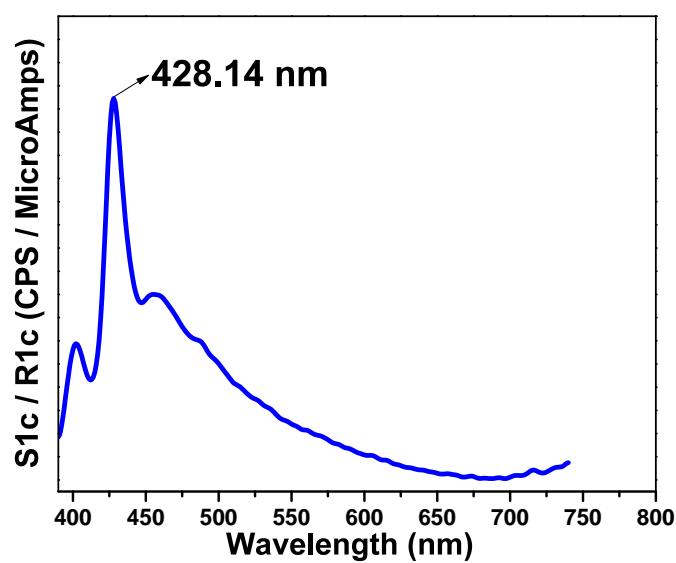


Fig.3.6. 5 Fluorescence spectra of BNP

The highest occupied molecular orbital and lowest unoccupied molecular orbital (HOMO-LUMO) of BNP are shown in Fig. 3.6.6. The frontier orbital gap enables in describing the chemical reactivity and kinetic strength of the molecule. The red and green colours represent the positive and negative standards for the wave function. The HOMO is the orbital that primarily perform as an electron donor and the LUMO is the orbital that mainly acts as an electron acceptor [26-27]. The energy gap between HOMO (-7.215 eV) to LUMO (-4.122 eV) of the molecule is about 3.093 eV. The chemical hardness of the molecule is calculated using Koopman's theorem [28] and is given by expression

$$\eta = \frac{(IP - EA)}{2} = 1.5465 \text{ eV}$$

where ionization potential (eV) $IP \approx -E(\text{HOMO})$; electron affinity (eV) $EA \approx -E(\text{LUMO})$. Since the chemical hardness, large HOMO, LUMO gap specifies a hardness of the molecule and small HOMO-LUMO gap specifies a softness of the molecule. The stability of the molecule in the direction of hardness, which assets that the molecule with smallest HOMO-LUMO gap specifies it is more reactive.

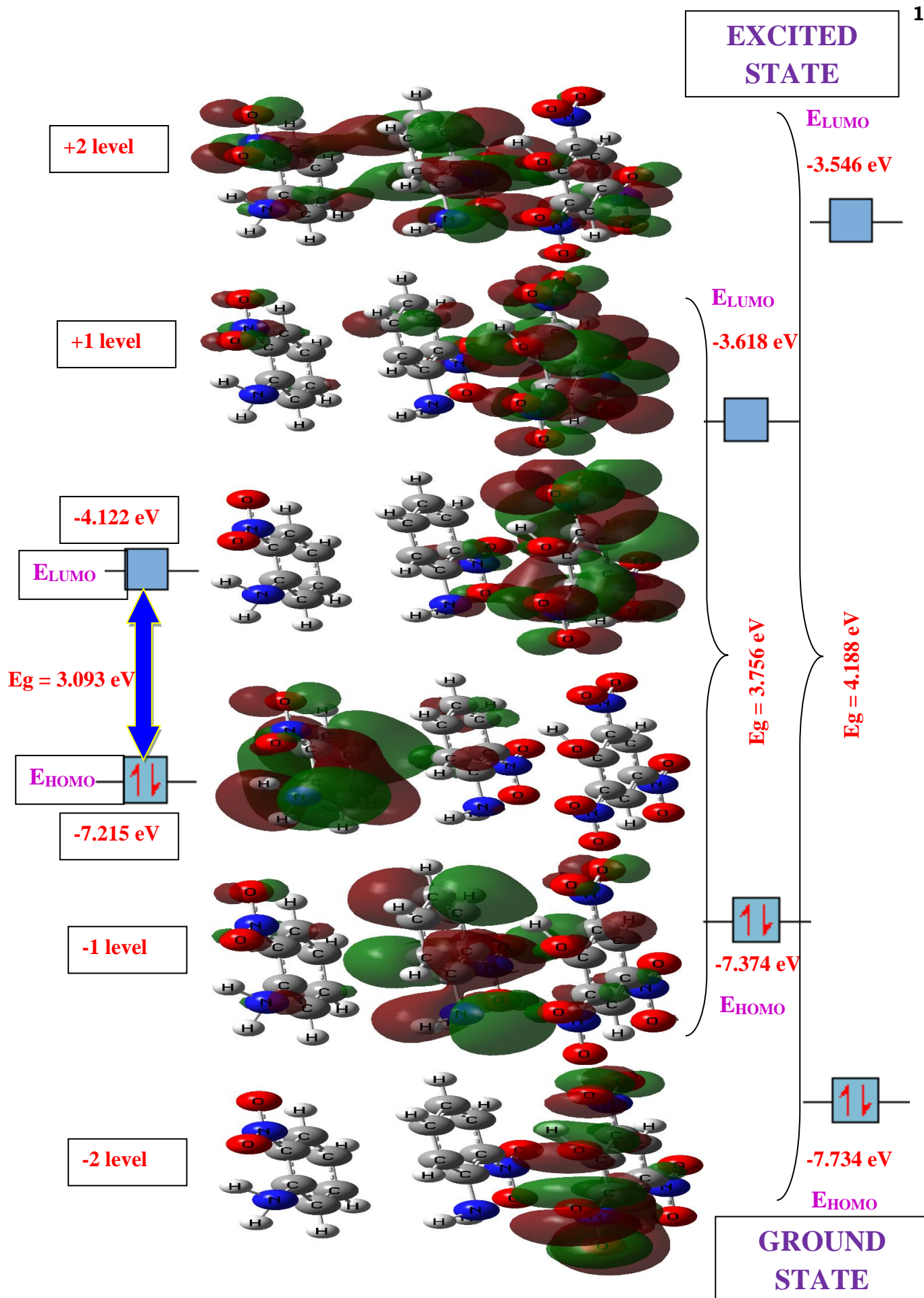


Fig. 3.6.6 HOMO-LUMO energy gap of BNP

3.3 UV-DRS

The indirect band gap energy (Fig. 3.6.7) of the crystalline material is calculated as 2.39 eV reflections from the Tauc plot by the application of Kubelka–Munk algorithm [29] (theory provides correlation between reflectance and concentration).

$$F(R) = (1 - R)^2 / 2R = \alpha/s = Ac/s$$

Where $F(R)$ is the Kubelka–Munk function, R is the reflectance of the solid and s is scattering coefficient, A is the absorbance and c is concentration of the absorbing species.

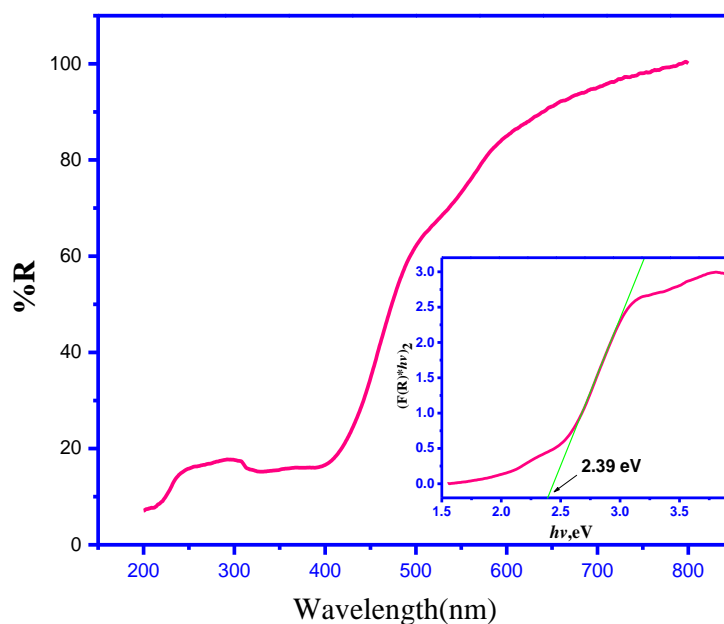


Fig. 3.6.7 UV-DRS spectrum of BNP (Tauc plot is given in inset)

3.5. Single crystal XRD

BNP crystallizes in the monoclinic system with non-centrosymmetric space group Cc and the cell parameters are “ $a = 9.304 \text{ \AA}(3)$, $b = 14.136 \text{ \AA}(4)$, $c = 13.11 \text{ \AA}(4)$ ” and “ $\beta = 107^\circ(4)$, $V = 1649 \text{ \AA}^3(9)$ ”. Cell parameters were matches with earlier structure [30], but structure morphology differs. The crystal cohesion is achieved by $N-H\cdots O$, $O-H\cdots O$, $C-H\cdots N$, $H\cdots H$, $O\cdots O$ and $\pi\cdots\pi$ staking interactions. Weak intermolecular interactions play major role in supramolecular materials. Weak supramolecular $\pi\cdots\pi$ staking interactions are displayed in Fig 3.6.9, with interaction distances of 3.001, 3.073 \AA . Crystal packing projections formed along the b-axis look like zigzag fashion. $N-H\cdots O$ (Fig 3.6.10) interactions were assembled with the bond distance about 1.976 \AA , 2.071 \AA , 2.352 \AA , 2.427 \AA and 2.609 \AA . Weak intermolecular contacts are assembled by $H\cdots H$, $O\cdots O$ (Fig 3.6.11) and these interactions were organized with the distance about “2.139 \AA , 2.378 \AA ” and “2.882 \AA , 2.844 \AA ” respectively.

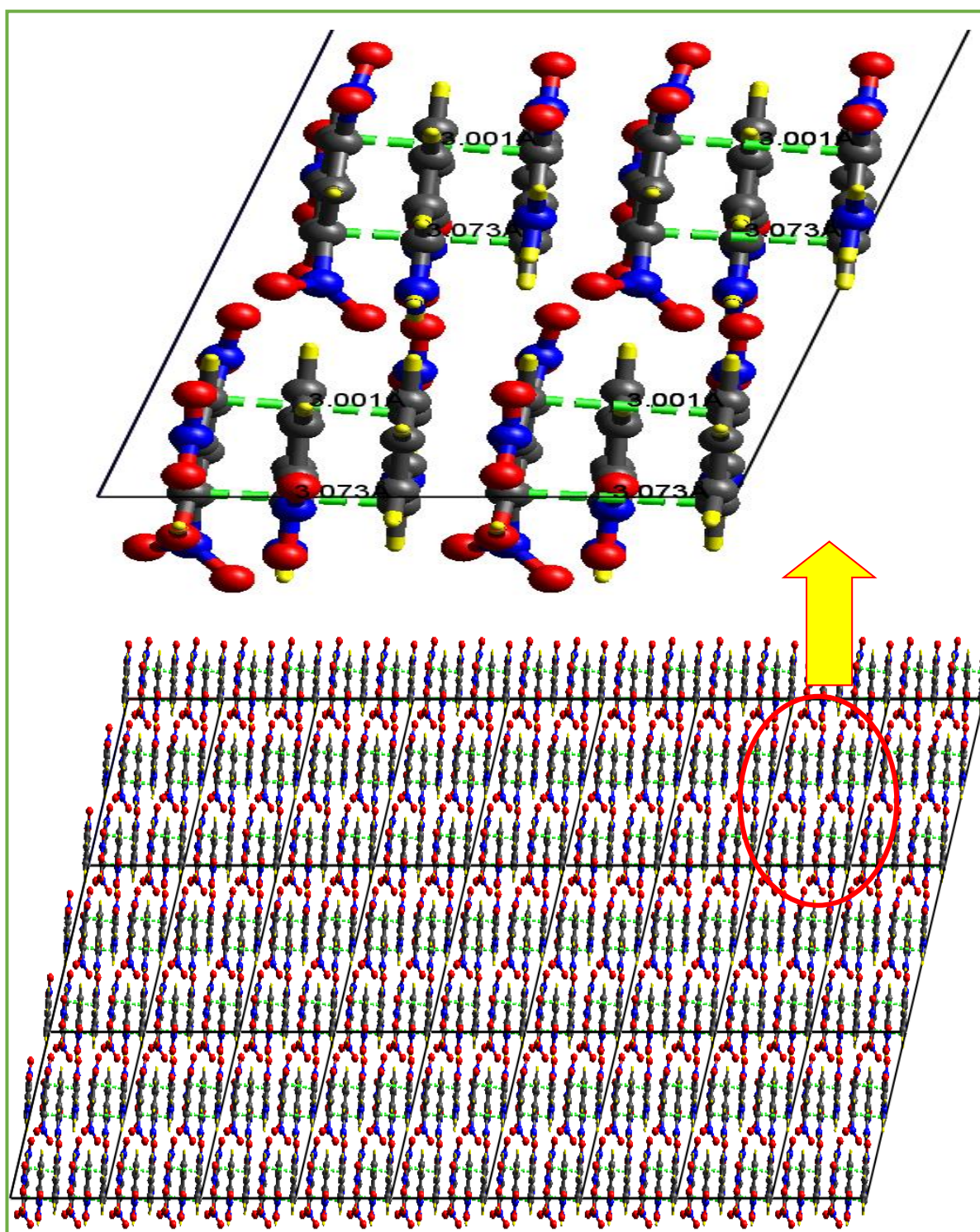


Fig.3.6. 9 Packing projection along a-axis showing $\pi\cdots\pi$ interactions

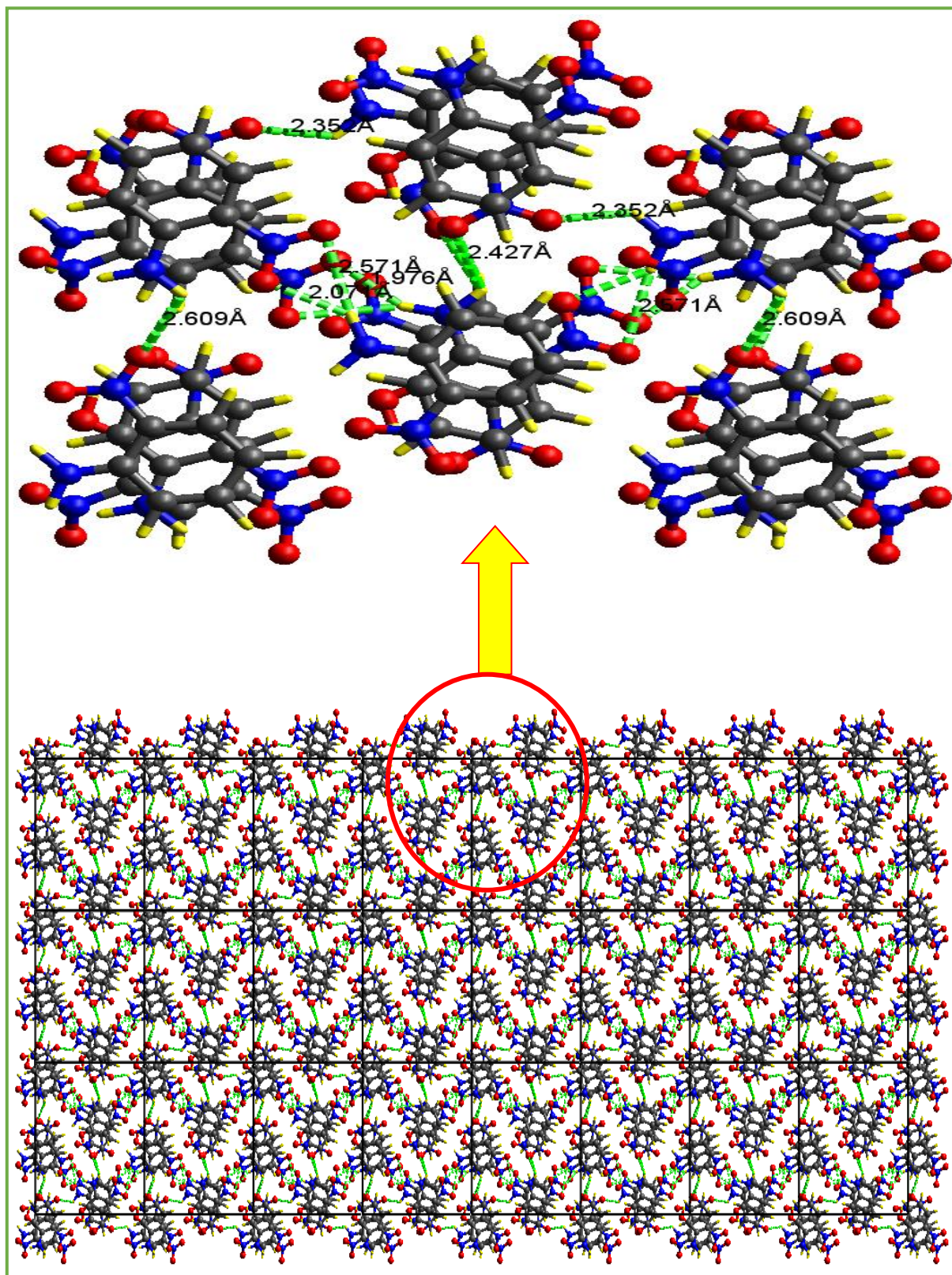


Fig.3.6.10 Packing projection along b-axis showing N-H...O interactions

3.6. First-order molecular hyperpolarizability

The first-order hyperpolarizability is a third-rank tensor that can be described by a 3 X 3 X 3 matrix. The 27 components of the 3D matrix can be reduced to 10 components due to the Kleinman symmetry [31]. It can be given in the lower tetrahedral format.

$$E = E^0 - \mu_\alpha F_\alpha - 1/2 \alpha_{\alpha\beta} F_\alpha F_\beta - 1/6 \beta_{\alpha\beta\gamma} F_\alpha F_\beta F_\gamma + \dots$$

where E^0 – is the energy of the unperturbed molecule, F_α – the field at the origin of μ_α , $\alpha_{\alpha\beta}$ and $\beta_{\alpha\beta\gamma}$ are the components of dipolemoment, polarizability and first-order molecular hyperpolarizability respectively.

$$\mu_0 = (\mu_x^2 + \mu_y^2 + \mu_z^2)^{1/2} \text{ and}$$

$$\beta_0 = (\beta_x^2 + \beta_y^2 + \beta_z^2)^{1/2}.$$

$$\beta_x = (\beta_{xxx} + \beta_{xyy} + \beta_{xzz}),$$

$$\beta_y = (\beta_{yyy} + \beta_{xxy} + \beta_{yzz}) \text{ and}$$

$$\beta_z = (\beta_{zzz} + \beta_{xxz} + \beta_{yyz}).$$

The computed first-order molecular hyperpolarizability (β) and dipolemoment (μ) of the sample are 16.016×10^{-30} esu (>56.64 times of urea) and 5.92 D respectively (Table 3.6.2). The large β is due to the performance of nonzero μ values. High beta rate is a required property of an NLO material.

Experimentally, nonlinear optical property is measured by using Kurtz and Perry technique. The input beam energy is 2.82 mJ/pulse. KDP sample was used as the reference material ($I_{2\omega} \sim 55$ mV) and the powder SHG efficiency of BNP was found to be ~ 1.2 times that of KDP ($I_{2\omega} \sim 66$ mV).

Table 3.6.2. The calculated β components, β_{tot} value (esu), dipole moment (μ , D) and HOMO-LUMO (eV) characteristic of BNP.

β_{xxx}	-1581.083
β_{xxy}	-283.579
β_{xyy}	-179.003
β_{yyy}	409.604
β_{xxz}	-151.929
β_{xyz}	-28.822
β_{yyz}	-243.412
β_{xzz}	-37.210
β_{yxx}	-317.652
β_{zzz}	-16.737
$\beta_{tot} (\times 10^{-30})$	16.016
μ	5.920
E_{HOMO}	-7.215 eV
E_{LUMO}	-4.122 eV
$E_{HOMO} - E_{LUMO}$	3.093 eV

3.7 Hirshfeld surface analysis

The Hirshfeld surface [32, 33] is an essential approach for investigating intermolecular interactions. All the molecular interactions occurring in the crystal packing are quantified and pie chart of molecular interactions was displayed in Fig 3.6.12. The Hirshfeld surface surrounding a molecule is indicated by points where the connection to the electron density from the molecule is identical to the influence from all the other molecules. The normalized contact distance (d_{norm}) based on both d_e and d_i , and the radii of the atom which facilitate identification of the areas of

specific intermolecular interactions. On behalf of every value on the iso-surface two distances are well-defined, such as d_e - the distance from the point to the adjacent nucleus external to the surface and d_i - the distance to the adjacent nucleus internal to the surface.

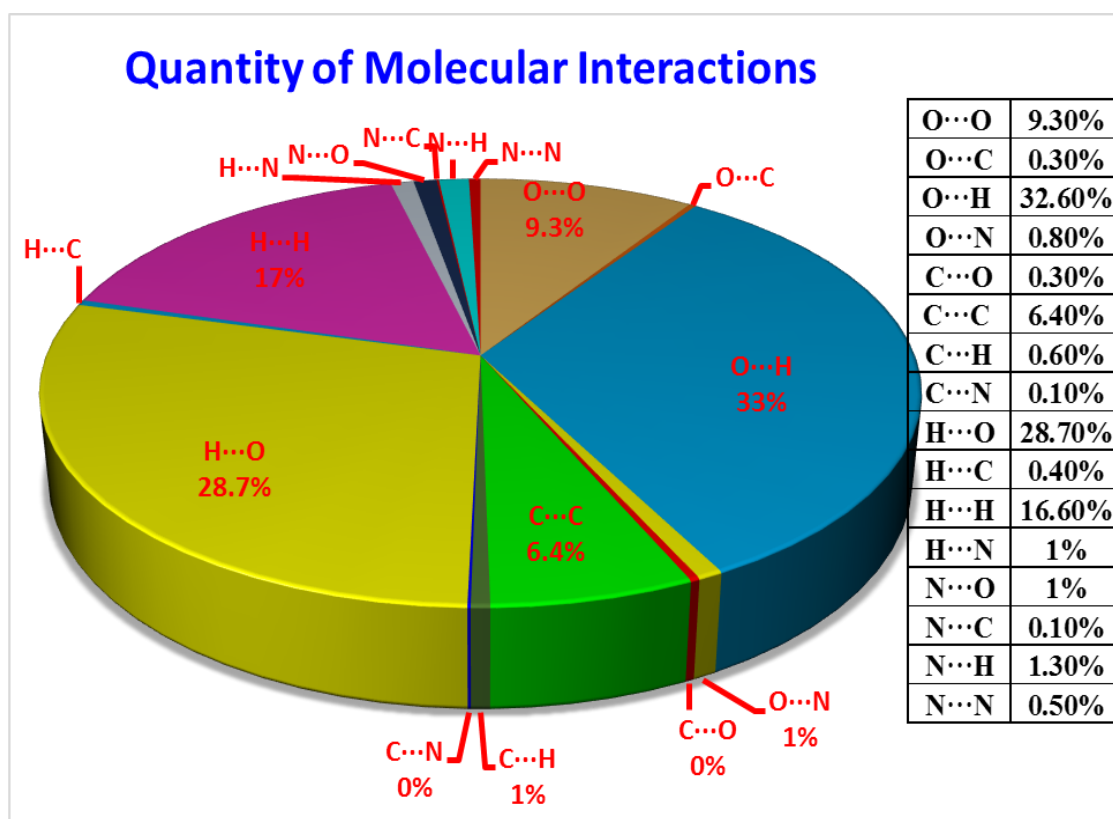


Fig.3.6.12 Pie chart of molecular interactions

The value of the $dnorm$ is negative or positive when intermolecular contacts are shorter or longer. Because of the symmetry between d_e and d_i in the appearance for $dnorm$, where two Hirshfeld surfaces touch, both will display a red spot identical in colour intensity as well as size and shape. The combination of d_e and d_i in the form of a 2D fingerprint plots provides an immediate of intermolecular interactions in the crystal. Graphical plots of the molecular Hirshfeld surfaces were mapped with $dnorm$ using a red-

white–blue colour system. The red indicates less distance interaction; white is comparatively long distance around the surface and blue represents longer interactions. Moreover, further coloured properties (curvedness Fig 3.6.13(d)) based on the local curvature of the surface can be specified.

Curvedness is an evaluate of “shape”, while areas of sharp curvature possess a high curvedness and tend to divide the surface into patches associated with contacts between neighbouring molecules. Bright red colour in the Fig 3.6.13(a) are the indication of strong interactions such as O···O (9.3%), H···O (28.7%), π ··· π (6.4%) and O···H (32.6%). In the same way *di surface* (Fig 3.6.13c), comparatively strong interactions O···H (32.6%). Weak interactions are indicated with yellow colour in the Fig 3.6.13b, *de surface* clearly indicates the H···O (28.7%) interactions. Moreover fingerprint plots [34] are strong proof for the quantity of interactions with each and every molecule to molecule in the crystal packing. Many interactions are symbolized as spikes in the fingerprint plots Fig 3.6.14. The O···H, H···O and H···H interactions are more. Less interactions are “H···C & C···H (1%)”, “N···O & O···N (1.5%)” and “O···C & C···O (0.6%)”.

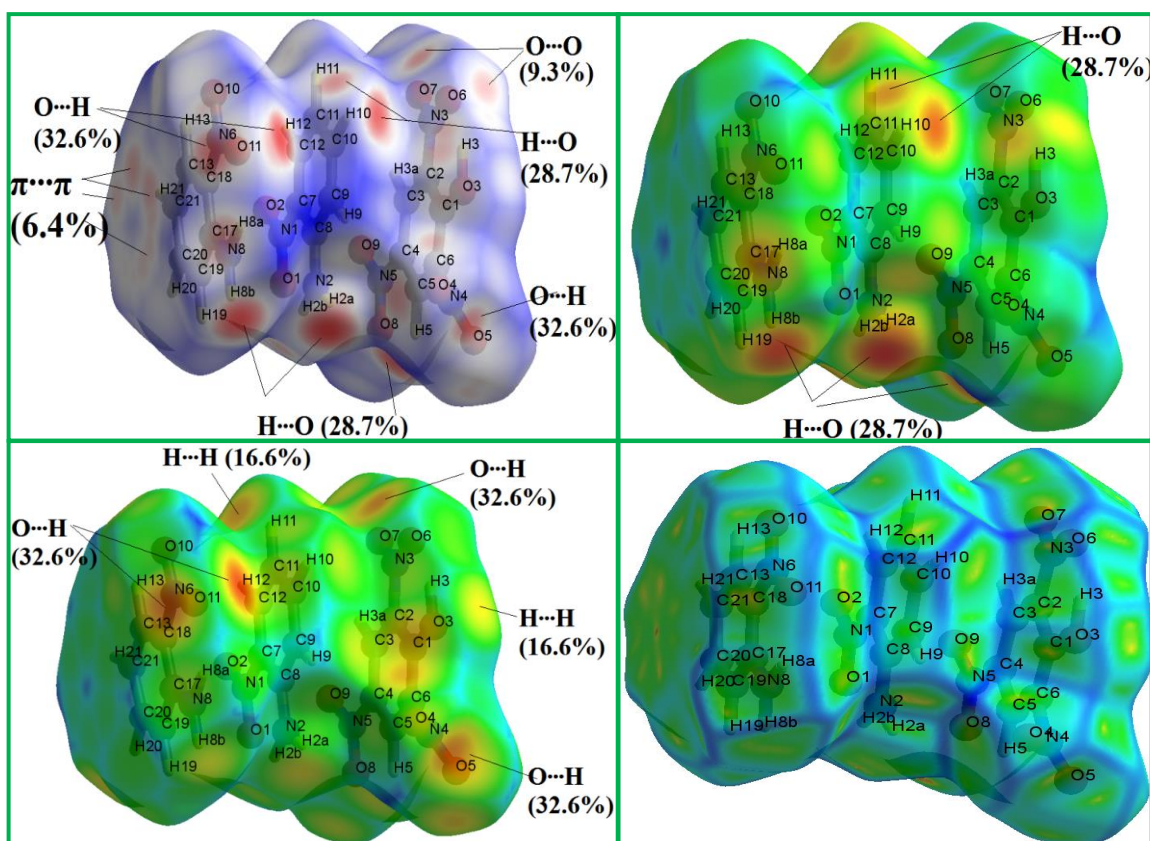


Fig. 3.6.13 Hirshfeld surfaces of BNP (a) *dnorm* (b) *di* (c) *de* (d) *curvedness*

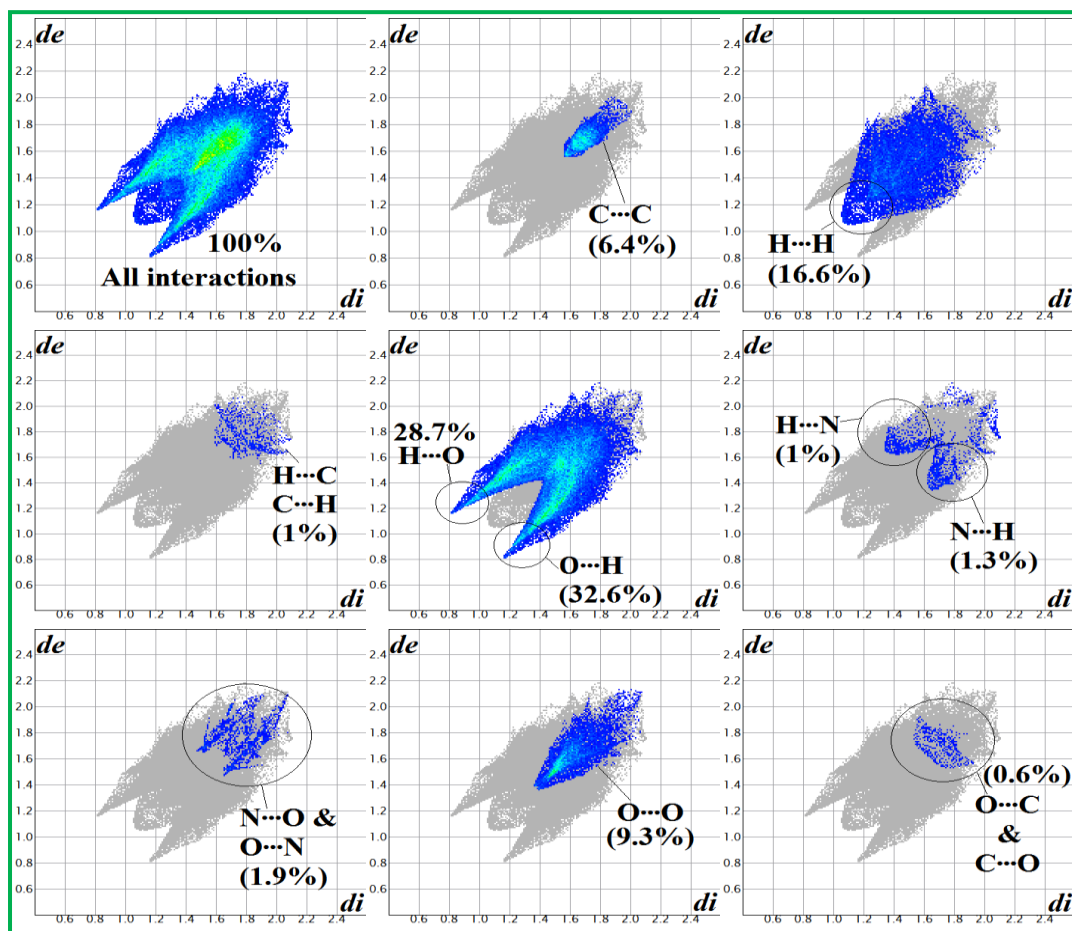


Fig. 3.6.14 Fingerprint plot analysis of BNP

4. Conclusions

Reddish yellow coloured crystals of bis(2-nitroaniline) picrate were successfully grown by slow evaporation solution growth technique at constant temperature. The product formation was confirmed by FT-IR and single crystal XRD analyses. Comparison of bond length and angles of theoretical and experimental values shows slight variations. It crystallizes in a space group *Cc* with four molecules in the unitcell. A sharp peak in ESR spectrum represents the paramagnetic behaviour of the material. Hydrogen bonding interactions were quantified using fingerprint and Hirshfeld surface analysis. Supramolecular architecture is confirmed by Inter- and intramolecular hydrogen bonding interactions were construed by N-H \cdots O, O-H \cdots O, C-H \cdots N, H \cdots H, O \cdots O and $\pi\cdots\pi$ staking interactions.

Supplementary information

CCDC1009556 contains the supplementary crystallographic data for this paper. These data can be obtained free of charge from The Cambridge Crystallographic Data Centre *via* www.ccdc.cam.ac.uk/data_request/cif.

References

- [1] Skarp.K, Handschy.M. A,(1988) *Molecular Crystals and Liquid Crystals Incorporating Nonlinear Optics*, 165Issue 1
- [2] Moulson.A. J., Herbert.J. M., *Electroceramics: Materials, Properties, Applications*, John Wiley & Sons Ltd. The Atrium, Southern Gate, Chichester, England. 2003
- [3] Bymathias O. Senge, Marijana Fazekas, Eleni G. A. Notaras,Werner J. Blau, Monika Zawadzka, Oliver B. Locos andEimhin M. Ni Mhuircheartaigh, (2007) *Adv. Mater.* 19, 2737–2774

- [4] Dhanabal.T., Amirthaganesan.G., Dhandapani.M.,(2014)*Optik* 125 4341–4346
- [5] Lekshmi P. Nair, Bijini.B.R., Prasanna.S., Eapen.S.M., Nair.C.M.K., Deepa.M., RajendraBabu.K., (2015) *Spectrochimica Acta Part A*, 137, 778–784
- [6] Pramod B. Pansuriya, Glenn E.M. Maguire, Holger B. Friedrich, (2015) *Spectrochimica Acta Part A*,
<http://dx.doi.org/10.1016/j.saa.2015.01.090>
- [7] Uma.J., Rajendran.V.,(2014)*Optik* 125,816–819
- [8] Peramaiyan.G., Pandi.P., Mohan Kumar.R., (2015) *J Therm Anal Calorim*, 119, 291–299
- [9] Krishna Kumar.V., Nagalakshmi.R., (2007) *Spectrochimica Acta Part A* 66 924–934
- [10] Muthu.K., Subbiah Meenakshisundaram, (2012) *Journal of Crystal Growth*, 352, 163–166
- [11] Aditya Prasad.A., Muthu.K., Meenatchi.V., Rajasekar.M., Meenakshisundaram.S. P., Mojumdar.S.C., *J Therm Anal Calorim.*, DOI 10.1007/s10973-014-4255-8
- [12] Aditya Prasad.A., Muthu.K., Rajasekar.M., Meenatchi.V., Meenakshisundaram.S.P., (2015) *Spectrochimica Acta Part A*, 135, 46–54
- [13] Aditya Prasad.A., Muthu.K., Rajasekar.M., Meenatchi.V., Meenakshisundaram.S.P., (2015) *Spectrochimica Acta Part A*, 135, 805–813
- [14] Gaussian 09, Revision C.01, Frisch, M. J.; Trucks, G. W.; Schlegel, H. B.; Scuseria, G. E.; Robb, M. A.; Cheeseman, J. R.; Scalmani, G.;

- Barone, V.; Mennucci, B.; Petersson, G. A.; Nakatsuji, H.; Caricato, M.; Li, X.; Hratchian, H. P.; Izmaylov, A. F.; Bloino, J.; Zheng, G.; Sonnenberg, J. L.; Hada, M.; Ehara, M.; Toyota, K.; Fukuda, R.; Hasegawa, J.; Ishida, M.; Nakajima, T.; Honda, Y.; Kitao, O.; Nakai, H.; Vreven, T.; Montgomery, J. A., Jr.; Peralta, J. E.; Ogliaro, F.; Bearpark, M.; Heyd, J. J.; Brothers, E.; Kudin, K. N.; Staroverov, V. N.; Kobayashi, R.; Normand, J.; Raghavachari, K.; Rendell, A.; Burant, J. C.; Iyengar, S. S.; Tomasi, J.; Cossi, M.; Rega, N.; Millam, M. J.; Klene, M.; Knox, J. E.; Cross, J. B.; Bakken, V.; Adamo, C.; Jaramillo, J.; Gomperts, R.; Stratmann, R. E.; Yazyev, O.; Austin, A. J.; Cammi, R.; Pomelli, C.; Ochterski, J. W.; Martin, R. L.; Morokuma, K.; Zakrzewski, V. G.; Voth, G. A.; Salvador, P.; Dannenberg, J. J.; Dapprich, S.; Daniels, A. D.; Farkas, Ö.; Foresman, J. B.; Ortiz, J. V.; Cioslowski, J.; Fox, D. J. Gaussian, Inc., Wallingford CT, 2009.
- [15] Roy Dennington, Todd Keith and John Millam, GaussView, Version 5, Semichem Inc., Shawnee Mission KS, 2009
- [16] Jamroz.M.H., (2013) Vibrational energy distribution analysis, *Spectrochim. Acta A*, 114,220
- [17] Wolff.S. K., Grimwood.D. J., McKinnon.J. J., Jayatilaka.D., and Spackman.M. A., CrystalExplorer 3.1, University of Western Australia, Perth, Australia, 2007
- [18] Dolomanov, O.V., Bourhis, L.J., Gildea, R.J, Howard, J.A.K. & Puschmann, H., *J. Appl. Cryst.* 42(2009) 339-341
- [19] Bourhis, L.J., Dolomanov, O.V., Gildea, R.J., Howard, J.A.K., Puschmann, H.,*Acta Cryst. A*71 (2015) 59-75
- [20] Kurtz.S.K., Perry.T.T., (1968) *J. Appl. Phys.* 39, 3798

- [21] Bharathikannan.R., Chandramohan.A., Kandhaswamy.M. A., Chandrasekaran.J., Renganathan.R., and Kandavelu.V., (2008)*Cryst. Res. Technol.* 43, 683 – 688
- [22] Mulliken.R.S.,(1952) *J. Am. Chem. Soc.* 74, 811
- [23] Mulliken.R.S., (1955) *J. Chem. Phys.* 23, 1833
- [24] Maiorov.V.N., and Crippen.G.M., (1994) *J. Mol. Biol.* 235, 625-635
- [25] Rob J. Hyndman, Anne B. Koehler, (2006) *Int. J. of Forecasting* 22, 679–688
- [26] Thanthiriwatte.K.S., Nalin de Silva.K.M., (2002) *J. Mol. Struct.* 617,169.
- [27] Liyange.P.S., de Silva.R.M., Nalin de Silva.K.M.,(2003)*J. Mol. Struct.* 639,195
- [28] Koopmans, Tjalling, (1934)*Physica*, 1, 104–113
- [29] Kubelka.P.,(1948) *J. Opt. Soc. Am.* 38, 448
- [30] Saminathan.K., Sivakumar.K., (2007) *Acta Cryst. E*63,o354–o356
- [31] Kleinman.D.A., (1962) *Phys. Rev.*,126, 1977-1979
- [32] Hirshfeld.F. L., (1977) *Theor. Chim. Acta*, 44, 129–138
- [33] Koenderink.J. J., and van Doorn.A., (1992)*Image Vision Comput.*, 10,557
- [34] Spackman.M.A., McKinnon.J.J.,(2002)*CrystEngComm* 4, 378

LIST OF PUBLICATIONS UNDER THE PROJECT WORK

1. A. Aditya Prasad, K. Muthu, M. Rajasekar, V. Meenatchi, **S.P. Meenakshisundaram***, *SpectrochimicaActa Part A: Molecular and Biomolecular Spectroscopy*, **135** (2015) 46–54
2. A. Aditya Prasad, K. Muthu, V. Meenatchi, M. Rajasekar, **S.P. Meenakshisundaram**, S. C. Mojumdar, *J Therm Anal Calorim*, **119** (2015) 885–890
3. A. Aditya Prasad, K. Muthu, M. Rajasekar, V. Meenatchi, **S.P. Meenakshisundaram***, *SpectrochimicaActa Part A: Molecular and Biomolecular Spectroscopy*, **135** (2015) 805–813
4. A. Aditya Prasad, K. Muthu, V. Meenatchi, M. Rajasekar, R. Agilandeshwari, K. Meena, J. VijilaManonmoni, **S.P. Meenakshisundaram***, *SpectrochimicaActa Part A: Molecular and Biomolecular Spectroscopy*, **140** (2015) 311–327
5. A. Aditya Prasad, **SP. Meenakshisundaram**, *J. Appl. Cryst*, **48** (2015) 844–852
6. A. Aditya Prasad, **SP. Meenakshisundaram**, *Cryst. Res. Technol*, **50**, No. 5 (2015) 395-404
7. R. Agilandeswari, A. Aditya Prasad, S. Sivaraman, S. Kalainathan, **SP. Meenakshisundaram***, *Molecular crystals and liquid crystals*, 625:1, (2016) 238-252.